Molecular Interaction and Adhesion Mechanisms of Mussel-inspired Adhesive Coatings

By

Li Xiang

A thesis submitted in partial fulfillment of the requirements for the degree of
Doctor of Philosophy
in
Chemical Engineering

Department of Chemical & Materials Engineering
University of Alberta

©Li Xiang, 2020

Abstract

In marine mussel adhesion science, mussel foot proteins (mfps) have been identified to play an essential role in forming the bioadhesive coating. A catecholic amino acid named 3,4-dihydroxyphenyl-L-alanine (DOPA) has been found to primarily contribute to such robust underwater adhesion performance by employing various catechol-modulated interactions including hydrogen bonding, coordination bonding, π-π stacking, cation-π interaction and covalent cross-linking. Based on these interactions, numerous underwater adhesives and coatings have been developed and applied for specific use purposes. Nevertheless, for synthetic adhesives, completely achieving adhesive coatings as robust as bioadhesvies is still a big challenge. Therefore, further studies on DOPA interfacial behavior is of great importance as it can provide both fundamental and practical insights into successfully translating Dopa chemistry to adhesion technology and engineering advanced materials. In this thesis, a surface forces apparatus (SFA) was applied to further explore the interaction mechanisms underlying mussel-inspired catecholic adhesion system, with specific focus on the roles of functional groups in mfps (e.g., catechol and amine), substrate surface chemistry (e.g., organic and inorganic surfaces) and water chemistry (e.g. salinity and salt type), and test the feasibility of potential coating strategies which may be utilized in surface functionalization under practical aqueous conditions.

In the first work, a facile and versatile approach to prepare robust adhesive coating in aqueous solutions with high salinity and mild alkalinity was demonstrated through the incorporation of primary amines into polydopamine (PDA) during the polymerization of dopamine (i.e., catecholamine). SFA were applied to precisely quantify the interaction forces between PDA-amine adhesive coatings and investigate the impact of

amine species amine content and water chemistry on the adhesion behaviour. The measured strong adhesion force was mainly achieved through the synergetic effect of amine and PDA, including the displacement of hydrated salt ions adsorbed on the surface by cationic amine, strong adhesion to substrate via catechol groups on PDA moieties and enhanced cohesion achieved by their cation-π interactions.

In the second work, a study on the correlation between interaction behavior and deposition capability of DOPA-amine based adhesive coatings was conducted by virtue of SFA and AFM. Using tannic acid (TA) and diethylenetriamine (DETA) as the model catecholic moiety and amine, the mass ratio between catecholic moiety and amine was found to have a significant influence on the coating thickness, surface roughness and surface morphology during the deposition of adhesive coating through regulating the electric double layer (EDL) repulsion between as-formed TA-DETA aggregates. Such TA-DETA adhesive shown a strong adhesion to substrate surfaces bearing varies surface chemistry and wettability via multiple interactionsits because of its specific molecular structure and chemical properties, which was demonstrated to primarily contribute to the initiation of the formation of adhesive coating.

In the third work, SFA and AFM were applied to directly quantify the correlation between the nanomechanics and deposition behavior of mussel-inspired polypyrocatechol (pPC) adhesive coatings in various monovalent saline aqueous media. For the first time, a different yet experimentally unexplored type of cation-π interaction with ternary π-cation-π configuration was identified. The ternary π-cation-π interaction was found to be able to induce the bridging effect of salt cation with two π-conjugated catechol groups, through which the monovalent cations actively participated in and greatly enhanced the wet adhesion and deposition of catechol-based adhesive coatings. By varying salt cation concentration, this ternary interaction could transform to a binary

cation-π interaction at high cation concentration, leading to the abolishment of bridging and the undermined adhesion and deposition. Furthermore, such π-cation-π interaction behavior was demonstrated to be general for various cation species with the trend of binding strength following $NMe_4^+ > K^+ > Na^+ > Li^+$.

In the fourth work, a non-covalent interaction called anion-π interaction was experimentally identified for the first time, which was found to play a critical role in biomolecular underwater adhesion. The nanomechanics of anion-π interaction was directly quantified in a model system containing anionic phosphate ester and π-conjugated catecholic moieties which abound in marine bioadhesives, by using a surface forces apparatus with complementary computational simulations. Anion-π interaction, cooperated by cation-π interaction due to co-existence of cation, was unravelled to synergistically contribute to robust wet-adhesion. The anion-π interaction strength follows the trend of phosphate ester > HPO_4^{2-} > SO_4^{2-}> NO_3^-, affected by charge density, polarity and hydration effect.

Preface

Chapter 3 of this thesis has been published as Chao Zhang, Li Xiang, Jiawen Zhang, Lu Gong, Linbo Han, Zhikang Xu and Hongbo Zeng, "Tough and Alkaline-Resistant Mussel-Inspired Wet Adhesion with Surface Salt Displacement via Polydopamine-Amine Synergy," *Langmuir* 35.15 (2019): 5257-5263. Chao Zhang and I contributed equally to this work. Chao and I designed the research under the supervision of Dr. Hongbo Zeng. Chao Zhang was responsible for the material design, result discussion and manuscript composition. I was responsible for the SFA and AFM experiment and data analysis and discussion as well as the manuscript composition. Jiawen Zhang, Lu Gong and Linbo Han assist to interpret the data, discussed the results and commented on the manuscript. Dr. Zhikang Xu and Dr. Hongbo Zeng were the corresponding author and was involved in concept formation and manuscript composition.

Chapter 4 of this thesis has been published as by Li Xiang, Jiawen Zhang, Lu Gong, Linbo Han, Chao Zhang, Bin Yan, Jifang Li and Hongbo Zeng, "Probing the interaction forces of phenol/amine deposition in wet adhesion: impact of phenol/amine mass ratio and surface properties," *Langmuir* 35.48 (2019): 15639-15650. Jiawen Zhang and I conceived the research under the supervision of Dr. Hongbo Zeng. I performed and analysed experimental results as well as manuscript composition. Jiawen Zhang was responsible for data analysis, result discussion and manuscript composition. Lu Gong, Linbo Han and Chao Zhang contributed to interpret the data, discussed the results and commented on the manuscript. Dr. Bin Yan, Dr. Jifang Li and Dr. Hongbo Zeng were the supervisor who was involved in concept formation and manuscript composition.

Chapter 5 of this thesis will be submitted for publication as Li Xiang, Jiawen Zhang, Wenda Wang, Lu Gong, Ling Zhang, Bin Yan and Hongbo Zeng, "Nanomechanics of π-cation-π Interaction for Bio-inspired Wet Adhesion." Jiawen Zhang and I conceived the research under the supervision of Dr. Hongbo Zeng. I performed experiments and analysed experimental results as well as manuscript composition. Jiawen Zhang was responsible for data analysis, result discussion and manuscript composition. Lu Gong, Linbo Han and Chao Zhang contributed to interpret the data, discussed the results and commented on the manuscript. Dr. Hongbo Zeng was the corresponding author and was involved in concept formation and manuscript composition.

Chapter 6 of this thesis has been published as by Jiawen Zhang, Li Xiang, Bin Yan and Hongbo Zeng, "Nanomechanics of Anion-π Interaction in Aqueous Media," *J. Am. Chem. Soc.* 142. 4 (2020): 1710–1714. Jiawen Zhang and I contributed equally to this work. Jiawen Zhang and I conceived the research and design the experiments under the supervision of Dr. Hongbo Zeng. Jiawen Zhang performed material synthesis, result discussion and manuscript composition. I performed experiments and analysed experimental results as well as manuscript composition. Bin Yan contributed to interpret the data, discussed the results and commented on the manuscript. Dr. Hongbo Zeng was the corresponding author and was involved in concept formation and manuscript composition.

Acknowledgements

I would like to express my sincere gratitude to my supervisor Prof. Hongbo Zeng for giving me the opportunity to study in University of Alberta and introducing me to the fantastic world of intermolecular and surface interactions and functional materials. Thanks for providing the excellent laboratory facilities and research atmosphere during the whole course of my PhD study. With conscientious attitude and great dedication to scientific research, he is always a role model for me to become a scientific researcher in the future. I really appreciate his insightful guidance, valuable suggestions and continued encouragements, both in academic research and in career planning.

I would like to thank all groups members for the concern and help all the time. I want to thank Dr. Bin Yan for teaching me a lot in polymer synthesis at the very beginning of my PhD study. Many thanks to Dr Jiawen Zhang and Dr Lu Gong for their constant support and generous help when my researches got stuck. Special thanks to Mr Wenda Wang for valuable discussion regarding the fusion of fundamental interaction mechanism to functional material design.

My deep thanks go to my family, especially my parents, my parents in law and my wife Jiawen Zhang. Your love and support always encourage me to keep moving forward and chasing my dream.

My sincere gratitude goes to China Scholarship Council the Natural Sciences and Engineering Research Council of Canada, the Canada Foundation for Innovation, the Alberta Advanced Education & Technology Small Equipment Grants Program and the Canada Research Chairs Program for the financial support.

Table of Contents

Abstract ii

Preface v

Table of Contents viii

List of Figure xi

List of Abbreviations xvii

Chapter 1. Introduction 1

1.1 Mussel adhesion behavior 1

1.1.1 Mussel foot proteins 2

1.1.2 Interactions involved in mussel foot proteins 3

1.2 Mussel-inspired adhesive coatings 6

1.3 Objectives 9

1.4 Structure of the thesis 10

Reference 12

Chapter 2. Experimental Techniques 18

2.1 Surface forces apparatus (SFA) 18

2.1.1 SFA experiment setup 19

2.1.2 Force measurement using SFA 20

2.1.3 Multiple beam interferometry (MBI) 21

2.2 Other techniques 24

References 27

Chapter 3. Tough and Alkaline-Resistant Mussel-Inspired Wet Adhesion with Surface Salt Displacement via Polydopamine-Amine Synergy 29

3.1 Introduction 29

3.2 Materials and Experimental Methods 33

3.2.1 Materials 33
3.2.2 Fabrication and characterization of PDA and PDA/amines coatings 34
3.2.3 Surface force measurements using surface forces apparatus (SFA) 34
3.3 Results and Discussion 35
3.4 Conclusions 46
3.5 Supporting information 47
References 53
Chapter 4. Probing the Interaction Forces of Phenol/amine Deposition in Wet Adhesion: Impact of Phenol/amine Mass Ratio and Surface Properties 58
4.1 Introduction 58
4.2 Materials and Experimental Methods 60
4.3 Results and Discussion 64
4.4 Conclusions 81
4.5 Supporting information 82
References 84
Chapter 5. Nanomechanics of π-cation-π Interaction for Bio-inspired Wet Adhesion 88
5.1 Introduction 88
5.2 Materials and Experimental Methods 91
5.2.1 Materials. 91
5.2.2 Fabrication and characterization of poly(pyrocatechol) (pPC) films 92
5.2.3 Surface forces measurements using surface forces apparatus (SFA) 92

5.3 Results and Discussion 93
5.4 Conclusions 100
5.5 Supporting information 101
Reference 105
Chapter 6 Nanomechanics of Anion-π Interaction in Aqueous Media 107
6.1 Introduction 107
6.2 Materials and Experimental Methods 111
6.2.1 Materials and synthesis 111
6.2.2 Experimental method 113
6.3 Results and discussion 118
6.4 Conclusions 122
6.5 Supporting information 123
References 134
Chapter 7 Conclusions and Future Work 138
Bibliography 143

List of Figure

Figure 1.1 (a) The schematic of mussel structure on sectional view. (b) Schematic cross-section view of the mussel byssal plaque showing the approximate distribution of mussel foot protein distribution. (Reproduced from reference 15) 2

Figure 1.2 DOPA-mediated various non-covalent and covalent interactions in mussel foot proteins. 5

Figure 2.1 Section view of SFA 2000 through the center of the apparatus.[10] 19

Figure 2.2 Schematic of a typical SFA experimental setup.[15] 20

Figure 2.3 FECO of mica surface in air (a) under adhesive (separation distance $D_0 = 0$) and (b) separated by a distance D. 24

Figure 3.1 (a) Primary sequences of mussel foot protein (mfp-3f) and molecular structure of according amino acid residues. (b) Schematic illustration of mussel-inspired process based on the one-step reaction of dopamine and primary amine under Tris buffer. 33

Figure 3.2 (a) Schematic of surface force measurements between two PDA layers or PDA/PEI layers deposited on mica via SFA. (b) Force-distance curves of PDA layers and PDA/PEI (Mw = 800 g/mol) layers on mica surfaces after in situ polymerization in Tris buffer solution (pH=8.5, 50 mM) with 250 mM KCl. The concentration of dopamine and PEI is 2 mg/mL and 1 mg/mL, respectively. (c) Schematic illustration of salt displacement and deposition process of dopamine and dopamine/amine systems. Primary amine group shows a positive charge at pH 8.5.....37

Figure 3.3 UV-vis spectra associated with the polymerization process of dopamine in tris buffer solution (pH=8.5, 50 mM) with or without the existence presence of

250 mM KCl. 38

Figure 3.4 Adhesion force and adhesion energy of PDA/PEI (Mw = 800 g/mol) layers with different PEI concentrations deposited on mica after in situ polymerization in Tris buffer solution (pH=8.5, 50 mM) with 250 mM KCl. The mass ratios of dopamine (DA) and PEI (DA/PEI) are 2:0.5, 2:0.7, 2:1, 2:1.5 and 2:2. 40

Figure 3.5 (a, b) Force-distance curves of PDA/PEI (Mw = 800 g/mol) films coated on mica after in situ polymerization in Tris buffer solution (pH=8.5, 50 mM) with (a) 250 mM KCl and (b) 600 mM KCl. The concentrations of dopamine and PEI (Mw = 800 g/mol) are fixed at 2 mg/mL and 1 mg/mL, respectively. 41

Figure 3.6 AFM topographic images of PDA and PDA/different amines coatings on mica: (a) PDA/o-phenylenediamine, (b) PDA/tetraethylenepenamine, (c) PDA/polyethyenimine (Mw = 2000 g/mol) and (d) PDA/polyethyenimine (Mw = 25000 g/mol). The polymerization conditions are Tris buffer solution (pH=8.5, 50 mM) with 250 mM KCl for 4 h. The concentrations of dopamine and amine are 2 mg/mL and 1 mg/mL, respectively. 43

Figure 3.7 Adhesion force and adhesion energy of PDA/different amines layers: (A) PDA/o-phenylenediamine, (B) PDA/tetraethylenepenamine, (C) PDA/PEI (Mw = 800 g/mol), (D) PDA/PEI (Mw = 2000 g/mol) and (E) PDA/PEI (Mw = 25000 g/mol), deposited on mica after in situ polymerization in Tris buffer solution (pH=8.5, 50 mM) with 250 mM KCl. The concentrations of dopamine and amines were fixed at 2 mg/mL and 1 mg/mL, respectively. 44

Figure 3.8 (a) AFM height image of PDA/PEI coatings underwater. (b) AFM modulus mapping of PDA/PEI coatings. Each DMT modulus map was analyzed at least using three cross sections across the modulus map. Young's modulus is around 4.1 GPa. 45

Figure 3.9 Force-distance curves of PDA/amines layers on mica after in situ polymerization at pH 8.5 and 250 mM KCl. The concentrations of dopamine and amine are 2 mg/mL and 1 mg/mL, respectively.....51

Figure 3.10 Topographic AFM images and water contact angles before and after 4-h deposition for: (a, d) gold surface, (b,e) (3-Aminopropyl)triethoxysilane (APTES) surface, and (c, f) trichloro(octadecyl)silane (OTS) surface. The deposition conditions are as follows: Tris buffer solution (pH = 8.5) containing 250 mM KCl. The concentrations of dopamine and PEI are 2 mg/mL and 1 mg/mL, respectively. 52

Figure 3.11 Typical DMT modulus calculation of PDA/PEI coatings using peak force quantitative nanomechanical (PF-QNM) method. 53

Scheme 4.1 Schematic of the interacting surfaces in a) symmetric configuration and b) asymmetric configuration under aqueous condition (10 mM tris buffer, pH 8.5) during surface force measurements using a surface forces apparatus (SFA).....63

Figure 4.2 The effects of the TA/DETA mass ratio on a) the normalized cohesion forces F_{co}/R and cohesion energy (W_{co}) between TA/DETA coatings, and b) thickness of the TA/DETA coating. 69

Figure 4.3 X-ray photoelectron spectroscopy (XPS) characterization of a) pristine mica and b) TA/EDTA coating on mica surface. High-resolution XPS analysis of N1s on c) pristine mica and d) the TA/DETA coating. 70

Figure 4.4 Atomic force microscopy (AFM) images of as-formed TA/DETA coatings on mica surfaces using tris buffer solutions containing different TA/DETA mass ratios: a) 1:0, b) 1:1, c) 1:2, d) 1:5, e) 1:10, f) 1:15, g) 1:20 and h) 1:50. The concentration of TA is 2 mg/mL and the deposition time is 2 h. 74

Figure 4.5 AFM images and WCA of a) (3-Aminopropyl) triethoxysilane (APTES), b)

Titanium dioxide (TiO2), c) polystyrene (PS) and d) Octadecyltrichlorosilane (OTS) modified mica surface. 77

Figure 4.6 Force-distance profiles measured between the as-formed TA/DETA coating and different types of surfaces a) APTES surface, b) TiO2 surface, c) PS surface, d) OTS surface and e) Mica surface under tris buffer condition (10 mM, pH 8.5). 78

Figure 4.7 AFM images and WCA of TA/DETA coatings on different surfaces, including a) APTES surface, b) TiO2 surface, c) PS surface, d) OTS surface, e) Mica surface. The concentration of TA is kept as 2 mg/mL. The TA/DETA mass ratio is 1:10. The deposition time is 2 h. 80

Figure 5.1 Schematic of force measurement using a surface forces apparatus (SFA). Two opposing mica surfaces (radius R) coated with poly(pyrocatechol) (pPC) films first approached to each other until they come into contact to determine the thickness of confined layers (D_t), and then were separated, during which the adhesion force (F_{ad}) was measured. 90

Figure 5.2 Force-distance profiles measured between pPC coatings after in-situ deposition for 8 h in 50 mM bicine buffer solution at pH 8.5 containing 2mg/mL PC and different K^+ concentrations: a) 0, b) 10, c) 50, d) 100, e) 250 and f) 600 mM. 91

Figure 5.3 Schematic illustration of a) π-cation-π complex can induce bridging and promote the assembly of larger pPC aggregates; and b) binary cation–π binding pairs form due to excess K^+, leading to bridging abolishment and undermined assembly with smaller pPC aggregates. 97

Figure 5.4 Atomic force microscopy (AFM) topographic images of pPC film after deposition in PC solutions containing different K^+ concentrations for 8 h: a) 0, b)

10, c) 50, d) 100, e) 250 and f) 600 mM. 98

Figure 5.5 Force-distance profiles measured between pPC films after in-situ deposition for 8 h in PC solution containing 250 mM a) Li^+, b) Na^+, and c) NMe_4^+. e) The normalized adhesion forces (F_{ad}/R) and adhesion energy (W_{ad}) as a function of salt specie 99

Figure 5.6 AFM topographic images of pPC films on mica deposited in PC solution containing 250 mM a) Li^+, b) Na^+ and c) NMe_4^+. 100

Figure 6.1 a) Structures of dopa and phosphoserine residues, and PO_4-DHB. b) Schematic of SFA measurement. Two opposing curved mica surfaces (radius R) coated with poly(PO_4-DHB) films first approached to each other, then were compressed and separated to measure the adhesion force (F_{ad}) and thickness of confined films (D_T). 108

Figure 6.2 Force-distance profiles as a function of deposition time *t* of poly(PO_4-DHB) films in 150 mM KNO_3 buffer solution (50 mM bicine, pH 8.4) with initial concentration of PO_4-DHB as 2 mg/mL. The inset shows thickness ($D_T/2$) of each poly(PO_4-DHB) films. 110

Figure 6.3 a) Adhesion changes between poly(PO_4-DHB) films (1 hr deposition) in 150 mM KNO_3 background buffer solution after further addition of NO_3^-, HPO_4^{2-} or SO_4^{2-}. b) Force-distance profiles and thickness of poly(PO_4-DHB) coatings as a function of *t* in 150 mM $LiNO_3$ buffer solution. c) Binding energies of different anions to methyl amide of π-conjugated quinone (QMA)-K^+ pair in water obtained from DFT simulation. 111

Figure 6.4 a) Adhesion changes obtained from SFA experiments between two poly(PO_4-DHB) or two poly(pyrocatechol) films (1 hr deposition) in 150 mM KNO_3 background buffer solution with increased additional K^+ concentration.

Schematics for b) the abolishment of bridging with increasing concentration of K^+ due to the formation of more cation-π pairs in poly(pyrocatechol) coating and c) the formation of anion-π-cation complex in poly(PO_4-DHB) coating.....120

List of Abbreviations

mfps	mussel foot proteins
DOPA	3,4-dihydroxyphenyl-L-alanine
SFA	Surface forces apparatus
AFM	Atomic force microscopy
PDA	Polydopamine
TA	Tannic acid
DETA	Diethylenetriamine
EDL	Electric double layer
pPC	polypyrocatechol
PEG	Polyethylene glycol
PS	Polystyrene
ATRP	Atom transfer radical polymerization
MBI	Multiple beam interferometry
FECO	the fringes of equal chromatic order
JKR	Johnson−Kendall−Roberts
k	spring constant
D	Separation distance
D_{actual}	Actual separation distance

D_{applied}	Applied separation distance
F_{ad}	Adhesion force
W_{ad}	Adhesion energy per unit area
R	Curvature of the surfaces
λ_n^0, λ_{n-1}^0	wavelength of the nth and (n-1)th fringe at contact
λ_n^D, λ_{n-1}^D	wavelength of the nth and (n-1)th fringe at separation D
μ	refractive indices of the intermedium
μ_{mica}	refractive index of mica
XPS	X-ray photoelectron spectroscopy
TEPA	Tetraethylenepentamine
PEI	Polyethyleneimine
APTES	(3-Aminopropyl) triethoxysilane
OTS	Octadecyltrichlorosilane
TiO_2	Titanium dioxide
RMS	Root-mean-square
WCA	Water contact angle
D_t	confine layer thickness
NMe_4Cl	tetramethylammonium chloride
ToF-SIMS	time-of-flight negative secondary ion mass
EPR	electron paramagnetic spectroscopy

DFT	density functional theory
ESP	electrostatic potential

Chapter 1. Introduction

1.1 Mussel adhesion behavior

Living in the wind- and wave-swept seaside, marine mussels can effectively and robustly adhere to wet and salt-encrusted surfaces over million years of adaptation to nature. [1-4] Such tough and strong adhesion is surface-independent, which is essentially governed by the formation of tenacious byssus.[5-7] The schematic of mussel structure on sectional view is shown in **Figure 1.1a.** Anterior and posterior adductor muscles cooperatively control the open and close of the shell valves in mussel body, where the mussel foot can stretch out and retract back.[3] During an attachment process of mussel to a surface, mussel foot first stretches out to touch the substrate and explore for a suitable place to locate (generally the mussel prefers to high-energy surfaces and rough surfaces rather than low-energy surfaces and to smooth surfaces).[8,9] After the proper spot is found, the adhesive proteins are secreted and released from the ventral groove and the distal mussel foot followed by solidification once exposing to seawater condition to form the byssus strongly bonded on the target surface.[10-12] The byssus is consisted of four parts: adhesive plaque, thread comprising distal and proximal portions, stem and root.[2,3,13] The thread is derived from the root and joined at the stem, which utilizes the adhesive plaque to attach on the substrate and uses 12 byssal retractor muscles to control byssal tension.[14] As such, the holdfast of mussel to the substrate can be effectively realized through the tensile byssal threads connecting to mussel body and the adhesive plaques tightly attaching to the foreign surface.[6]

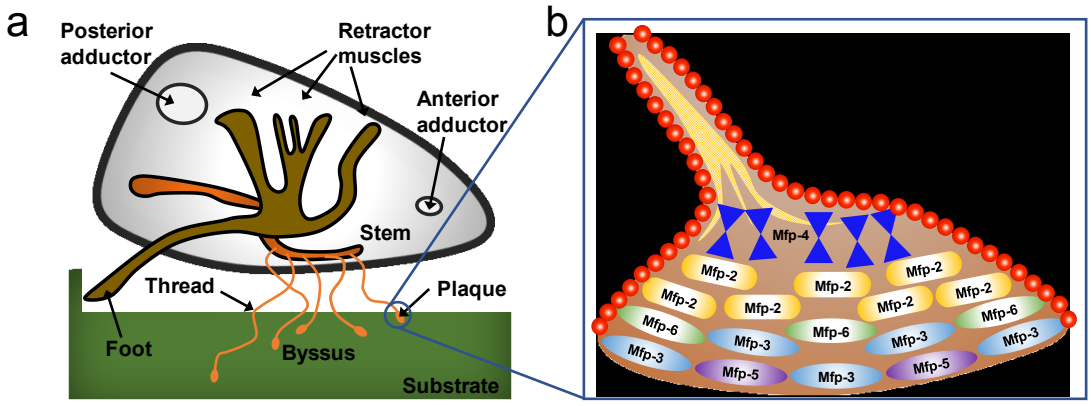

Figure 1.1 (a) The schematic of mussel structure on sectional view. (b) Schematic cross-section view of the mussel byssal plaque showing the approximate distribution of mussel foot protein distribution. (Reproduced from reference 15)

1.1.1 Mussel foot proteins

To unravel the mysterious interfacial behavior underlying the mussel adhesion behavior, much attention has focused on investigating the biochemistry of byssus thread and plaque. Prepolymerized collagens (preCOLs) and thread matrix proteins (tmp) are the major components of the fibrous core of byssal threads.[15-17] The entire thread and plaque are coated by a cuticle, of which a mussel foot protein (mfp) called mfp-1 is identified to be a key protein. The proteins that uniquely exist in plaque are mfp-2, mfp-3, mfp-4, mfp-5 and mfp-6. The location and distribution of mfp-1 to mfp-6 are shown in **Figure 1.1b.** Mfp-1, as a large protein (molecular weight ~ 108 kDa), is first identified to associate certainly with byssal cuticle, which contains ~ 15 mol% of amino acid 3,4-dihydroxyphenyl-L-alanie (DOPA).[18,19] The DOPA can undergo oxidation and complex with meta ions (especially Fe^{3+}) to form tough and rigid cuticles coated on the byssus for the protection of byssal treads and plaques.[20] Mfp-2 is the most abundant protein that widely presents in the

plaque, accounting for ~ 25 wt% of the plaque protein.[21] As a core of each plaque, mfp-2 contains ~ 5 mol% of DOPA, which can also form complexation bond with metal ions.[22] Mfp-3, abundantly distributed at the plaque interface, is believed to primarily contribute to the mussel interfacial adhesion between plaque and the substrate, which is mainly due to its structure flexibility (small mass of ~ 6 KDa) and the high DOPA content of ~ 20 mol%.[23,24] Mfp-4 is a 90 KDa protein with low DOPA content, which locates between the distal end of the thread and the proximal end of the plaque. It can regulate the links between precool from thread core and other mfp in plaque.[25] Mfp-5 also locates at the plaque interface. Similar to mfp3, mfp-5 also contains a high DOPA content at ~ 30 mol% and is confirmed to play a critical role in the strong adhesion between plaque and target surface,[26] implying that such adhesion behavior may closely related to DOPA. Located near to the plaque interface, mfp-6 is mainly responsible to effectively reduce dopaquinone to DOPA, mediating the redox balance to maintain the efficient adhesion of mfp-3 and mfp-5 to the surface.[27] In addition, it also provides necessary cross-link site between mfp at the plaque interface (i.e., mfp-3 and mfp-5) and mfp at bulk plaque (mfp-2).[28]

1.1.2 Interactions involved in mussel foot proteins

Robust attachment of mussel to target surface is essentially realized through two attractive interactions.[29] One is the interaction between mfps and underlying surface, which is defined as adhesion; and the other one is the interaction between mfps, which is called cohesion or cross-linking. Mussel mediates these two kinds of interaction behaviors via the secreted mfps to achieve strong and tough underwater adhesion. The widely existence of DOPA amino acid in mfps has been believed to play a critical role in enhancing both the adhesion and cohesion. Its unique molecular structure and versatile chemistry properties

endow DOPA with the capability of interacting with various materials/surfaces via multiple interactions. In marine environment, the catechol group (i.e., a benzene ring bearing two adjacent hydroxyl groups) in DOPA often undergoes the oxidation to quinone form (i.e., a benzene ring bearing two adjacent carbonyl groups), during which both of them are responsible for adhesion and cross-linking.[30]

DOPA-regulated various interaction behaviors are shown in **Figure 1.2**. Robust adhesion of mussel adhesive plaque to substrate often requires catechol or quinone groups to form strong attractive interactions with the surface. For inorganic surfaces (e.g., metals and metal oxides), catechol can bind to these surfaces through coordination bonds.[31] For the organic surfaces contains amines or thiols, quinone can bind to these surfaces through covalent binds.[32] For mineral surfaces carrying polar groups such as mica and silica, catechol, acting as both a hydrogen donor and receptor, can form hydrogen bond with them; and quinone, serving as a hydrogen receptor can also interaction with these surfaces through hydrogen bonding.[33] Due to the existence of benzene ring, both catechol and quinone can form hydrophobic interactions with hydrophobic surfaces. Besides, the electron-rich π-conjugated orbital in benzene ring allows catechol and quinone forming π-π interaction with surfaces containing aromatic compounds and cation-π interaction with surfaces carrying positive charges.[34] Strong cohesion in the bulk plaque and thread core needs the cross-linking occurring between catechol or quinone themselves. Multivalent metal ions such as Fe^{3+} and Ca^{2+} can serve as central atoms which enable the bridging of catechols through chelate bonds.[35] Boronic acid can form catechol-boronate complex by reacting with the hydroxyl groups in catechol at neutral and alkaline pH.[36] Such boronic ester bond is reversible, which can dissociate under acidic condition. The oxidation process of

catechol to quinone provides free radicals which can initiate the chemical cross-linking among catechols and quinones through coupling reaction.[30] The as-generated quinone groups can also react with amino groups existed in mfps via Michael addition or Schiff base reaction to realize the cross-linking of these adhesive proteins.[37,38] In addition, positively charged amino acids (*e.g.,* lysine) in mfps offer the bridging sites to interact with π-conjugated benzene groups through cation-π interaction, which are suggested to be an indispensable molecular interaction for the enhancement of mussel cohesion.[39] The various unraveled interactions involved in mussel adhesion shed light onto developing novel and practical bio-mimic adhesives and coatings for a wide range of engineering, bioengineering, biomedical applications.

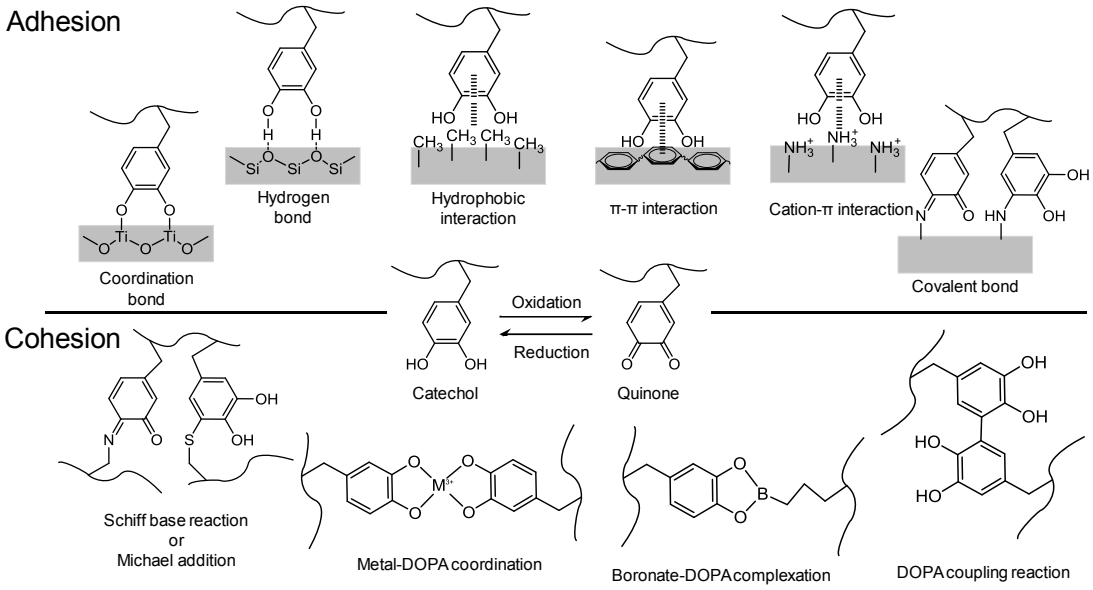

Figure 1.2 DOPA-mediated various non-covalent and covalent interactions in mussel foot proteins.

1.2 Mussel-inspired adhesive coatings

The mussel-inspired DOPA interfacial chemistry of mfps has attracted tremendous attention because its understanding inspires and guides the strategies for in-situ functionalizing material surfaces for biomedical and underwater engineering applications, such as wound dressing,[40] dental restoration,[41] biosensor,[42] bone tissue engineering[43] and under seawater pipeline repair.[44] Fabricating such adhesive coatings on target surfaces is realized by using catechol or its derivatives as a surface anchor to immobilize a variety of molecules or polymers for different functional purposes.[45-51] Generally, two strategies are often utilized for the surface functionalization. The first one is to prepare catecholic polymers by incorporating catechol groups to polymeric bones such as polyethylene glycol (PEG), polystyrene (PS), poly(methyl methacrylate-co-methacrylic acid) and polysaccharide, via copolymerization or polymer modification, and use them to functionalize surfaces by the "graft to" method.[52] The second one is to synthesize small catechol-ended initiator that can anchor to the surface via catechol followed by initiating the polymerization of various monomers from the surface via atom transfer radical polymerization (ATRP) to generate functional coating, which is called "graft from" method.[53] Despite both of the two methods have been utilized for surface functionalization, the process for synthesizing these catecholic molecules and polymers is often laboring and time-consuming. In addition, for some applications in biological system and marine environment requiring in-situ surface modification, the mild alkaline aqueous condition would induce the oxidation of catechol in artificial adhesives to quinone, that could not be able to adhere to some specific substrates such as mineral and metal oxide surface.[54] Thus, the development of a more readily coating strategy that can be applied in physiological

fluid and seawater is urgently needed. In 2007, Messersmith *et al.* reported a facile and versatile approach for surface modification called polydopamine deposition, which is the third strategy.[47] By simply dip-coating the surface in the weak alkaline aqueous solution containing dopamine (one kind of catecholamine), a polydopamine (PDA) coatings could form on almost all kinds of surfaces through the oxidative polymerization of dopamine. The obtained PDA coating bears an outstanding hydrophilicity and biocompatibility, which makes it as a suitable candidate for application in living organism.[55-57] The functional groups on PDA comprising catechol, quinone, amine and imine enable the PDA-coated material surfaces with post-functionalization accessibility, by which various molecules and polymers bearing different functions can be immobilized to the surfaces via co-depositing these chemical moieties with dopamine.[58,59] This find has attracted much attention and PDA coating has been utilized to introduce a wide range of micro/macromolecules such as peptides, proteins, inorganic nanoparticles, DNA and polysaccharides onto the surface to impart specific functions for certain applications.[60-62] Although this surface modification strategy has been widely expanded to many research directions and application areas, technically achieving adhesive coatings as robust as mussel adhesive protein is still a big challenge. The limitation is mainly due to that: In many practical bio- and marine-engineering applications, salt ions, especially cations, that ubiquitously exist in physiological fluid and seawater environments, can form a hydration layer tightly bound at the marine and physiological interfaces.[63] The hydrated salt layers could impose a physical barrier to impede the intimate contact between adhesives and surfaces, impairing the formation of high-performance adhesive coatings on wet substrate.[64] To conquer this problem and with the continuous efforts putting into the study of interfacial science, in

2015, Israelachvili *et al.* discovered an unexplored wet adhesion mechanism of marine mussel, which holds the key for mussel to surmount the adhesion failure induced by the adsorbed hydration ions.[1,65] The adjacent positioned DOPA-lysine provides a synergistic effect in underwater adhesion, in which cationic amino group on lysine "sweeps out" hydrated cations from the wet surface to allow the catechol binding to underlying substrate. Inspired by this mechanism, numerous works have been carried out to develop effective artificial wet adhesives for diverse surface functionalization applications by mimicking analogous molecular skeletons.[40,66-68] For example, Tren-Lys-Cam containing 2,3-dihydroxybenzoic acid and cationic lysine moieties and Tren-Arg-Cam containing 2,3-dihydroxybenzoic acid and arginine with a "three-legged" structure have been synthesized, which exhibit remarkable wet adhesion under salty water conditions.[21] Nevertheless, the preparation of these materials to control the DOPA and cationic group in an adjacent position is usually complicated, which may not be a good candidate to scale up for practical usage. In addition, the adhesion strength of such prepared adhesives could only be applied under acidic condition (pH ~3.3) and would be largely reduced when increasing the pH to 7.5 due to transition of dopacatechol to dopaquinone.[69] In view of these, in order to develop an effective and easy-to-implement strategy to further improve the coating's mechanical properties such as the achievement of enhanced adhesion and cohesion, the pace for in-depth understanding on the mussel-inspired surface chemistry and interaction mechanism cannot be ever slackened. Surface forces apparatus (SFA), as a powerful nanomechanical instruments for measuring various interactions between two curved molecularly smooth mica surfaces in vapors or liquids, have been widely applied to quantify the adhesion forces of biomacromolecule (e.g., mfps) and bio-mimic molecules/polymers (e.g., dopamine and

synthetic catecholic polymers) to various surfaces and between themselves.[4,70,71] Previously unraveled interaction mechanisms have provided very important insights onto the fundamental understanding of mussel-inspired interfacial adhesion chemistry and offers valuable guidance for developing advanced adhesive materials/coatings for associated applications.[65,72-75] Therefore, SFA is an ideal nano-instrument for us to further investigate the interaction mechanism underlying the mussel-inspired adhesion behavior and test the feasibility of coating strategy we hypothesized and proposed.

1.3 Objectives

Despite huge advances have been made in understanding mussel interaction behavior and development of mussel-inspired adhesives and coatings, the room for in-depth exploration of interaction mechanisms in mussel adhesive system and design and engineering of more readily, effective and scalable coating strategy are still existed. Therefore, the major objective of this thesis is to further investigate the nanomechanics involving in the wet deposition of mussel adhesive coating through systemically quantifying the interaction forces in the model catecholic systems by using SFA and to correlate the interaction behaviors to the adhesive coating properties such as chemical structure, coating thickness and surface roughness, which aim to providing implications onto designing and engineering coating strategies that can be applied under biological and seawater conditions. The detailed objectives are presented below.

(1) Design a facile and versatile method via integrating primary amine into PDA during dopamine polymerization that can achieve *in-situ* adhesion coatings formed on substrate surface under the model physiological fluid/seawater condition (i.e., high salinity and mild alkalinity). The validity of this proposed method is tested by using SFA to directly measure

the interaction forces and coating thickness of the as-formed adhesive coatings and employing atomic force microscopy (AFM) to characterize the coating properties such as surface roughness and surface morphology.

(2) Study the impact of the mass ratio of catecholic moiety and amine in catechol/amine deposition strategy on the interaction behavior and deposition capability of as-formed adhesive coatings via measuring the cohesion and adhesion forces between adhesive coatings and adhesive coating to various substrates and evaluating the coating capability such as coating thickness, surface roughness and surface morphology.

(3) Employ SFA to quantify the interaction forces combining with the evaluation of the as-formed adhesive coating properties in a model catecholic system coexisting with salt cations to further investigate the interaction mechanism underlying the formation of wet adhesive coating achieved by mussel adhesive proteins with specific focus on the role of ubiquitously existed monovalent cations (e.g., Na^+ and K^+) in physiological fluid and seawater on the interaction behavior and deposition performance of adhesive coatings.

(4) Utilizing SFA to investigate the intermolecular interactions in a model system containing anionic phosphate ester and π-conjugated catecholic moieties which abound in marine bioadhesives to further study the role of anions in wet adhesion of mussel, aiming at unravel the unexplored non-covalent interactions that may involve in marine mussel adhesion science.

1.4 Structure of the thesis

Chapter 1 introduces the underwater adhesion behavior of marine mussel, the mussel adhesive proteins and the interactions involved in the formation of mfp adhesive coating,

and reviews the development of mussel-inspired adhesive coating strategy. The objectives of this thesis are also included.

Chapter 2 describes the experimental methods utilized in this study, mainly including the working principles of the experimental techniques and the experiment setups.

Chapter 3 presents the measured interaction forces between *in-situ* formed PDA-amine coatings using SFA, and correlates the force results to the coating properties characterized by AFM, which demonstrates the validity of introducing primary amine to PDA to realize the formation of robust wet adhesive coating under physiological and seawater conditions. The interaction mechanism underlying the proposed strategy is also investigated.

Chapter 4 studies the variation of cohesion/adhesion strength and deposition capability during the formation of catechol-amine adhesive coatings with the mass ratio of catecholic moiety and amine, with implications on comprehensively understanding the interaction mechanism behind catechol-amine cooperative strategy for achieving the deposition of wet adhesive coating.

Chapter 5 reports a different and unexplored interaction mechanism that exists in the mussel-inspired wet adhesion behavior called π-cation-π interaction, which provides new insights into underwater bioadhesion and offers guidance to engineer novel adhesives with adhesion reversibility.

Chapter 6 reports an experimentally unexplored interaction mechanism that exists in the mussel-inspired wet adhesion behavior called anion-π interaction, which provides novel insights into the fundamental adhesion science of marine organism-secreted adhesives and shows great implications in biochemical and materials engineering processes.

Chapter 7 presents the major conclusions and original contributions of this thesis, and provides the perspectives of the further works in this research area.

Reference

(1) Maier, G. P.; Rapp, M. V.; Waite, J. H.; Israelachvili, J. N.; Butler, A. *Science* **2015**, *349*, 628-632.

(2) Lee, B. P.; Messersmith, P. B.; Israelachvili, J. N.; Waite, J. H. *Annual review of materials research* **2011**, *41*, 99-132.

(3) Waite, J. H. *J. Exp. Biol.* **2017**, *220*, 517-530.

(4) Oh, D. X.; Shin, S.; Yoo, H. Y.; Lim, C.; Hwang, D. S. *Korean J. Chem. Eng.* **2014**, *31*, 1306-1315.

(5) Waite, J. H. *Nat. Mater.* **2008**, *7*, 8-9.

(6) Waite, J. H.; Andersen, N. H.; Jewhurst, S.; Sun, C. *The journal of adhesion* **2005**, *81*, 297-317.

(7) Kavouras, J. H.; Maki, J. S. *Invertebr. Biol.* **2003**, *122*, 138-151.

(8) Aldred, N.; Ista, L.; Callow, M.; Callow, J.; Lopez, G.; Clare, A. *J. Royal Soc. Interface* **2006**, *3*, 37-43.

(9) Crisp, D.; Walker, G.; Young, G.; Yule, A. *J. Colloid Interface Sci.* **1985**, *104*, 40-50.

(10) Haris, V.; Springer Science & Business Media, 1990.

(11) Waite, J. H. *Int. J. Adhes. Adhes.* **1987**, *7*, 9-14.

(12) Waite, J. H. In *Book*; Springer, 1992; pp 27-54.

(13) Waite, J. H.; Qin, X.-X.; Coyne, K. J. *Matrix Biol.* **1998**, *17*, 93-106.

(14) Lowy, J.; Millman, B. *Philos. Trans. R. Soc. Lond. B. Biol. Sci.* **1963**, *246*, 105-148.

(15) Hwang, D. S.; Zeng, H.; Masic, A.; Harrington, M. J.; Israelachvili, J. N.; Waite, J. H. *J. Biol. Chem.* **2010**, *285*, 25850-25858.

(16) Holten-Andersen, N.; Fantner, G. E.; Hohlbauch, S.; Waite, J. H.; Zok, F. W. *Nat. Mater.* **2007**, *6*, 669-672.

(17) Qin, X.; Waite, J. H. *J. Exp. Biol.* **1995**, *198*, 633-644.

(18) Filpula, D. R.; Lee, S. M.; Link, R. P.; Strausberg, S. L.; Strausberg, R. L. *Biotechnol. Prog.* **1990**, *6*, 171-177.

(19) Taylor, S. W.; Waite, J. H.; Ross, M. M.; Shabanowitz, J.; Hunt, D. F. *J. Am. Chem. Soc.* **1994**, *116*, 10803-10804.

(20) Waite, J. H. *J. Biol. Chem.* **1983**, *258*, 2911-2915.

(21) Rzepecki, L. M.; Hansen, K. M.; Waite, J. H. *The Biological Bulletin* **1992**, *183*, 123-137.

(22) Inoue, K.; Takeuchi, Y.; Miki, D.; Odo, S. *J. Biol. Chem.* **1995**, *270*, 6698-6701.

(23) Burzio, L. A.; Waite, J. H. *Biochemistry* **2000**, *39*, 11147-11153.

(24) Even, M. A.; Wang, J.; Chen, Z. *Langmuir* **2008**, *24*, 5795-5801.

(25) Zhao, H.; Waite, J. H. *Biochemistry* **2006**, *45*, 14223-14231.

(26) Waite, J. H.; Qin, X. *Biochemistry* **2001**, *40*, 2887-2893.

(27) Zhao, H.; Waite, J. H. *J. Biol. Chem.* **2006**, *281*, 26150-26158.

(28) Yu, J.; Wei, W.; Danner, E.; Ashley, R. K.; Israelachvili, J. N.; Waite, J. H. *Nat. Chem. Biol.* **2011**, *7*, 588-590.

(29) Yu, J.; Springer, 2014.

(30) Yu, M.; Hwang, J.; Deming, T. J. *J. Am. Chem. Soc.* **1999**, *121*, 5825-5826.

(31) Lee, H. *Single-molecule mechanics of mussel adhesion. Proc. Natl. Acad. Sci. USA*

2006, *103*, 12999-13003.

(32) Bandara, N.; Zeng, H.; Wu, J. *J. Adhes. Sci. Technol.* **2013**, *27*, 2139-2162.

(33) Ahn, B. K.; Lee, D. W.; Israelachvili, J. N.; Waite, J. H. *Nat. Mater.* **2014**, *13*, 867-872.

(34) Lu, Q.; Danner, E.; Waite, J. H.; Israelachvili, J. N.; Zeng, H.; Hwang, D. S. *J. Royal Soc. Interface* **2013**, *10*, 20120759.

(35) Zeng, H.; Hwang, D. S.; Israelachvili, J. N.; Waite, J. H. *Proc. Natl. Acad. Sci. U.S.A.* **2010**, *107*, 12850-12853.

(36) Kan, Y.; Danner, E. W.; Israelachvili, J. N.; Chen, Y.; Waite, J. H. *PLoS ONE* **2014**, *9*.

(37) Fant, C.; Sott, K.; Elwing, H.; Hook, F. *Biofouling* **2000**, *16*, 119-132.

(38) Krogsgaard, M.; Nue, V.; Birkedal, H. *Chemistry–A European Journal* **2016**, *22*, 844-857.

(39) Kim, S.; Yoo, H. Y.; Huang, J.; Lee, Y.; Park, S.; Park, Y.; Jin, S.; Jung, Y. M.; Zeng, H.; Hwang, D. S. *ACS Nano* **2017**, *11*, 6764-6772.

(40) Kord Forooshani, P.; Lee, B. P. *J. Polym. Sci., Part A: Polym. Chem.* **2017**, *55*, 9-33.

(41) Li, J.; Celiz, A.; Yang, J.; Yang, Q.; Wamala, I.; Whyte, W.; Seo, B.; Vasilyev, N.; Vlassak, J.; Suo, Z. *Science* **2017**, *357*, 378-381.

(42) Brault, N. D.; Gao, C.; Xue, H.; Piliarik, M.; Homola, J.; Jiang, S.; Yu, Q. *Biosens. Bioelectron.* **2010**, *25*, 2276-2282.

(43) Kao, C.-T.; Lin, C.-C.; Chen, Y.-W.; Yeh, C.-H.; Fang, H.-Y.; Shie, M.-Y. *Mater. Sci. Eng. C* **2015**, *56*, 165-173.

(44) Lee, L.-H. In *Book*; Springer, 1988; pp 5-29.

(45) Dalsin, J. L.; Messersmith, P. B. *Materials today* **2005**, *8*, 38-46.

(46) Gao, C.; Li, G.; Xue, H.; Yang, W.; Zhang, F.; Jiang, S. *Biomaterials* **2010**, *31*, 1486-1492.

(47) Lee, H.; Dellatore, S. M.; Miller, W. M.; Messersmith, P. B. *Science* **2007**, *318*, 426-430.

(48) Han, H.; Wu, J.; Avery, C. W.; Mizutani, M.; Jiang, X.; Kamigaito, M.; Chen, Z.; Xi, C.; Kuroda, K. *Langmuir* **2011**, *27*, 4010-4019.

(49) Kang, S. M.; You, I.; Cho, W. K.; Shon, H. K.; Lee, T. G.; Choi, I. S.; Karp, J. M.; Lee, H. *Angew. Chem., Int. Ed.* **2010**, *49*, 9401-9404.

(50) Liu, J.; Li, J.; Yu, B.; Ma, B.; Zhu, Y.; Song, X.; Cao, X.; Yang, W.; Zhou, F. *Langmuir* **2011**, *27*, 11324-11331.

(51) Wei, Q.; Pei, X.; Hao, J.; Cai, M.; Zhou, F.; Liu, W. *Adv. Mater. Interfaces.* **2014**, *1*, 1400035.

(52) Wach, J. Y.; Malisova, B.; Bonazzi, S.; Tosatti, S.; Textor, M.; Zürcher, S.; Gademann, K. *Chemistry–A European Journal* **2008**, *14*, 10579-10584.

(53) Edmondson, S.; Osborne, V. L.; Huck, W. T. *Chemical society reviews* **2004**, *33*, 14-22.

(54) Min, Y. **2011**.

(55) Ho, C.-C.; Ding, S.-J. *J. Biomed. Nanotechnol.* **2014**, *10*, 3063-3084.

(56) Liu, Y.; Ai, K.; Lu, L. *Chem. Rev.* **2014**, *114*, 5057-5115.

(57) Yang, H.-C.; Luo, J.; Lv, Y.; Shen, P.; Xu, Z.-K. *J. Membr. Sci.* **2015**, *483*, 42-59.

(58) Jeon, E. K.; Seo, E.; Lee, E.; Lee, W.; Um, M.-K.; Kim, B.-S. *Chem. Commun.* **2013**, *49*, 3392-3394.

(59) Zhang, C.; Yang, H.-C.; Wan, L.-S.; Liang, H.-Q.; Li, H.; Xu, Z.-K. *ACS Appl. Mater. Interfaces* **2015**, *7*, 11567-11574.

(60) Choi, B.-H.; Choi, Y. S.; Hwang, D. S.; Cha, H. J. *Tissue Engineering Part C: Methods* **2012**, *18*, 71-79.

(61) Ham, H. O.; Liu, Z.; Lau, K. A.; Lee, H.; Messersmith, P. B. *Angew. Chem., Int. Ed.* **2011**, *50*, 732-736.

(62) Lee, H.; Rho, J.; Messersmith, P. B. *Adv. Mater.* **2009**, *21*, 431-434.

(63) Pashley, R. *Adv. Colloid Interface Sci.* **1982**, *16*, 57-62.

(64) Israelachvili, J.; Wennerström, H. *Nature* **1996**, *379*, 219-225.

(65) Rapp, M. V.; Maier, G. P.; Dobbs, H. A.; Higdon, N. J.; Waite, J. H.; Butler, A.; Israelachvili, J. N. *J. Am. Chem. Soc.* **2016**, *138*, 9013-9016.

(66) North, M. A.; Del Grosso, C. A.; Wilker, J. J. *ACS Appl. Mater. Interfaces* **2017**, *9*, 7866-7872.

(67) Wang, R.; Li, J.; Chen, W.; Xu, T.; Yun, S.; Xu, Z.; Xu, Z.; Sato, T.; Chi, B.; Xu, H. *Adv. Funct. Mater.* **2017**, *27*, 1604894.

(68) Zhao, Y.; Wu, Y.; Wang, L.; Zhang, M.; Chen, X.; Liu, M.; Fan, J.; Liu, J.; Zhou, F.; Wang, Z. *Nat. Commun.* **2017**, *8*, 1-8.

(69) Yu, J. In *Book*; Springer, 2014; pp 21-30.

(70) Li, L.; Zeng, H. *Biotribology* **2016**, *5*, 44-51.

(71) Park, S.; Kim, S.; Jho, Y.; Hwang, D. S. *Langmuir* **2019**, *35*, 16002-16012.

(72) Gebbie, M. A.; Wei, W.; Schrader, A. M.; Cristiani, T. R.; Dobbs, H. A.; Idso, M.; Chmelka, B. F.; Waite, J. H.; Israelachvili, J. N. *Nat. Chem.* **2017**, *9*, 473-479.

(73) Yang, B.; Jin, S.; Park, Y.; Jung, Y. M.; Cha, H. J. *Small* **2018**, *14*, 1803377.

(74) Degen, G. D.; Stow, P. R.; Lewis, R. B.; Andresen Eguiluz, R. C.; Valois, E.; Kristiansen, K.; Butler, A.; Israelachvili, J. N. *J. Am. Chem. Soc.* **2019**, *141*, 18673-18681.

(75) Lim, C.; Huang, J.; Kim, S.; Lee, H.; Zeng, H.; Hwang, D. S. *Angew. Chem., Int. Ed.* **2016**, *55*, 3342-3346.

Chapter 2. Experimental Techniques

2.1 Surface forces apparatus (SFA)

Surface forces apparatus (SFA) has been widely utilized for the measurement of various interaction forces between surfaces as a function of separation distance under various conditions such as air, vapors, aqueous and non-aqueous media. The first apparatus, as a prototype of SFA, was described by Tabor and Winterton in 1969, by which the separations between interacting surfaces could be down to 5-30 nm with a distance resolution of 0.3 nm. [1, 2,3] After that, with the improvement of such technique, Israelachvili *et al*. developed the first version of SFA in the 1970s, which was called SFA MK I.[4] Later, SFA has being upgraded, with different versions of SFA such as SFA MK II, SFA MK III and SFA 2000 have been developed in the next few decades.[5-8] SFA 2000 was employed in this study, which is easier to assemble and manipulate due to the less parts included while still retaining the merits of pervious versions. The larger chamber in SFA 2000 compared to the SFA MK series make it capable of integrating other attachments and modulus for various experimental researches.[6,9]

Figure 2.1 shows schematic diagram of SFA 2000.[10] The components of SFA 2000 mainly include the micrometers, the main chamber, the main stage which consists of one central simple-cantilever spring and attachments base, low disk holder and upper disk holder mounted with a piezoelectric tube. The separation distance between the upper and lower surfaces can be controlled by four different controls, which is over several orders of magnitude rang from angstrom to millimeter. The hand-driven differential micrometer enables the moving distance of lower surface with a coarse control in which the distance

range is 2 mm and the precision is 200 nm, and a medium control over range of 200 μm at 50 nm precision. The motor-driven micrometer can precisely control the distance of lower surface with the range of 10 mm and precision down to 2 Å. The movement of upper surface can be modulated by a piezoelectric tube over a range of 1 μm with a precision of less than 1 Å to realize the extra-fine distance control.

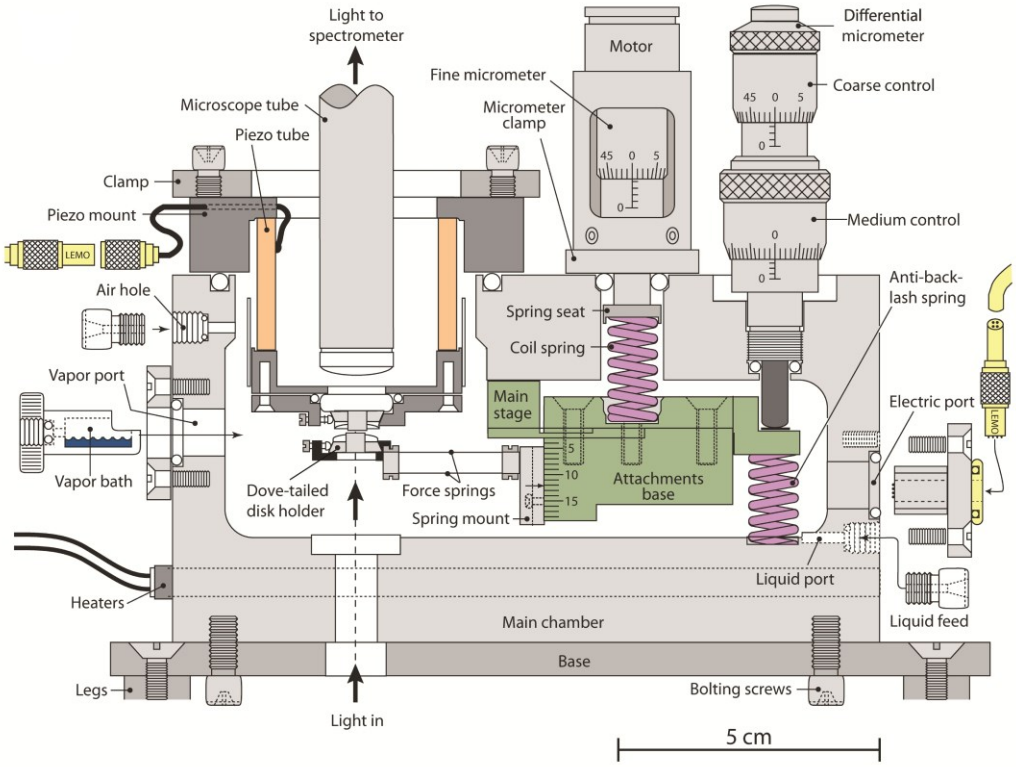

Figure 2.1 Section view of SFA 2000 through the center of the apparatus.[10]

2.1.1 SFA experiment setup

Figure 2.2 shows the typical SFA experiment setup.[11-14] In the SFA technique, two back-silvered (thickness ~50 nm) molecularly smooth mica sheets with thickness 1-5 μm are glued onto two cylindrical silica disks (radius R=2 cm). The two surfaces are mounted

to the upper and lower disk holders in SFA chamber with a crossed-cylinder configuration, and the interaction of which is locally equivalent to a sphere of radius R approaching a flat surface when their separation D is much smaller than R. The absolute surface separation during the experiment is monitored and measured *in situ* and in real time by employing an optical technique called multiple beam interferometry (MBI) using the fringes of equal chromatic order (FECO). The light path shown in **Figure 2.2** exhibit that the FECO generated in the spectrometer can be recorded by a video camera. Thus, based on the positions and shapes of the FECO, the actual distance between two surfaces and their surface morphology as can be obtained, meanwhile the refractive index of the in-between confined medium can also be calculated.

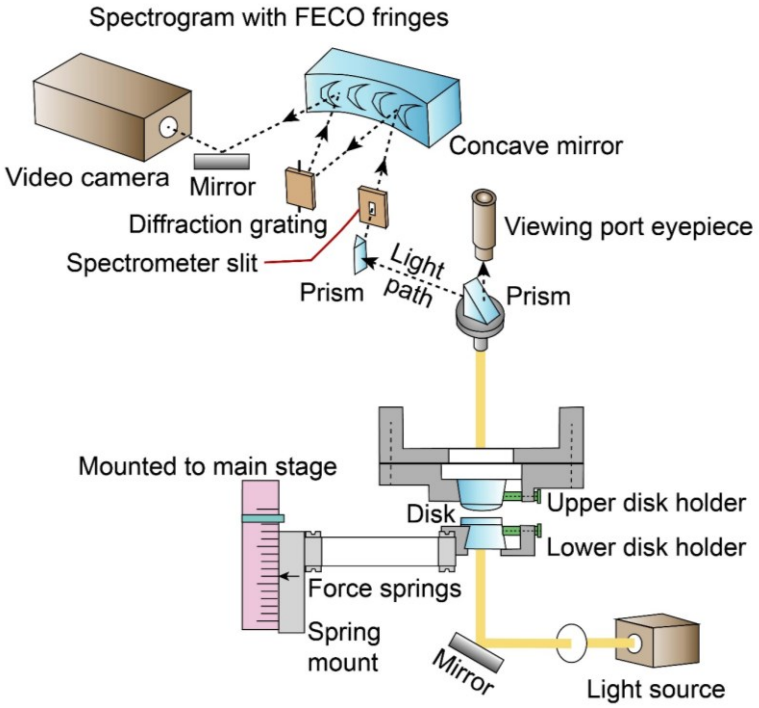

Figure 2.2 Schematic of a typical SFA experimental setup.[15]

2.1.2 Force measurement using SFA

The interaction force F between two surfaces is measured based on the Hook's law:

$F=k\Delta x$, where k is the spring constant supporting the lower surface and Δx is the spring deflection which can be determined using an equation $\Delta x = D_{actual} - D_{applied}$.[6] The actual separation distance D_{actual} is obtained from the position of FECO shown in the screen, and the applied separation distance $D_{applied}$ is determined according to the moving distance of the surface driven by the motor or piezoelectric tube. The resolution of the force measured using SFA is ~10 nN and the accuracy of distance measurement is 1 Å. During a typical force measurement, the two surfaces are firstly driven to approach and come into contact for a certain time followed by a separation process, during which the interaction region is simultaneously monitored by using the FECO fringes for the determination of surface deformation and their separation distance. The force F between two curved surfaces of radius R can be plotted as a function of their separation distance D and normalized using F/R to describe the interaction between any other curved surfaces with a known radius. In addition, the interaction energy per unit area between two flat surface $W(D)$ can be correlated to the measured force $F(D)$ based on the Johnson−Kendall−Roberts (JKR) model, where $W(D)= F(D)/2\pi R$.[16] The adhesion energy per unit area W_{ad} can be calculated from the measured adhesion force F_{ad} through the equation $W_{ad} = F_{ad}/1.5\pi R$ for soft deformable surfaces with relatively large curvature and adhesion.[10] The reference distance (D = 0) was determined from an independent measurement of the contact point of two bare mica surfaces in air. The confined coating thickness on mica surfaces could be determined via the shift of the FECO wavelength before and after coating.

2.1.3 Multiple beam interferometry (MBI)

An optical technique called the optical multiple beam interferometry (MBI) was utilized to generate a series of colored interference fringes with equal chromatic order (viz.,

fringes of equal chromatic order (FECO)) to monitor and determine the distance between two interacting surfaces with high accuracy in SFA experiments. The schematic of FECO is shown in **Figure 2.3**. MBI was first developed to measure the topography of single surfaces in 1948,[17] and later it was extended for the measurement of absolute separation between two surfaces, confined film thickness as well as its surface deformation and the refractive index of the intermedium.[18] The accuracy for the separation and thickness measurement can achieve to 1 Å. In a typical SFA experiment, two opposite mica surfaces coated by the silver as a highly reflective layer form an interferometer. It could be noted that the FECO appear as doublet since mica is a birefringent material which has two refractive indices. The optical path with the lower refractive index leads to the relatively lower wavelength fringe called the β component, and the higher refractive index leads to the relatively higher wavelength called γ component. When the two surfaces are at contact, the white light passed rough them would reflect multiple times to generate the interference light with certain wavelengths o leave the interferometer. The emerging light beam focused on to the slit of a spectrometer by a microscope objective lens are split up based on its discrete wavelengths λ_n^0 (n = 1, 2, 3, …) and form an array of colored fringes (FECO) in the exit port shown in **Figure 2.3a**. When the two mica sheets have the same thickness (i.e., symmetric system), if the surfaces are separated by a separation distance D (**Figure 2.3b**), the separation distance D can be determined by correlating with the measured FECO wavelength of λ_n^0, $\lambda_{n-1}^0, \lambda_n^D$ and λ_{n-1}^D using the equation (2.1).

$$\tan(2\pi\mu D/\lambda_n^D) = \frac{2\bar{\mu}\sin\left[\pi\left(1-\lambda_n^0/\lambda_n^D\right)/\left(1-\lambda_n^0/\lambda_{n-1}^0\right)\right]}{(1+\bar{\mu}^2)\cos\left[\pi\left(1-\lambda_n^0/\lambda_n^D\right)/\left(1-\lambda_n^0/\lambda_{n-1}^0\right)\right]\pm(\bar{\mu}^2-1)} \qquad (2.1)$$

where $\bar{\mu} = \mu_{mica}/\mu$, μ and μ_{mica} is the refractive indices of the intermedium

confined between two mica surfaces and mica at λ_n^D. In Eq. 2.1, '+' refers to the odd order fringes (n odd), and '−' refers to the even order fringes (n even).

When the distance between the surfaces is small (D < 30 nm), Taylor series expansions can be used to obtain the approximate expressions for the trigonometric functions in Eq. (2.1), which is show in Eqs (2.2a) and (2.2b).

$$D = \frac{nF_n(\lambda_n^D - \lambda_n^0)}{2\mu_{mica}} \qquad \text{for n odd} \qquad (2.2a)$$

$$D = \frac{nF_n(\lambda_n^D - \lambda_n^0)\mu_{mica}}{2\mu^2} \qquad \text{for n even} \qquad (2.2b)$$

where $nF_n = \lambda_{n-1}^0 / (\lambda_{n-1}^0 - \lambda_n^0)$, in which n is the order of interference fringe F_n can be regarded as a correction factor which considers the dispersion effects and the phase changes at the mica-silver interface. For wavelength of the incident light at λ ~ 500 nm, F_n ≈ 1.024 + 1/n. The distance D can be monitored through measuring the wavelength shift of the FECO patterns (i.e., an n odd and adjacent n-1 even fringe).

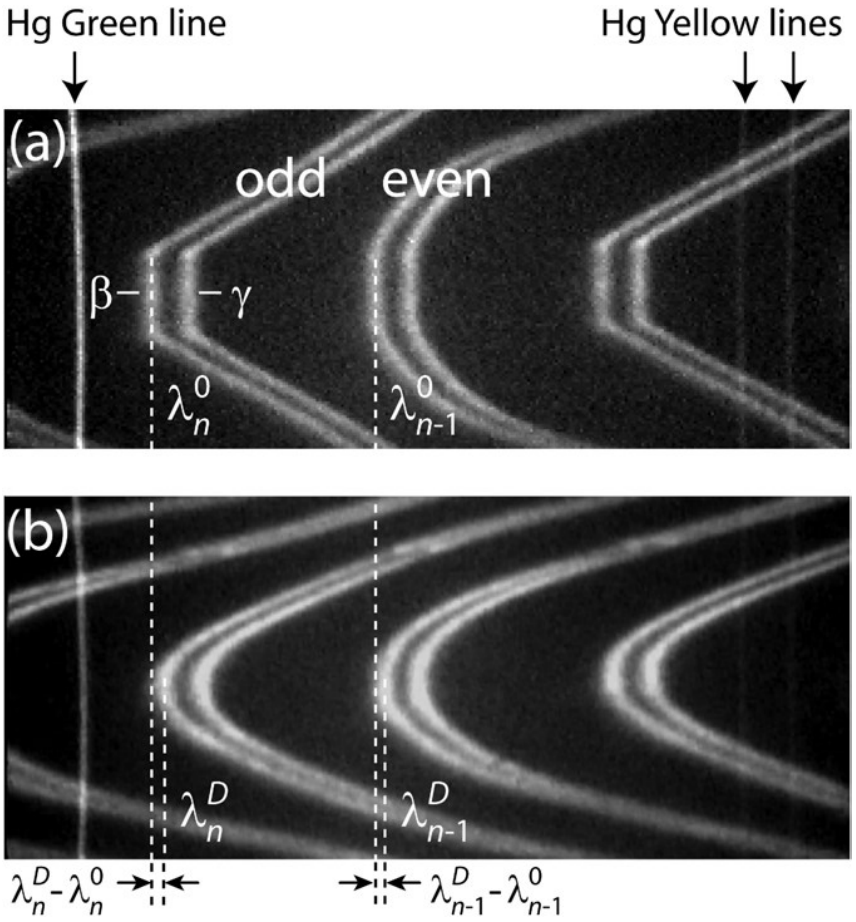

Figure 2.3 FECO of mica surface in air (a) under adhesive (separation distance $D_0 = 0$) and (b) separated by a distance D.[10]

2.2 Other techniques

In addition to the SFA technique, other techniques such as atomic force microscope (AFM), X-ray photoelectron spectroscopy (XPS) and UV–vis spectrophotometer, contact angle goniometer and zetasizer nano were also utilized for my research work.

AFM (Bruker, Santa Barbara, CA) was used to characterize the morphology of the substrate surfaces before and after the phenol/amine deposition using a tapping mode. During surface imaging in tapping mode, a cantilever with proper spring constant is driven to oscillate and to slightly scan over the sample surface. The morphology difference on the

surface could result in the change of tip-sample separation, affecting the oscillation amplitude. Thus, to maintain a constant oscillation amplitude, a feed back loop would adjust the height of tip. This adjustment due to the surface morphology change could be recorded in the system and generate a topographic image of the surface.

The surface elemental composition and chemical structure of prepared coating surfaces was analyzed using XPS ((Kratos AXIS 165) equipped with a monochromated Al Ka X-ray source (h_v= 1486.7 eV). The pressure of analysis chamber was controlled < 5 × 10^{-10} Torr during the experiments. Detailed elemental chemical information was obtained by analyzing the high-resolution spectra of specific element. C 1s peak of background hydrocarbon at 284.8 eV was used as a standard for charge compensation.

UV–vis adsorption of the as-prepared deposition solution was characterized using a UV-vis spectrophotometer (Evolution 300) for the semi-quantitative determination of highly conjugated organic compounds during polymerization. The adsorption wavelength of lights depends on the electron transitions from the ground to the excited state. The UV-vis absorbance intensity at specific wavelengths is closely related to the concentrations of the corresponding functional groups. By comparing the variation of characteristic peak adsorption intensity at these specific wavelengths over time in the obtained UV-vis spectra, detailed information on polymerization process of catecholamine and phenol moieties could be obtained.

The wettability of each sample surfaces was determined using a contact angle goniometer through a sessile drop method. A droplet of Milli-Q water was dropped on the surface and then an image processing software was employed to fit the shape of the drop to determine the contact angle.

A Zetasizer Nano (Malvern Instruments Ltd., United Kingdom) was used to determine the zeta potential and particle size of as-formed phenol/amine aggregates at varying mass ratios.

The composition characterizations of target surfaces were performed by Time-of-flight secondary ion mass spectrometry (ToF-SIMS) analysis in negative-ion mode using an TOF.SIMS 5 instrument (IONTOF GmbH, Münster, Germany) with a 25 keV Bi^+ primary ion source.

Electron paramagnetic spectroscopy (EPR) spectrum was acquired using a Bruker Elexys E500 spectrometer, which could detect and characterize the free radicals during the reaction process.

References

(1) Tabor, D.; Winterton, R. *Proc. Royal Soc. Lond* **1969,** 312, (1511), 435-450.

(2) Israelachvili, J.; Tabor, D. *Wear* **1973,** 24, (3), 386-390.

(3) Israelachvili, J.; Tabor, D. *Nat. Phys. Sci.* **1972,** 236, (68), 106.

(4) Israelachvili, J.; Adams, G. *Nature* **1976,** 262, (5571), 774-776.

(5) Israelachvili, J. N.; McGuiggan, P. M. *J. Mater. Res.* **1990,** 5, (10), 2223-2231.

(6) Israelachvili, J.; Min, Y.; Akbulut, M.; Alig, A.; Carver, G.; Greene, W.; Kristiansen, K.; Meyer, E.; Pesika, N.; Rosenberg, K. *Rep. Prog. Phys.* **2010,** 73, (3), 036601.

(7) Horn, R.; Israelachvili, J.; Pribac, F. *J. Colloid Interface Sci.* **1987,** 115, (2), 480-492.

(8) Klein, J. *J. Chem. Soc., Faraday Trans.* **1983,** 79, (1), 99-118.

(9) Israelachvili, J. N. Academic press: 2011.

(10) Israelachvili, J.; Min, Y.; Akbulut, M.; Alig, A.; Carver, G.; Greene, W.; Kristiansen, K.; Meyer, E.; Pesika, N.; Rosenberg, K.; Zeng, H. *Rep Prog Phys* **2010,** 73, (3).

(11) Zeng, H.; Tian, Y.; Anderson, T. H.; Tirrell, M.; Israelachvili, J. N. *Langmuir* **2008,** 24, (4), 1173-1182.

(12) Teng, F. C.; Zeng, H. B.; Liu, Q. X. *J. Phys. Chem. C* **2011,** 115, (35), 17485-17494.

(13) Natarajan, A.; Xie, J. G.; Wang, S. Q.; Liu, Q. X.; Masliyah, J.; Zeng, H. B.; Xu, Z. H. *J. Phys. Chem. C.* **2011,** 115, (32), 16043-16051.

(14) Natarajan, A.; Kuznicki, N.; Harbottle, D.; Masliyah, J.; Zeng, H. B.; Xu, Z. H.

Langmuir **2014,** 30, (31), 9370-9377.

(15) Gong, L.; Xiang, L.; Zhang, J.; Chen, J.; Zeng, H. *Langmuir* **2019,** 35, (48), 15914-15936.

(16) Israelachvili, J. N. Academic press: 2015.

(17) Israelac.Jn. *J Colloid Interf Sci* **1973,** 44, (2), 259-272.

(18) Israelachvili, J. **1973,** 44, (2), 259-272.

Chapter 3. Tough and Alkaline-Resistant Mussel-Inspired Wet Adhesion with Surface Salt Displacement via Polydopamine-Amine Synergy

3.1 Introduction

Robust and durable wet polymer adhesives have received continually increased attention and have been applied in a wide range of fields such as biomedical materials for wound dressing,[1,2] dental restoration,[3,4] sustainable sealants for under seawater pipeline repair[5,6] and various functional coatings for surface modification.[7-13] Under physiological and seawater environments, hydrated salt ions are able to form tightly bound hydration layer on substrate surface, which is regarded as a physical barrier to the adhesives and adhesive coatings. This barrier can tremendously undermine the adhesion forces and even result in adhesion failure when the adhesive materials are attempted to adhere to the wet surfaces.[14,15] Therefore, up to date, the great challenge for developing biomimetic underwater adhesive materials is still how to displace or evict the hydration layer for achieving strong and durable adhesion under practical aqueous conditions (e.g., physiological environment and seawater).

In nature, marine mussels have remarkable adhesion capability underwater to effectively remove the hydration layer, and thus facilitate their attachment to various wet mineral surfaces. The firm attachment of the mussel byssus plaques on wet surfaces is attributed to the cooperative effect of the secreted proteins (i.e., mussel foot proteins (mfps)).[16-19] Extracting natural mfps from mussels has been considered as a promising candidate for superior wet adhesive materials. However, one gram of mfps has to be obtained from several thousand mussels *via* a time-consuming extraction and purification

process, significantly limiting its large-scale practical applications. Hence, developing synthetic wet adhesives inspired by marine mussels is of vital importance to practical applications. Previous studies found that the building blocks of these adhesive mfps mainly comprise of 20-30 mol % 3,4-dihydroxyphenylalanine (DOPA) and ~ 20 mol % cationic lysine,[2,17] and they are usually in adjacent positions (**Figure 3.1a**). Recently, the neighboring arrangements of these two functionalities, DOPA and cationic lysine, in mfps were demonstrated to possess synergistic interplay to realize robust underwater adhesion, whereby cationic lysine displaces the surface hydrated salt ions and then DOPA moieties binds to the surfaces.[14] Inspired by this principle, many efforts have been devoted to developing a variety of biomimetic wet adhesive materials. A biomimic siderophore-cyclic trichrysobactin, containing catecholic 2,3-dihydroxybenzoic acid (DHBA) and cationic lysine moieties, was synthesized and exhibited remarkable wet adhesion.[11] Subsequently, a series of artificial wet adhesives were developed for various surface adhesion applications by employing analogous molecular skeletons.[20-22] Nevertheless, two crucial challenges still exist in the applications of these wet adhesive materials. First, to control the DOPA and cationic groups located in adjacent positions and prevent the oxidation of catechol groups on DOPA, the preparation of these materials usually suffers from complex chemical synthesis and excessive solvent/energy consumption. Second, the adhesion strength of the aforementioned artificial adhesives could be dramatically reduced by almost a factor of 2 when increasing the solution pH from 3.3 to 7.5, which could be further lowered when applied under seawater condition (pH ~ 8.5).[23] The greatly weakened wet adhesion capability under neutral or weak alkaline pH conditions is mainly because that, under these pH conditions, catechol residues can be readily oxidized into corresponding dopaquinone

moieties, hence weakening their adhesion to solid surfaces. The rigorous requirement to keep acidic pH condition significantly restricts the practical applications of these synthetic wet adhesives in biomedical engineering and oceaneering. Therefore, it is of practical and fundamental importance to develop an easy-to-implement, universal and scalable method to fabricate strong and durable wet adhesive materials sustainable under physiological and seawater environments.

It has been well known that dopamine or its derivatives can readily form the "bio-glue" polydopamine (PDA) to toughly adhere to various substrates in weak alkaline solutions (e.g., pH 8.5) *via* a oxidative self-polymerization process.[7-9,24-26] These previous studies have indicated that unlike most synthetic catechol-based underwater adhesives, PDA-based adhesive materials can maintain strong adhesion under weak alkaline conditions. However, their adhesion to wet surfaces could be easily diminished under relatively high KCl concentration (e.g., 100 mM), exhibiting a poor salt displacement ability.[27] Herein, inspired by the underwater adhesion mechanism based on the synergistic effect of cationic lysine and DOPA, as well as the "bio-glue" PDA chemistry, we report a facile, one-step and scalable method to realize surface salt displacement and robust wet adhesion under mild alkaline and relatively high saline environment through incorporating cationic amines into PDA adhesive (**Figure 3.1b**). During a typical polymerization process, dopamine undergoes self-oxidation followed by cyclization to form several intermediates including leucodopaminechrome, dopaminechrome, 5,6-dihydroxyindole (DHI) and 5,6-indolequinone.[7] The primary and secondary amino groups on amines can react with carbon-carbon double bond on aryl groups of these intermediates through nucleophilic addition named Michael addition.[9] It should be mention that this addition reaction can also occur

between primary amino groups on dopamine to carbon-carbon double bond on another dopamine. However, due to the intramolecular cyclization of a vast majority of dopamine and the higher density of amino group on amines compared to dopamine, in our adhesive materials, the major products are formed by PDA and different kinds of cationic amines (**Figure 3.1c**) located in adjacent position, which is very analogous to the molecular structure of mfps. By using surface forces apparatus (SFA), the interaction forces between the PDA-amine coatings were precisely quantified, and the impact of amines types and contents on the adhesion behavior was also investigated. To our best knowledge, it is the *first* report to achieve robust mussel-inspired wet adhesion under mild alkaline and high salinity conditions. The facile approach developed in this work and the force measurement results enrich and broaden the library of wet adhesion from acidic condition to weak alkaline environment, with great implications for the development and application of new underwater adhesives and coatings in biomedical and industrial engineering.

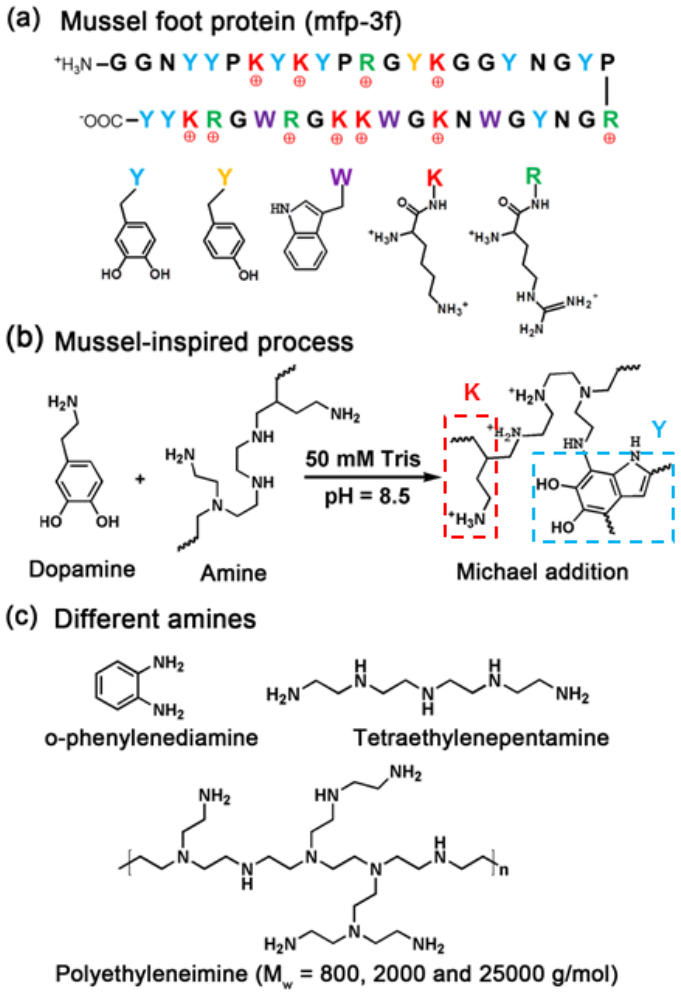

Figure 3.1 (a) Primary sequences of mussel foot protein (mfp-3f) and molecular structure of according amino acid residues. (b) Schematic illustration of mussel-inspired process based on the one-step reaction of dopamine and primary amine under Tris buffer.

3.2 Materials and Experimental Methods

3.2.1 Materials

Dopamine hydrochloride, o-phenylenediamine, tetraethylenepentamine (TEPA), polyethyleneimine (PEI) with difference molecular weights (M_w = 800, 2000 and 25000 g/mol) were purchased from Sigma-Aldrich (Canada). Potassium chloride (KCl) and tris-(hydroxymethyl)aminomethane were obtained from Fisher Scientific (Canada). All

chemical reagents were used without further purification. The water used in all experiments was deionized and ultrafiltered to 18.2 MΩ·cm with a Milli-Q water system (USA).

3.2.2 Fabrication and characterization of PDA and PDA/amines coatings

Dopamine hydrochloride (2 mg/mL), amine (1 mg/mL) and KCl (250 mM) were dissolved in Tris buffer solution (pH = 8.5, 50 mM), and then fresh mica was immersed in the above solution for 1 h at 25 °C. Subsequently, as-deposited mica was washed by deionized water and blow dried by nitrogen gas before use. UV-vis absorption of the deposition solutions was measured with an ultraviolet spectro-photometer (UV 2450, Shimadzu, Japan). The surface morphology and chemical component of the as-deposited samples were characterized by atomic force microscope (MFP-3D, Asylum Research, Santa Barbara, CA) and X-ray photoelectron spectroscopy (XPS, PerkinElmer, USA).

3.2.3 Surface force measurements using surface forces apparatus (SFA)

The normalized force (F/R)-distance (D) profiles and adhesion forces of PDA/amine layers were measured by employing an SFA according to the experimental setup reported previously.[27-30] In this work, Tris buffer solutions (pH=8.5, 50 mM) containing 250 mM KCl were used in all the force experiments, under which the electrical double layer interaction was significantly suppressed.[31] In a typical force measurement, back-silvered thin mica sheets (1-5 μm) were first glued onto cylindrical silica disks (R = 2 cm). Then, the two surfaces were mounted into the SFA chamber in a cross-cylinder configuration, and the interaction of which is equivalent to a sphere of radius R approaching a flat surface when the surface separation D is much smaller than R based on the Derjaguin

approximation.[32] Freshly prepared dopamine/amine Tris buffer solution (pH=8.5, 50 mM) with 250 mM KCl was injected between the two mica surfaces. The normal forces were measured based on the Hooke's law. The measured adhesion or "pull-off" force F_{ad} is correlated to the adhesion energy per unit area between two flat surfaces W_{ad} by $F_{ad}/R = 1.5\pi W_{ad}$, based on the Johnson-Kendall-Roberts (JKR) model.[33,34]

During a typical SFA measurement, two surfaces were moved to approach each other to reach a "hard wall" distance (defined as the confined distance which barely changed with increasing the normal load or pressure) and kept in contact for a certain time followed by separation. The thicknesses of PDA/amine films and surface separation during force measurements were obtained by employing the fringes of equal chromatic order (FECO) based on multiple beam interferometry technique coupled with SFA. In this work, the reference distance (D = 0) was determined at the contact between two bare mica surfaces in air.

3.3 Results and Discussion

In this study, SFA was employed to perform the surface force measurements. Mica has been used as the model substrate surface because its molecularly smooth basal plane could eliminate the influence of substrate roughness on force measurements. It is known that a tightly bound hydration layer can form on mica basal surface when immersed in saline water due to the adsorption of hydrated cations (e.g., K^+) on the negatively charged mica surface.[10] As illustrated in **Figure 3.2a,** the interaction forces between two *in situ* formed PDA or PDA/amine layers on mica surfaces in a symmetric configuration were quantified under a model aqueous conditions with high-salinity and mild alkalinity (i.e., Tris buffer solution with 250 mM KCl, pH = 8.5). Polyethyleneimine (PEI) was chosen as

one kind of primary amines to be integrated with PDA in our study, because its rich primary amine moieties were expected to be facilely located in adjacent position of the catechol groups on PDA via Michael addition reaction[35] to mimic the synergistic adhesion structures in mfps under high-salinity condition.[14] The interaction forces between the as-formed PDA layers in symmetric configuration, PDA/PEI layers (with different adding ratio of PDA and PEI) and PEI layers were measured.

Figure 3.2b shows the force-distance profiles of the as-formed PDA layers (yellow curves), and PDA/PEI layers (blue curves). For pure PDA case, after the *in situ* polymerization of dopamine in 250 mM KCl (pH 8.5) for 1 h, the two surfaces were brought to approach to each other. When the distance between the two surfaces decreased to ~ 30 nm, a long-range repulsion was observed. As AFM image shows (**Figure S3.2** in the Supporting Information) sparsely scattered large PDA nanoaggregates adsorbed on the substrate surface and electric double layer interactions are significantly suppressed under the high salinity condition, this long-range repulsion is most likely originated from the steric forces from the deposited PDA aggregates and the rough coating surfaces during approaching. The confined thickness of PDA is less than 1 nm (**Figure S3.1** in the Supporting Information), suggesting that the PDA aggregates could be significantly compressed or mostly squeezed out from the contact region under compression, which further evidences that the adhesion of PDA on the substrates is very weak.[36] Accordingly, during separation, no obvious adhesion was measured that also implied the weak adhesion of the PDA to the substrates. This phenomenon shows a distinctive difference with previously reported results that with aqueous solution of low salinity, PDA could deposit on various substrates.[37] Therefore, the presence of salts with high concentration most likely

has a negative influence on the adhesion of PDA to the substrates and may also impair the polymerization of dopamine. To better understand this phenomenon and the associated mechanism, the polymerization process of dopamine with or without the presence of 250 mM KCl was monitored by using a UV-vis spectrophotometer. It can be observed that the UV-vis spectra under both conditions are almost the same (**Figure 3.3**), suggesting that high concentration of KCl has no influence on dopamine polymerization in bulk solution. Thus, the phenomenon that no adhesion was observed in SFA measurement can only be attributed to the very weak adhesion of sparsely formed PDA layers on the substrates, which is most likely because the introduced hydrated K^+ forms a hydration layer on the substrate, suppressing the adhesion of PDA on mica surface.

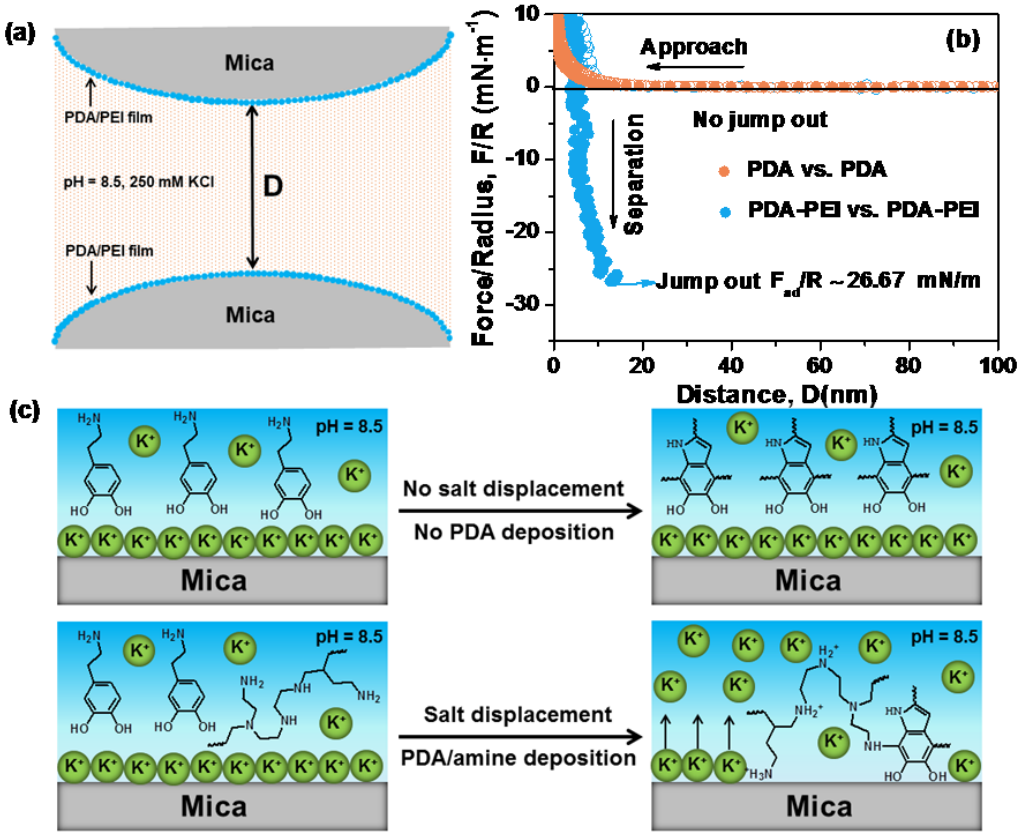

Figure 3.2 (a) Schematic of surface force measurements between two PDA layers or

PDA/PEI layers deposited on mica via SFA. (b) Force-distance curves of PDA layers and PDA/PEI (Mw = 800 g/mol) layers on mica surfaces after in situ polymerization in Tris buffer solution (pH=8.5, 50 mM) with 250 mM KCl. The concentration of dopamine and PEI is 2 mg/mL and 1 mg/mL, respectively. (c) Schematic illustration of salt displacement and deposition process of dopamine and dopamine/amine systems. Primary amine group shows a positive charge at pH 8.5.

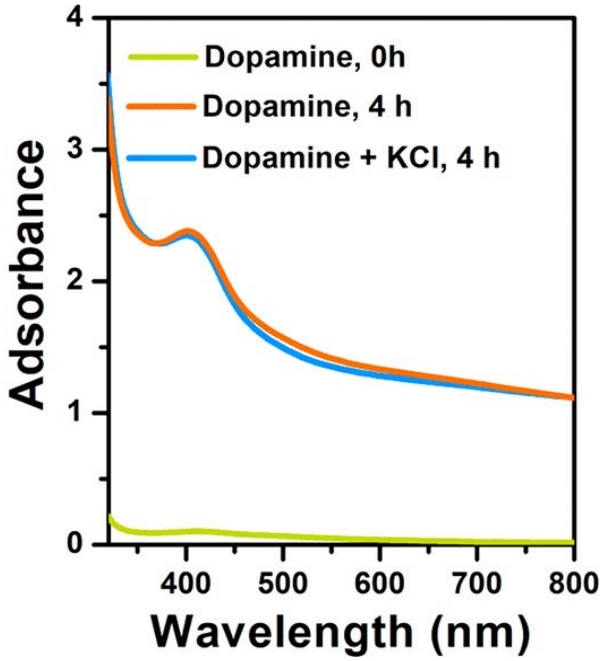

Figure 3.3 UV-vis spectra associated with the polymerization process of dopamine in tris buffer solution (pH=8.5, 50 mM) with or without the existence presence of 250 mM KCl.

For the as-formed PDA/PEI layer, as shown in **Figure 3.2b**, by optimizing the mass ratio between PEI and PDA to 2:1, the confined thickness of PDA-PEI was detected around 2.5 ± 0.4 nm, of which the successful deposition was further confirmed by AFM imaging (**Figure S3.5** in the Supporting Information) and XPS characterization (**Figure S3.6** in the Supporting Information). During surface separation, strong cohesion ($F_{ad}/R \sim 26.67$ mN/m,

W_{ad} ~ 5.66 mJ/m^2) was detected. The strong cohesion measured between PDA-PEI surfaces in symmetric configuration suggestions that the adhesion between PDA-PEI coating and mica substrate most likely is higher than 26.67 mN/m. Such a strong adhesion has not been reported previously for mussel-inspired polymers containing DOPA moieties or derivatives under the selected aqueous condition (i.e., 250 mM KCl, pH 8.5),[23,38,39]implying that this strategy may be further extended to develop underwater adhesives for practical applications under weak alkaline environment. In comparison, the cohesion between two pure PEI layers was measured as only F_{ad}/R ~ 2.61 mN/m (W_{ad} ~ 0.55 mJ/m^2) (**Figure S3.4** in the Supporting Information), indicating that pure amines cannot result in such strong cohesion. Therefore, the above results demonstrate that the introduction of PEI via this method is able to assist PDA to form PDA/PEI adhesive coatings with robust underwater adhesion for deposition on mica surfaces. The possible interaction mechanism proposed for the wet adhesion of PDA/PEI layers is illustrated in **Figure 3.2c**. For the PDA/PEI system, PEI, with positive charges at pH 8.5, can react with the dopamine quinone motif of PDA via Michael addition reaction to endow as-polymerized aggregates with positively charged amino groups.[35,40,41] The amino groups can facilitate the displacement of hydrated ions (i.e., K^+ ions) to allow PDA to intimately attach to the mica surfaces. In view of the pure PDA system, although dopamine can normally be polymerized into PDA in high salinity solutions, the as-polymerized PDA nanoparticles are negatively charged,[37] resulting in poor capability of evicting the surface hydration layer to realize the wet adhesion. By varying the mass ratios between PEI and dopamine from 2 : 0.5 to 2 : 2, it is found that the cohesion interaction first increases from ~ 7.36 mN/m (W_{ad} ~ 1.55 mJ/m^2) at the mass ration 2 : 0.5 to ~ 26.67 mN/m (W_{ad} ~ 5.66

mJ/m^2) at the mass ratio 2 : 1, and then deceases to ~ 3.28 mN/m (W_{ad} ~ 0.70 mJ/m^2) at the mass ratio 2 : 2 (**Figure 3.5** and **Figure S3.3** in the Supporting Information), implying the interaction between *in situ* formed PDA-PEI coatings could be significantly influenced by the content of PEI (as further discussed below).

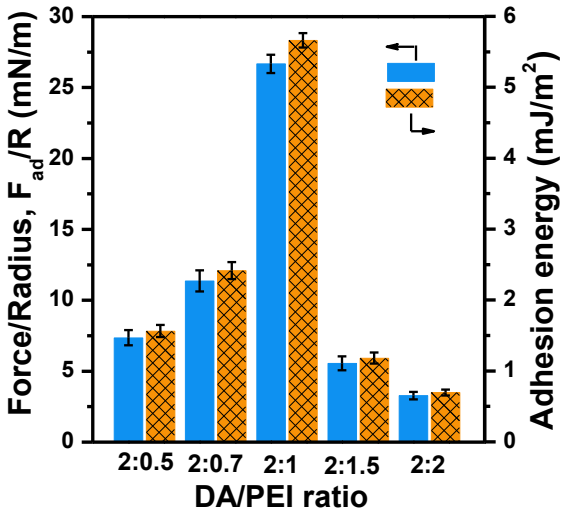

Figure 3.4 Adhesion force and adhesion energy of PDA/PEI (Mw = 800 g/mol) layers with different PEI concentrations deposited on mica after in situ polymerization in Tris buffer solution (pH=8.5, 50 mM) with 250 mM KCl. The mass ratios of dopamine (DA) and PEI (DA/PEI) are 2:0.5, 2:0.7, 2:1, 2:1.5 and 2:2.

It should be noted here that the strong cohesion force could be repetitive and maintained at ~26.00 mN/m (W_{ad} ~5.52 mJ/m^2) during the consecutive force measurements at the same interaction position (**Figure S3.7** in the Supporting Information), indicating that the cohesion is reversible and mostly contributed from non-covalent interactions. Considering the reversibility of the interaction force and the structure properties of PDA/PEI, cation-π interaction between positively charged amino group and cyclized indole is expected to play an important role in this system.[31,42-44] The "bridging effect"

might exist between two cyclized indole groups by interacting with one amino group through cation-π interaction. Based on this assumption, we increased the salt concentration during the force measurement process from 250 mM KCl to 600 mM KCl. As shown in **Figure 3.5b**, the cohesion force and cohesion energy drastically reduce to 3.43 mN/m and 0.73 mJ/m^2, respectively, as compared to that shown in **Figure 3.5a** ($F_{ad}/R \sim 26.09$ mN/m and $W_{ad} \sim 5.54$ mJ/m^2 in 250 mM KCl). The reduced cohesion is most likely due to the competition of abundant K^+ with cationic PEI in forming cation-π interactions with PDA, thus weakening the wet adhesion. Therefore, the origin of strong robust wet adhesion is most likely attributed to the cation-π interactions between PEI and PDA. In addition, even with the weakened cation-π interaction, the PDA/PEI adhesive layer is still able to deposit on the mica surface under 600 mM KCl (**Figure S3.8** in the Supporting Information), suggesting the hydrated salt layer under even higher salt concentrations could be disrupted and displaced by the PDA/PEI moieties, realizing robust adhesion to the underlying substrate surfaces.

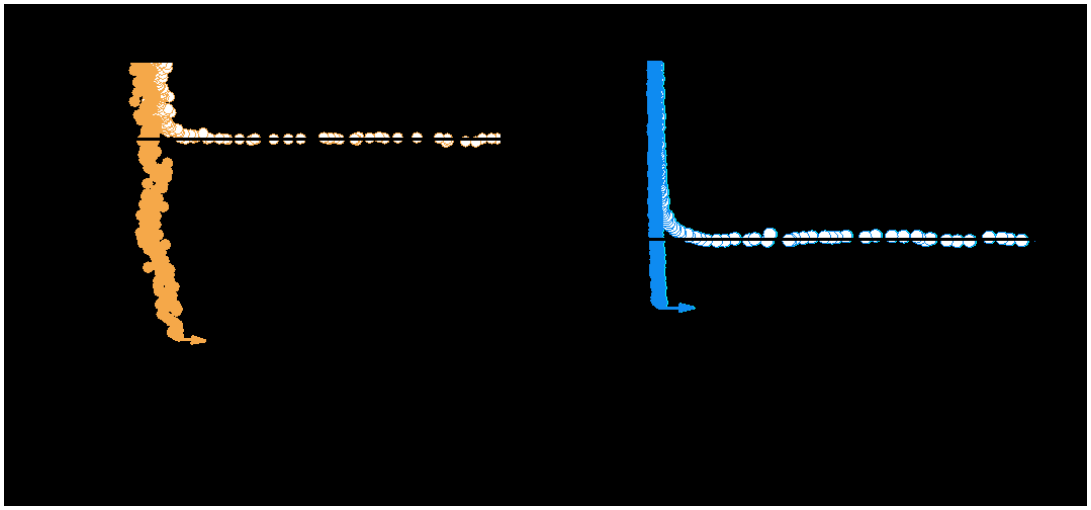

Figure 3.5 (a, b) Force-distance curves of PDA/PEI (Mw = 800 g/mol) films coated on mica after in situ polymerization in Tris buffer solution (pH=8.5, 50 mM) with (a) 250 mM

KCl and (b) 600 mM KCl. The concentrations of dopamine and PEI (Mw = 800 g/mol) are fixed at 2 mg/mL and 1 mg/mL, respectively.

To further demonstrate the feasibility of this universal coating strategy relied on the cooperative effect of primary amine groups and PDA for realizing the strong wet adhesion, different types of amines containing primary amine moieties were chosen and tested, including o-phenylenediamine, tetraethylenepenamine and PEI with different molecular weights (**Figure 3.1c**). **Figure 3.6** shows the AFM images of PDA/different amines coatings on mica, demonstrating that all these amines can assist PDA to remove the hydration salt layer to achieve successful deposition underwater. The measured force results in the PDA-amine systems show obviously enhanced adhesion and coating capability than the pure PDA case in 250 mM KCl (**Figure 3.7** and **Figure S3.9** in the Supporting Information). The interaction force is found to be firstly strengthened and then weakened with increasing the molecular weight of amines, which exhibits the same trend of interaction with increasing the PEI content as mentioned above. The tunable interaction, related to the molecular weight and mass content of amines, might be explained as follows: large molecular weight and high mass content of amine generally lead to less PDA moieties in the deposited layers, and introducing redundant amino groups would occupy the cation-π interaction sites, abolishing the "bridging effect" between indole groups, weakening the cohesion between the PDA-PEI coatings. On the other hand, low molecular weight and low mass content of amine lack of sufficient amino groups to generate "bridging effect" between the cation-π interactions sites, which thereby cannot enhance the cohesion between the coatings. Therefore, the synergy effect of PDA and amines, highly depending on the amine content and position, plays a vital role in underwater adhesion, providing a

facile approach to develop advanced functional materials with robust wet adhesion capability.

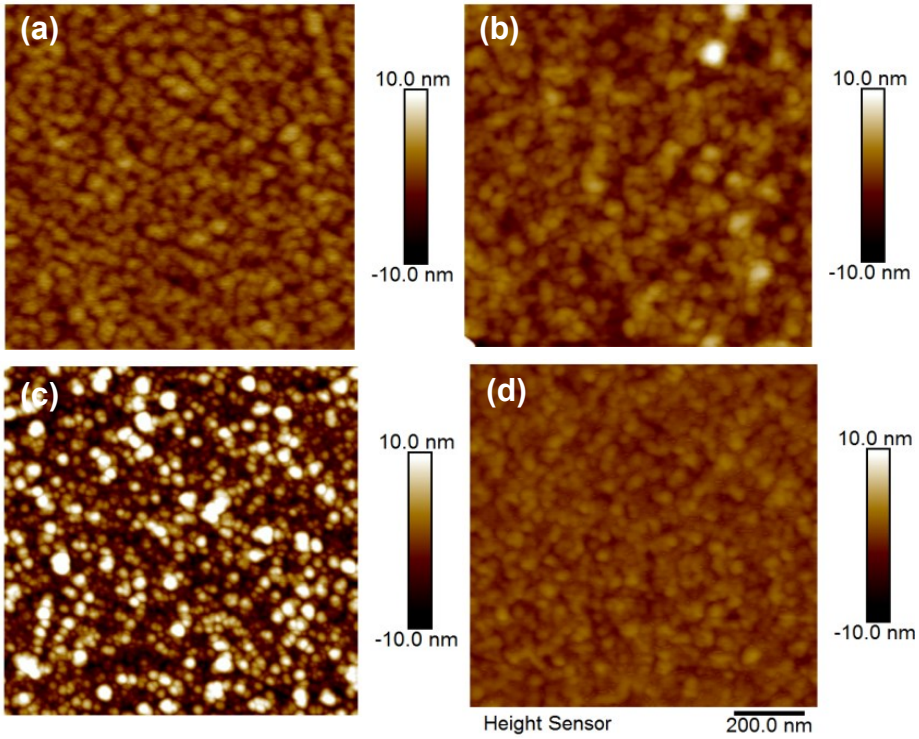

Figure 3.6 AFM topographic images of PDA and PDA/different amines coatings on mica: (a) PDA/o-phenylenediamine, (b) PDA/tetraethylenepenamine, (c) PDA/polyethyenimine (Mw = 2000 g/mol) and (d) PDA/polyethyenimine (Mw = 25000 g/mol). The polymerization conditions are Tris buffer solution (pH=8.5, 50 mM) with 250 mM KCl for 4 h. The concentrations of dopamine and amine are 2 mg/mL and 1 mg/mL, respectively.

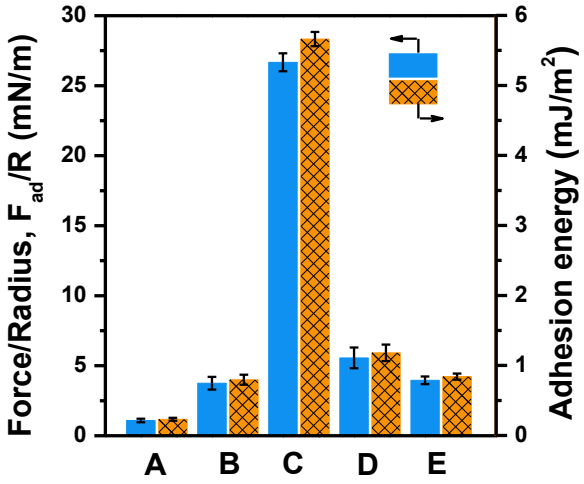

Figure 3.7 Adhesion force and adhesion energy of PDA/different amines layers: (A) PDA/o-phenylenediamine, (B) PDA/tetraethylenepenamine, (C) PDA/PEI (Mw = 800 g/mol), (D) PDA/PEI (Mw = 2000 g/mol) and (E) PDA/PEI (Mw = 25000 g/mol), deposited on mica after in situ polymerization in Tris buffer solution (pH=8.5, 50 mM) with 250 mM KCl. The concentrations of dopamine and amines were fixed at 2 mg/mL and 1 mg/mL, respectively.

The underwater curing properties are widely regarded as one of the critical factors for polymer adhesives applied under wet conditions. During a typical adhesive coating process, adhesive materials are first delivered on the substrate surface and then bind to the surface, followed by fast curing into load-bearing materials *via* different methods, including change of pH or salt as a trigger,[45,46] oxidative crosslinking[47] and solvent exchange.[48] All these curing processes require some additional conditions or specific post-processing treatments. Therefore, how to complete the curing process within a reasonably short time or even fabricate a curing-free process is a practical challenge for the adhesive materials. In this work, PDA/PEI aggregates are first formed in the solutions via oxidative polymerization, cross-linking and noncovalent assembly process, and then deposit on the substrate surfaces

to form robust PDA/PEI-based nanofilms.[37,49] It is worth noting that this mussel-inspired deposition is a typical "up-down" method and does not require the above-mentioned traditional curing processes to turn into load-bearing coating materials. AFM imaging has been applied to characterize the morphology and Young modulus of PDA/PEI layers underwater to investigate load-bearing properties of the adhesive materials. It is evident from the AFM images of PDA/PEI layers under water (**Figure 3.8a** in the Supporting Information) remain almost the same as that in air without obvious swelling behaviors. In addition, the Young's modulus can reach up to around 4.1 GPa via a typical Derjaguin-Muller-Toporov (DMT) modulus calculation using peak force quantitative nanomechanical (PF-QNM) method (**Figure 3.8b** and **Figure S3.10** in the Supporting Information), which is higher than many typical adhesive polymers, such as polystyrene and polymethyl methacrylate.[50-52]

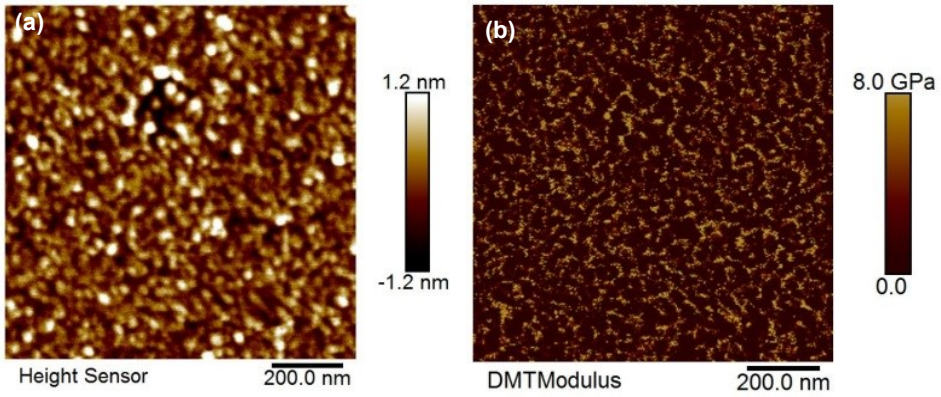

Figure 3.8 (a) AFM height image of PDA/PEI coatings underwater. (b) AFM modulus mapping of PDA/PEI coatings. Each DMT modulus map was analyzed at least using three cross sections across the modulus map. Young's modulus is around 4.1 GPa.

3.4 Conclusions

In summary, this work reports a robust and facile strategy to enable mussel-inspired PDA with tough wet adhesion *via* the introduction of amines as functional moieties during dopamine polymerization. Through optimizing the mass ratio between PEI and dopamine, the adhesive can exhibit strong adhesion strength even in mild alkaline solutions with high salinity due to the synergetic effect between PEI and PDA, which has never been realized in synthetic catechol-based adhesives previously. AFM imaging in combination with the SFA force results reveal that the incorporation of PEI plays dual critical roles: displacing or evicting the surface hydrated salt layer facilitated by the positively charged amine groups for allowing PDA/PEI moieties binding strongly to the substrate surface and inducing cation-π interactions between PDA/PEI moieties to enhance cohesion interaction. This study provides useful implications to guide the design and development of versatile mussel-inspired wet adhesives and coating materials.

3.5 Supporting information

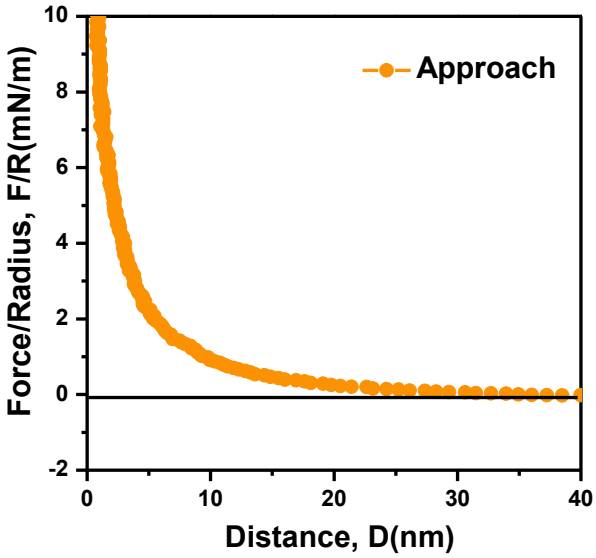

Figure S3.1 Force-distance curves on approach of PDA layers on mica surfaces after in situ polymerization at pH = 8.5 and 250 mM KCl. The concentration of dopamine is 2 mg/mL.

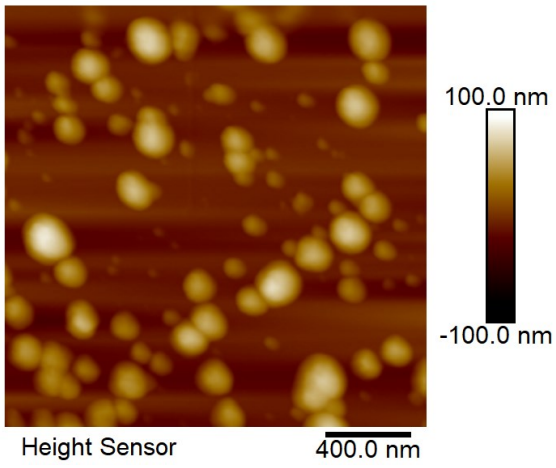

Figure S3.2 AFM images of PDA coatings on mica. The polymerization conditions are at pH 8.5 and 250 mM KCl for 4 h. The concentration of dopamine is 2 mg/mL.

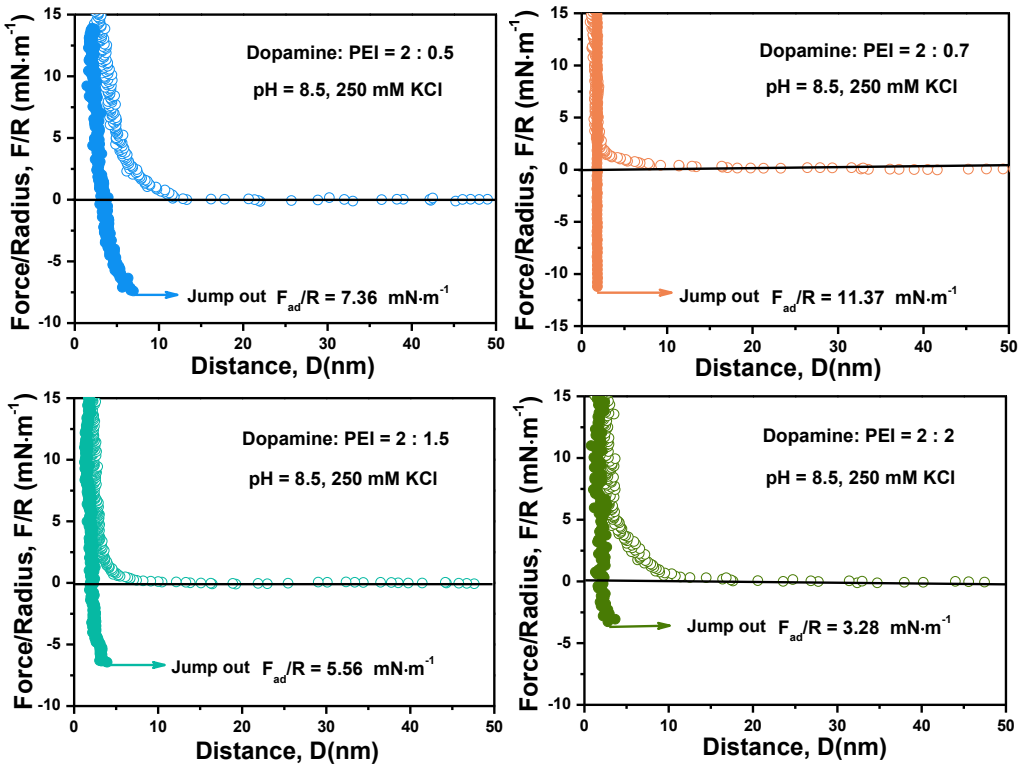

Figure S3.3 Force-distance curves of PDA/PEI (Mw = 800 g/mol) layers with different mass ratios on mica after in situ polymerization at pH 8.5 and 250 mM KCl. The concentrations of dopamine and PEI (Mw = 800 g/mol) are 2 mg/mL and 1 mg/mL, respectively.

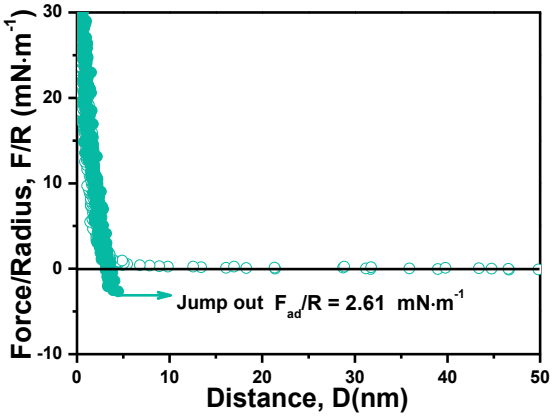

Figure S3.4 Force-distance curve between pure PEI 800 layers absorbed onto mica at pH

8.5 and 250 mM KCl.

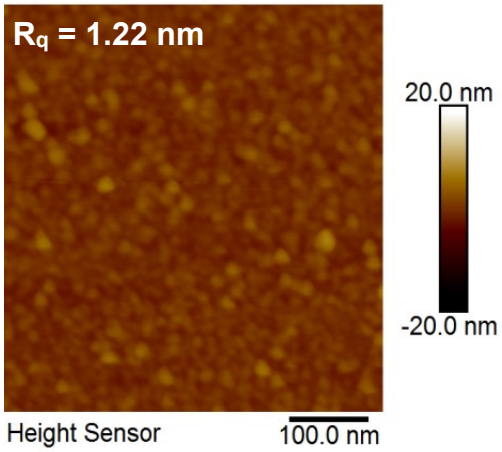

Figure S3.5 AFM images of PDA/PEI (Mw = 800 g/mol) coatings on mica. The polymerization conditions are at pH 8.5 and 250 mM KCl for 4 h. The concentration of dopamine and PEI is 2 mg/mL and 1 mg/L, respectively

.

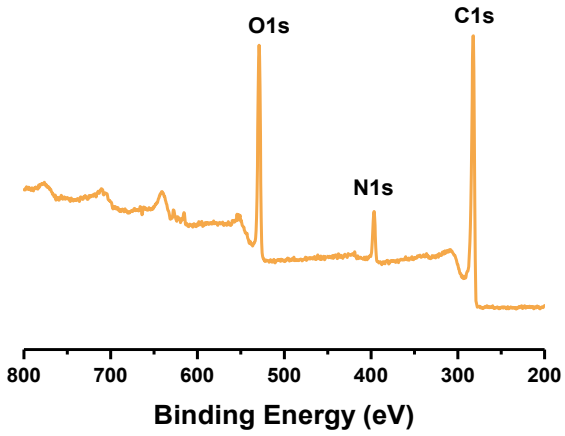

Figure S3.6 PS spectrum of PDA/PEI (Mw = 800 g/mol) coatings on mica. The polymerization conditions are at pH 8.5 and 250 mM KCl for 4 h. The concentration of dopamine and PEI is 2 mg/mL and 1 mg/L, respectively.

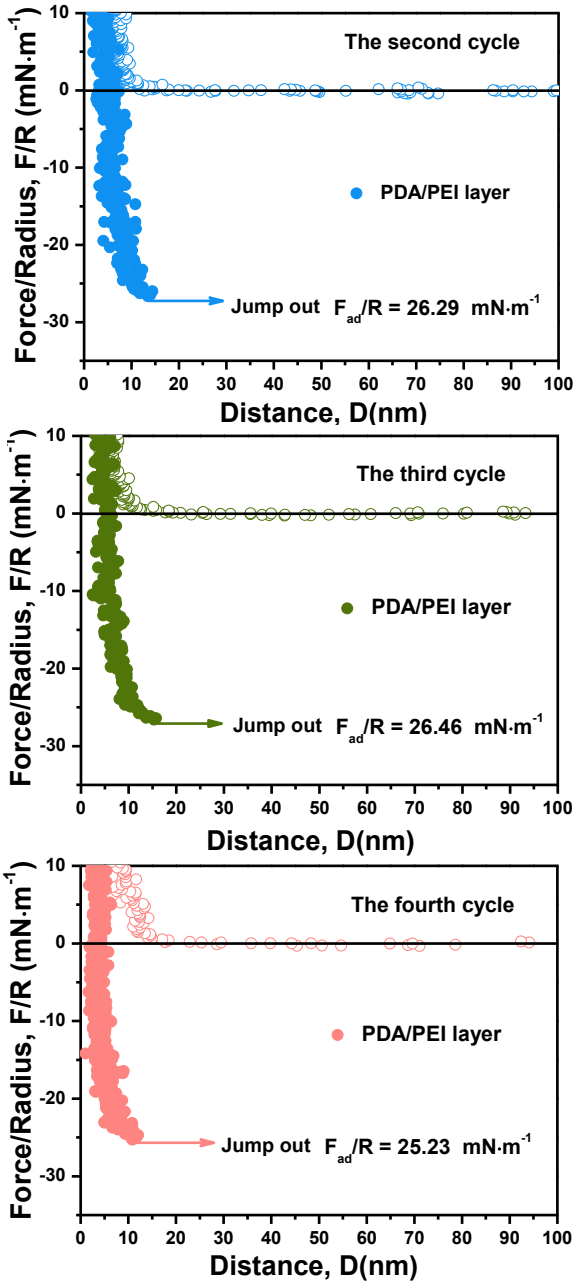

Figure S3.7 Force-distance curves of PDA layers and PDA/PEI (Mw = 800 g/mol) layers on mica after in situ polymerization at pH 8.5 and 250 mM KCl obtained at the same interaction position under sequential force measurements. The concentrations of dopamine and PEI are 2 mg/mL and 1 mg/mL, respectively.

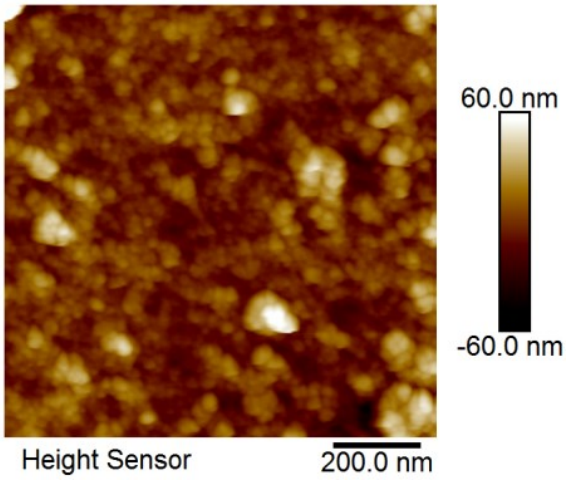

Figure S3.8 AFM images of PDA/PEI (Mw = 800 g/mol) coatings on mica deposited under tris buffer solution (pH 8.5) containing 600 mM KCl for 4 h. The concentration of dopamine and PEI is 2 mg/mL and 1 mg/L, respectively.

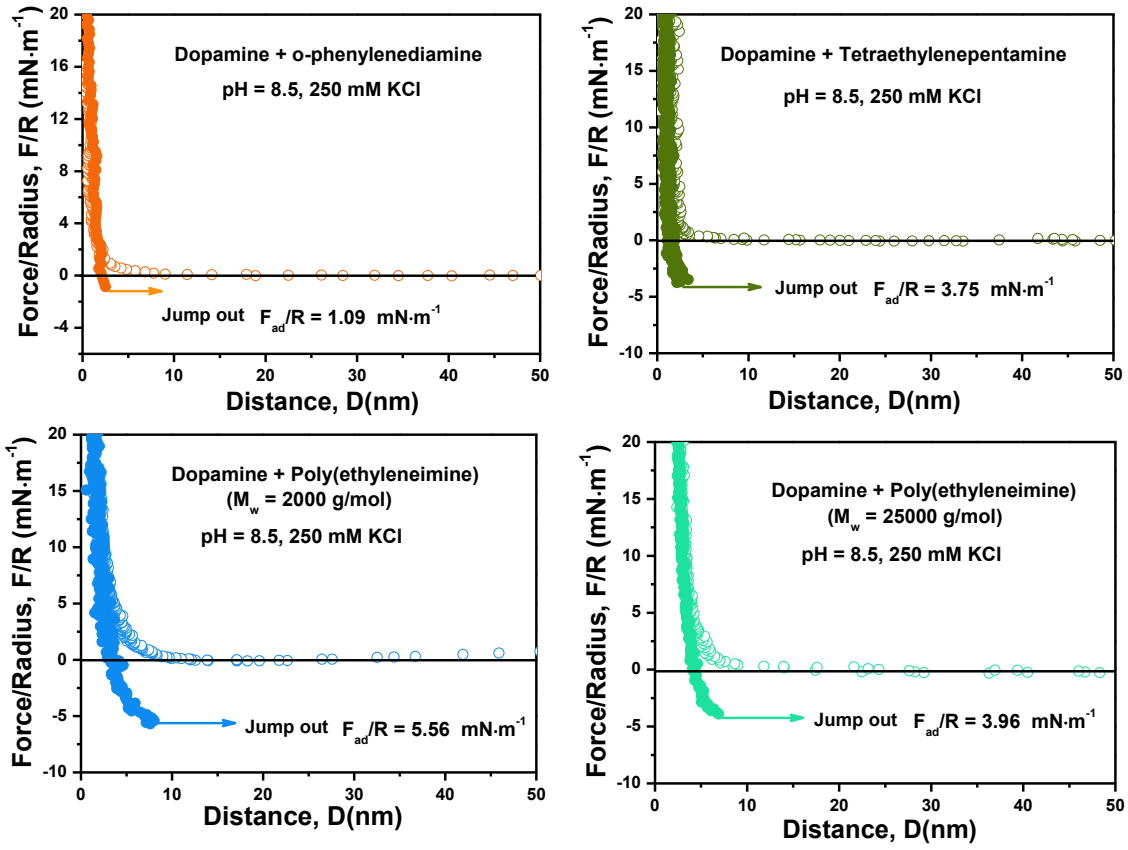

Figure S3.9 Force-distance curves of PDA/amines layers on mica after in situ

polymerization at pH 8.5 and 250 mM KCl. The concentrations of dopamine and amine are 2 mg/mL and 1 mg/mL, respectively.

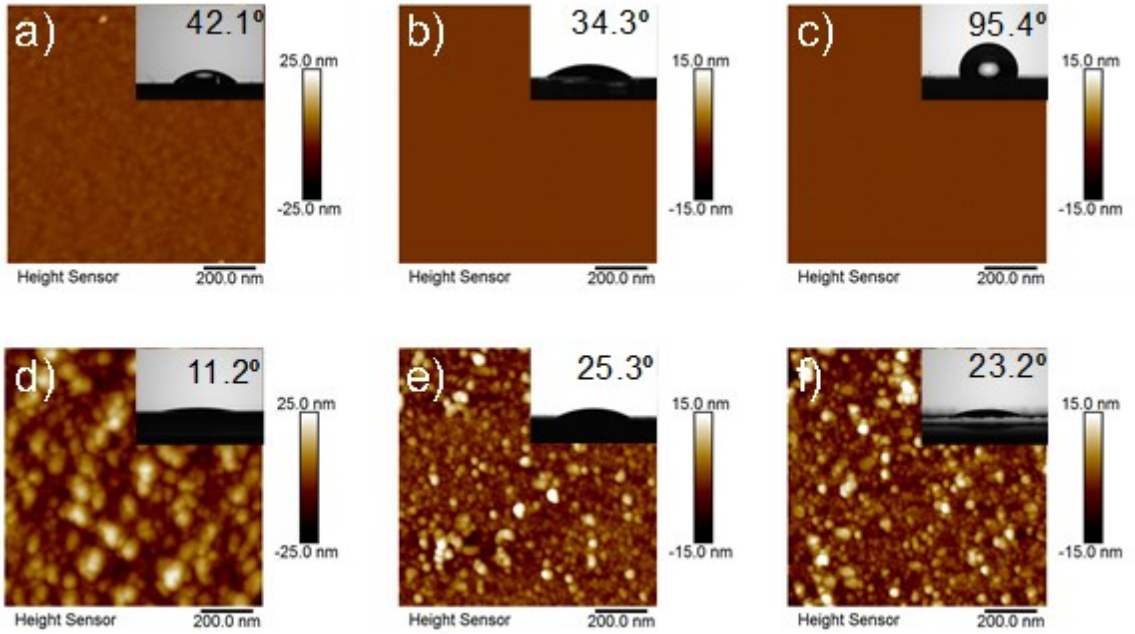

Figure S3.10 Topographic AFM images and water contact angles before and after 4-h deposition for: (a, d) gold surface, (b,e) (3-Aminopropyl)triethoxysilane (APTES) surface, and (c, f) trichloro(octadecyl)silane (OTS) surface. The deposition conditions are as follows: Tris buffer solution (pH = 8.5) containing 250 mM KCl. The concentrations of dopamine and PEI are 2 mg/mL and 1 mg/mL, respectively.

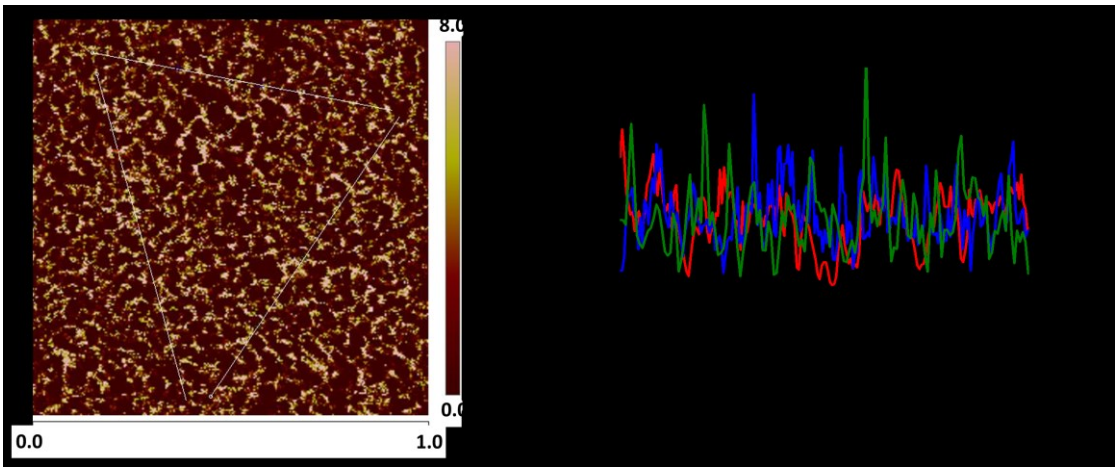

Figure S3.11 Typical DMT modulus calculation of PDA/PEI coatings using peak force quantitative nanomechanical (PF-QNM) method.

References

(1) Faure, E.; Falentin-Daudré, C.; Jérôme, C.; Lyskawa, J.; Fournier, D.; Woisel, P.; Detrembleur, C. *Prog. Polym. Sci.* **2013**, *38*, 236-270.

(2) Kord Forooshani, P.; Lee, B. P. *J Polym. Sci. A Polym. Chem.* **2017**, *55*, 9-33.

(3) Li, J.; Celiz, A.; Yang, J.; Yang, Q.; Wamala, I.; Whyte, W.; Seo, B.; Vasilyev, N.; Vlassak, J.; Suo, Z. *Science* **2017**, *357*, 378-381.

(4) Tay, F. R.; Pashley, D. H. *Am. J. Dent.* **2003**, *16*, 6-12.

(5) Lee, L.-H. In *Book*; Springer, 1988; pp 5-29.

(6) Waite, J. H. *Int. J. Adhes. Adhes.* **1987**, *7*, 9-14.

(7) Lee, H.; Dellatore, S. M.; Miller, W. M.; Messersmith, P. B. *science* **2007**, *318*, 426-430.

(8) Zhang, C.; Li, H.-N.; Du, Y.; Ma, M.-Q.; Xu, Z.-K. *Langmuir* **2017**, *33*, 1210-1216.

(9) Zhang, C.; Ou, Y.; Lei, W. X.; Wan, L. S.; Ji, J.; Xu, Z. K. *Angew. Chem., Int. Ed.* **2016**, *55*, 3054-3057.

(10) Guo, Z.; Zhou, F.; Hao, J.; Liu, W. *J. Am. Chem. Soc.* **2005**, *127*, 15670-15671.

(11) Schmidt, T. A.; Gastelum, N. S.; Nguyen, Q. T.; Schumacher, B. L.; Sah, R. L. *Arthritis & Rheumatism* **2007**, *56*, 882-891.

(12) Wei, Q.; Zhang, F.; Li, J.; Li, B.; Zhao, C. *Poly. Chem.* **2010**, *1*, 1430-1433.

(13) Hwang, D. S.; Sim, S. B.; Cha, H. J. *Biomaterials* **2007**, *28*, 4039-4046.

(14) Maier, G. P.; Rapp, M. V.; Waite, J. H.; Israelachvili, J. N.; Butler, A. *Science* **2015**, *349*, 628-632.

(15) Rapp, M. V.; Maier, G. P.; Dobbs, H. A.; Higdon, N. J.; Waite, J. H.; Butler, A.; Israelachvili, J. N. *J. Am. Chem. Soc.* **2016**, *138*, 9013-9016.

(16) Ahn, B. K. *J. Am. Chem. Soc.* **2017**, *139*, 10166-10171.

(17) Lee, B. P.; Messersmith, P. B.; Israelachvili, J. N.; Waite, J. H. *Annu. Rev. Mater. Res.* **2011**, *41*, 99-132.

(18) Lin, Q.; Gourdon, D.; Sun, C.; Holten-Andersen, N.; Anderson, T. H.; Waite, J. H.; Israelachvili, J. N. *Proc. Natl. Acad. Sci. U.S.A.* **2007**, *104*, 3782-3786.

(19) Waite, J. H.; Qin, X. *Biochemistry* **2001**, *40*, 2887-2893.

(20) Han, L.; Gong, L.; Chen, J.; Zhang, J.; Xiang, L.; Zhang, L.; Wang, Q.; Yan, B.; Zeng, H. *ACS Appl. Mater. Interfaces* **2018**, *10*, 2166-2173.

(21) Li, Y.; Wang, T.; Xia, L.; Wang, L.; Qin, M.; Li, Y.; Wang, W.; Cao, Y. *J. Mater. Chem. B* **2017**, *5*, 4416-4420.

(22) Sen, R.; Gahtory, D.; Carvalho, R. R.; Albada, B.; van Delft, F. L.; Zuilhof, H. *Angew. Chem. Int. Ed.* **2017**, *129*, 4194-4198.

(23) Yu, J.; Wei, W.; Danner, E.; Israelachvili, J. N.; Waite, J. H. *Adv. Mater.* **2011**, *23*, 2362-2366.

(24) Liu, M.; Zeng, G.; Wang, K.; Wan, Q.; Tao, L.; Zhang, X.; Wei, Y. *Nanoscale* **2016**, *8*, 16819-16840.

(25) Zhang, X.; Huang, Q.; Deng, F.; Huang, H.; Wan, Q.; Liu, M.; Wei, Y. *Applied Materials Today* **2017**, *7*, 222-238.

(26) Zhang, X.; Wang, S.; Xu, L.; Feng, L.; Ji, Y.; Tao, L.; Li, S.; Wei, Y. *Nanoscale* **2012**, *4*, 5581-5584.

(27) Lim, C.; Huang, J.; Kim, S.; Lee, H.; Zeng, H.; Hwang, D. S. *Angew. Chem. Int. Ed.* **2016**, *55*, 3342-3346.

(28) Israelachvili, J.; Min, Y.; Akbulut, M.; Alig, A.; Carver, G.; Greene, W.; Kristiansen, K.; Meyer, E.; Pesika, N.; Rosenberg, K. *Rep. Prog. Phys.* **2010**, *73*, 036601.

(29) Li, L.; Yan, B.; Zhang, L.; Tian, Y.; Zeng, H. *Chem. Comm.* **2015**, *51*, 15780-15783.

(30) Zeng, H.; Hwang, D. S.; Israelachvili, J. N.; Waite, J. H. *Proc. Natl. Acad. Sci.* **2010**, *107*, 12850-12853.

(31) Lu, Q.; Oh, D. X.; Lee, Y.; Jho, Y.; Hwang, D. S.; Zeng, H. *Angew. Chem.,* **2013**, *125*, 4036-4040.

(32) Israelachvili, J. N.; Academic press, 2011.

(33) Johnson, K. L.; Kendall, K.; Roberts, A. *Proc. R. Soc. A* **1971**, *324*, 301-313.

(34) Zeng, H.; Tian, Y.; Zhao, B.; Tirrell, M.; Israelachvili, J. *Macromolecules* **2007**, *40*, 8409-8422.

(35) Yang, H.-C.; Liao, K.-J.; Huang, H.; Wu, Q.-Y.; Wan, L.-S.; Xu, Z.-K. *J. Mater. Chem. A* **2014**, *2*, 10225-10230.

(36) Jin, L.; Liu, J.; Tang, Y.; Cao, L.; Zhang, T.; Yuan, Q.; Wang, Y.; Zhang, H. *ACS*

Appl. Mater. Interfaces **2017**, *9*, 41648-41658.

(37) Zhang, C.; Lv, Y.; Qiu, W.-Z.; He, A.; Xu, Z.-K. *ACS Appl. Mater. Interfaces* **2017**, *9*, 14437-14444.

(38) Hwang, D. S.; Harrington, M. J.; Lu, Q.; Masic, A.; Zeng, H.; Waite, J. H. *J. Mater. Chem.* **2012**, *22*, 15530-15533.

(39) Yu, J.; Wei, W.; Menyo, M. S.; Masic, A.; Waite, J. H.; Israelachvili, J. N. *Biomacromolecules* **2013**, *14*, 1072-1077.

(40) Liu, M.; Ji, J.; Zhang, X.; Zhang, X.; Yang, B.; Deng, F.; Li, Z.; Wang, K.; Yang, Y.; Wei, Y *J. Mater. Chem. B* **2015**, *3*, 3476-3482.

(41) Zhang, X.; Huang, Q.; Liu, M.; Tian, J.; Zeng, G.; Li, Z.; Wang, K.; Zhang, Q.; Wan, Q.; Deng, F. *Appl. Surf. Sci.* **2015**, *343*, 19-27.

(42) Hwang, D. S.; Zeng, H.; Lu, Q.; Israelachvili, J.; Waite, J. H. *Soft Matter* **2012**, *8*, 5640-5648.

(43) Kim, S.; Faghihnejad, A.; Lee, Y.; Jho, Y.; Zeng, H.; Hwang, D. S. *J. Mater. Chem. B* **2015**, *3*, 738-743.

(44) Kim, S.; Huang, J.; Lee, Y.; Dutta, S.; Yoo, H. Y.; Jung, Y. M.; Jho, Y.; Zeng, H.; Hwang, D. S. *Proc. Natl. Acad. Sci.* **2016**, *113*, E847-E853.

(45) Kim, S.; Yoo, H. Y.; Huang, J.; Lee, Y.; Park, S.; Park, Y.; Jin, S.; Jung, Y. M.; Zeng, H.; Hwang, D. S. *ACS nano* **2017**, *11*, 6764-6772.

(46) Shao, H.; Stewart, R. J. *Adv. Mater.* **2010**, *22*, 729-733.

(47) Haemers, S.; Koper, G. J.; Frens, G. *Biomacromolecules* **2003**, *4*, 632-640.

(48) Zhao, Q.; Lee, D. W.; Ahn, B. K.; Seo, S.; Kaufman, Y.; Israelachvili, J. N.; Waite, J. H. *Nature materials* **2016**, *15*, 407.

(49) Lv, Y.; Yang, H.-C.; Liang, H.-Q.; Wan, L.-S.; Xu, Z.-K. *J. Membr. Sci.* **2015**, *476*, 50-58.

(50) Adamcik, J.; Lara, C.; Usov, I.; Jeong, J. S.; Ruggeri, F. S.; Dietler, G.; Lashuel, H. A.; Hamley, I. W.; Mezzenga, R. *Nanoscale* **2012**, *4*, 4426-4429.

(51) Oral, I.; Guzel, H.; Ahmetli, G. *Polymer bulletin* **2011**, *67*, 1893-1906.

(52) Lin, A. S.; Barrows, T. H.; Cartmell, S. H.; Guldberg, R. E. *Biomaterials* **2003**, *24*, 481-489.

Chapter 4. Probing the Interaction Forces of Phenol/amine Deposition in Wet Adhesion: Impact of Phenol/amine Mass Ratio and Surface Properties

4.1 Introduction

Mussel-inspired wet adhesion strategies to functionalize material surfaces have attracted great attention and been widely applied in different areas including wound dressing,[1] dental restoration,[2] biosensor,[3] bone tissue engineering[4] and under seawater pipeline repair.[5] In general, dopamine, a catecholamine compound that mimics mussel foot proteins (Mfps)[6], can readily self-polymerize in weak alkaline solutions to form polydopamine (PDA) coatings on virtually all kinds of material surfaces.[7-9] Although PDA modification has exhibited great success in modulating the surface properties of a wide range of materials, it still suffers from some deficiencies, including relatively low stability, deep coloration of PDA coatings which are possibly impediment for its wide applications in some specific optical areas and high processing cost related to expensive DA monomer.[10-13] To address the aforementioned shortcomings of PDA coatings, a low-cost plant polyphenol named tannic acid (TA) has been exploited as a potential building block for functionalizing the surfaces of different materials due to its structure resemblance to DA.[14] The as-fabricated TA coatings demonstrate similar surface properties as PDA coatings but a dramatically decreased coloration. To further improve the performance of the TA coatings (e.g., coating thickness and stability), a novel phenol/amine coating strategy was developed by co-depositing with the cost-effective amine monomers such as diethylenetriamine (DETA) under mild alkaline conditions. This special coating strategy demonstrates great versatility

in modulating the surface properties, including light surface coloration, tunable surface roughness and hydrophobicity.[15-18] Besides, the relatively higher ratio of phenolic hydroxyl group compared to DA enable stronger adhesion of TA to substrate, which thereby leads to a enhanced coating stability.[17]

Generally, the phenol/amine coating deposition process is believed to be dominated by both the chemical reactions between phenols and amines and the physical interactions of the as-formed phenol/amine moieties.[16] The chemical reaction has been widely recognized to induce the formation of small phenol/amine moieties through Michael addition or Schiff base reaction between amines and phenol groups.[19, 20] The physical interactions including hydrogen bonding,[21] coordination interaction,[22] electrostatic interaction,[23, 24] cation-π interaction,[25, 26] π-π stacking,[27] and hydrophobic interaction[28] would not only induce the assembly of these moieties to phenol/amine aggregates but also drive the as-formed aggregates to adhere to the substrate surfaces and facilitate the growth of phenol/amine coatings. Nevertheless, the dominant interactions for promoting the deposition are largely dependent on the phenol/amine mass ratio in the solution for deposition and the surface properties of substrates (e.g., chemical composition and wettability), leading to the distinct deposition behavior of phenol/amine.[29] Therefore, a systematically investigation of the interaction forces between phenol/amine coatings and between phenol/amine coating and substrate surfaces is of both fundamental and practical importance to elucidate phenol/amine deposition mechanism.

Our previous work has demonstrated the success and feasibility of using surface forces apparatus (SFA) and atomic force spectroscopy (AFM) in studying the nanomechanics

underlying the PDA coatings.[27,30,31] Thus, both SFA and AFM can be employed as useful tools to quantify the specific interactions involved in the phenol/amine deposition process. In this work, using TA and DETA as typical phenol and amine components, the impact of phenol/amine mass ratio on the interaction forces between phenol/amine coatings and the deposition capacity of phenol/amine was investigated using SFA and AFM. Furthermore, the deposition capability and adhesion behavior of phenol/amine coating to different substrates were also evaluated. By systematically correlating the phenol/amine deposition behavior and interaction mechanism of phenol/amine moieties and between phenol/amine and various substrate surfaces, the nanomechanics behind this deposition strategy was unraveled. Our results provide useful insight on the fundamental understanding of interaction mechanism involved in phenol/amine deposition, with implications for the design and development of novel phenol/amine-based coating strategy for a wide range of engineering and bioengineering applications.

4.2 Materials and Experimental Methods

Materials. TA, DETA, (3-Aminopropyl) triethoxysilane (APTES) (≥ 99.9%) and polystyrene (PS) with the molecular weight of 8000 (PDI ≤ 1.05) were purchased from Sigma-Aldrich (Canada). Tris(hydroxymethyl)aminomethane and toluene (HPLC grade) were obtained from Fisher Scientific (Canada). Octadecyltrichlorosilane (OTS) was purchased from ACROS Organics. All chemical reagents were used without further purification. The water used in all experiments was Milli-Q water with the resistivity of 18.2 MΩ·cm.

Modification of mica surfaces. Titanium dioxide (TiO_2) thin film deposited on mica surface was prepared using an electron beam evaporation system (Gomez).[116] OTS-

modified and APTES-modified mica surfaces were achieved through a vapor-deposition method by exposing the mica to OTS and APTES vapor in a sealed desiccator for 24 h and 3 h, respectively.[33] PS thin film on mica surface was obtained by spin-coating PS-toluene solution on the mica substrate followed by drying under vacuum overnight (>12 h) to remove toluene.[34]

Fabrication of TA/DETA coatings. TA and DETA were selected as the model phenol and amine in our work. To prepare TA/DETA solution for deposition, TA and DETA were dissolved in tris buffer solution (pH=8.5, 10 mM) with different mass ratios of 1:0, 1:1, 1:2, 1:5, 1:10, 1:15, 1:20 and 1:50. The concentration of TA was fixed to be 2 mg/mL. TA/DETA coatings on mica surfaces were prepared using dip coating method. Freshly cleave mica was placed in 20 mL newly prepared TA/DETA tris buffer solution for 2 h. Then, the as-deposited mica surfaces were thoroughly rinsed by deionized water and dried by nitrogen gas before use. The same protocol was also applied to deposit TA/DETA coatings on other modified mica substrates.

Characterization. The surface morphologies before and after TA/DETA coatings were characterized using AFM (Bruker, Santa Barbara, CA), and the chemical components of the as-formed TA/DETA coatings were determined by X-ray photoelectron spectroscopy (XPS) (Kratos AXIS 165). The surface hydrophobicity before and after TA/DETA coatings was evaluate by a contact angle goniometer (ramé-hart instrument, Succasunna, NJ). The thickness of TA/DETA coating on different substrates was measured by a spectroscopic ellipsometer (Sopra GESP-5, France).

Surface force measurement by SFA.

The interaction forces (namely cohesion force and adhesion force) between TA/DETA

coatings and between TA/DETA coating and the substrate surfaces with different functional groups were measured using an SFA according to our reported procedure.[35, 36] To measure the cohesion force between two TA/DETA coatings, TA/DETA coatings were deposited to two thin back-silvered (with ~50 nm Ag) mica sheets (thickness 1-5 μm) on cylindrical silica disks (radius R = 2 cm). These two as-prepared TA/DETA surfaces were then mounted into the SFA chamber in a crossed-cylinder geometry, which denoted as a symmetric configuration (**Scheme 4.1a**), and the interaction of which is locally equivalent to a sphere of radius R against a flat surface when their separation $D \ll R$ based on the "Derjaguin approximation".[37] Then, tris buffer solution was injected between two surfaces and the system was allowed to equilibrate for 30 min. The normal forces F between TA/DETA coatings were measured as a function of surface separation D with the distance accuracy down to 0.1 nm. The absolute surface separation can be obtained in real time and in situ by employing the fringes of equal chromatic order (FECO) on the basis of an optical technique multiple beam interferometry (MBI).[38] The reference distance (D = 0) was defined as the contact of two bare mica surfaces in air before TA/DETA coating deposition. Thus, the coating thickness could be determined via the shift of the FECO wavelength before and after coating. F was determined according to the Hooke's law. During a typical force measurement, two surfaces were first brought to approach each other ("in") to come into contact, and then were kept in contact for a certain time followed by separation ("out"). Cohesion would be measured when the two surfaces were driven to separate and jumped apart from each other (so-called "jump out"). The cohesion force F_{co} measured during separation could be correlated to the cohesion energy per unit area W_{co} based on the Johnson−Kendall−Roberts (JKR) model: $W_{co}=F_{co}/1.5\pi R$, which is generally for soft

deformable surfaces with relatively strong adhesive contact.[39, 40] To determine the adhesion force between TA/DETA coating and the modified mica substrates, TA/DETA coating was first prepared by immersing mica surface in tris buffer solution with the optimal TA/DETA mass ratio of 1:10 for 30 min. After that, one TA/EDTA coated surface and one mica substrate with a specific functional group were mounted into the SFA chamber in a crossed-cylinder geometry, respectively, which denoted as an asymmetric configuration (**Scheme 4.1b**). Then, the force was measured for the symmetric configuration. The adhesion could be measured when the two surfaces at adhesive contact was separated and jumped away from each other. The adhesion energy per unit area W_{ad} could also be calculated from the measured adhesion force F_{ad} according to the JKR mode. Each measurement was repeated at least three times independently under a fixed experimental condition.

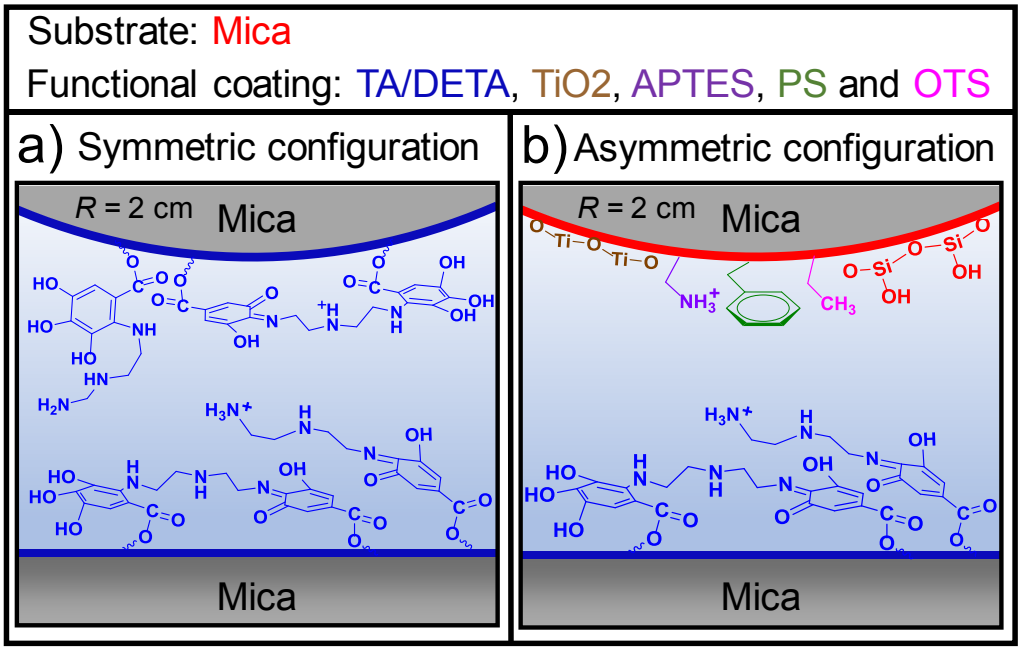

Scheme 4.1 Schematic of the interacting surfaces in a) symmetric configuration and b) asymmetric configuration under aqueous condition (10 mM tris buffer, pH 8.5) during surface force measurements using a surface forces apparatus (SFA).

4.3 Results and Discussion

Impact of phenol/amine mass ratio on the surface interaction and deposition

Figure 4.1 shows typical force - distance profiles of interaction between two as-prepared TA/DETA coatings in tris buffer solution (pH 8.5, 10 mM). For these force measurements, TA/EDTA coatings with different components were prepared by dip-coating mica surfaces in tris buffer solutions of TA/EDTA with different mass ratios. In all the cases, pure repulsion was detected during approach. While during separation, a "jump out" behavior was observed, indicating cohesion between two surfaces. For the case of TA coating (*i.e.,* the mass ratio of TA and DETA kept as 1:0), as shown in **Figure 4.1a**, the normalized cohesion force F_{co}/R was ~2.71 mN/m (W_{co} ~0.57 mJ/m^2) with the thickness of TA coating of ~1.6 nm. The coating thickness is very close to the hydrodynamic diameter of TA molecules, implying a monolayer of the TA moieties deposited on the surface.[41] The limited deposition capability is mostly due to the strong electrostatic repulsion between negatively charged TA molecules at pH 8.5,[42] preventing them from assembling to TA nanoaggregates and further depositing to the substrate. However, when DETA was introduced into the deposition system, both the cohesion strength between TA/DETA coatings and thickness of TA/DETA coating were found to greatly increase, which exhibit a great dependence on the TA/DETA mass ratio (**Figure 4.1b – h)**. As TA/DETA mass ratio increases from 1:1 to 1:50, the resulting TA/DETA coatings exhibit the maximum cohesion strength and coating thickness at 1:10. The effect of TA/DETA mass ratio on the cohesion strength and coating thickness is summarized in **Figure 4.2**. The consistency of the variation of cohesion strength and coating thickness indicates that the stronger cohesion between TA/DETA coatings could facilitate the deposition of TA and DETA and form thicker coatings on

substrate surface. To better understand the SFA results, the chemical compositions of bare mica and TA/ DETA coatings (the TA/DETA mass ratio of 1:10) were analyzed by XPS (**Figure 4.3)**. The high-resolution spectra of N_{1s} suggest formation of C-N and C=N bonds between TA and DETA during the deposition process. Besides, the solution behavior of the TA/DETA mixtures highly depends on the TA/DETA mass ratio. When the mass ratio sets between 1:1 and 5:1, the mixtures become turbid with discernable white precipitates (**Figure S4.1**). However, further increasing the ratio of DETA in TA/DETA mixtures could gradually transfer the heterogeneous suspension into the transparent solutions by effectively suppressing the precipitation of the aggregates. We attribute the above solution and deposition behaviors of TA/DETA mixtures to the physical and chemical interactions between TA and DETA during deposition. It is well-known that DETA molecules are positively charged at pH 8.5 due to the protonation of amino groups.[43] Hence, negatively-charged TA molecules would be first attracted by DETA molecules via the electrostatic attraction and then form TA/DETA moieties through Schiff base reaction or Michael addition of the amino groups on DETA molecules and phenol groups on TA molecules.[17] The resulting TA/DETA moieties will self-assemble into aggregates of different size as a function of the TA/DETA mass ratio. When the ratio of DETA is relatively low (e.g., the TA/DETA mass ratios of 1:1 and 1:2), the DETA molecules mainly serve as crosslinkers to react with TA molecules to form TA/DETA moieties. In addition, introducing positively charged DETA molecules could neutralize the negative-charged TA molecules and thus weaken the electrostatic repulsion between TA/DETA moieties. In this case, attractive interactions such as hydrogen bonding, π - π stacking, cation - π interaction and hydrophobic interaction would overwhelm and result in the severe aggregation of these

moieties. The resulting TA/DETA aggregates will be of larger size and prefer to precipitate from the solution instead of depositing on the surfaces.[44] Therefore, very limited thickness of TA/DETA coatings of 2.7 nm and 2.9 nm are achieved with weak cohesion with $F_{co}/R \sim$ 4.64 mN/m ($W_{co} \sim 0.97$ mJ/m^2) and $F_{co}/R \sim 6.49$ mN/m ($W_{co} \sim 1.36$ mJ/m^2) for the cases of 1:1 and 1:2 (**Figure 4.1b** and **c)**. However, adjusting the TA/DETA mass ratio to 1:5 and 1:10, more positively charged DETA molecules would interact/react with TA molecules and form the TA/DETA moieties with excessive positive charge.[45] The electrostatic repulsion between TA/DETA moieties would compete with other attractive interactions to slow down their aggregation and suppress the precipitation. As such, more stable TA/DETA aggregates with desired size will be formed and steadily exist in the solution for deposition. Therefore, as shown in **Figure 4.1d - f**, the resultant TA/DETA coatings possess dramatically increased thickness of ~ 7.3 nm, ~ 10.1 nm and ~ 6.3 nm at the cases of 1:5, 1:10 and 1:15, respectively, and the stronger cohesion between the corresponding TA/DETA coatings has been measured with $F_{co}/R \sim 17.29$ mN/m ($W_{co} \sim 3.63$ mJ/m^2), $F_{co}/R \sim 20.86$ mN/m ($W_{co} \sim 4.38$ mJ/m^2) and $F_{co}/R \sim 18.58$ mN/m ($W_{co} \sim 3.9$ mJ/m^2), respectively. The strongest cohesion was measured at the case of 1:10, suggesting that the adhesion between TA/DETA coating and mica surface is larger than 20.86 mN/m.[112] Nevertheless, further increasing the TA/DETA mass ratio to 1:20 and 1:50 can only decreases the thickness of TA/DETA coatings and the cohesion between TA/DETA coatings. We attribute this to formation of highly positively charged TA/DETA moieties at high ratios of DETA. As the strong electrostatic repulsion between TA/DETA moieties becomes dominant, the growth of TA/DETA aggregates will be mostly suppressed and greatly enhance their stabilization in the aqueous solution. Therefore, less TA/DETA aggregates could be formed

for deposition on the substrate surfaces, with the coating thickness and cohesion strength decreased to ~ 5.9 nm and ~ 5.2 nm, and F_{co}/R ~ 14.33 mN/m (W_{co} ~ 3.01 mJ/m^2) and F_{co}/R ~ 8.82 mN/m (W_{co} ~ 1.85 mJ/m^2) at the cases of 1:20 and 1:50 (**Figure 4.1g** and **h**).

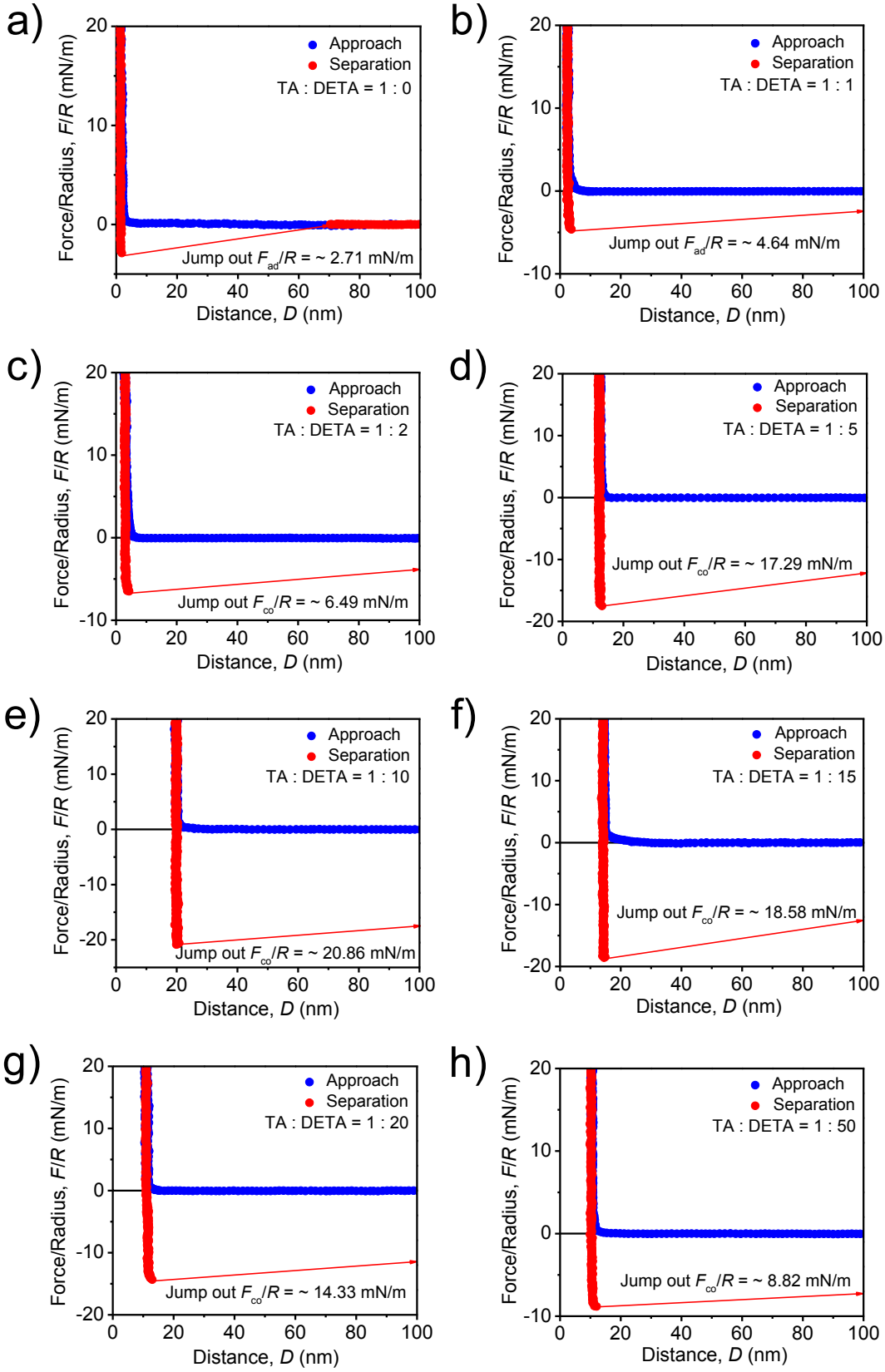
a)
Approach
Separation
TA : DETA = 1 : 0
Jump out F_{ad}/R = ~ 2.71 mN/m
b)
Approach
Separation
TA : DETA = 1 : 1
Jump out F_{ad}/R = ~ 4.64 mN/m
c)
Approach
Separation
TA : DETA = 1 : 2
Jump out F_{co}/R = ~ 6.49 mN/m
d)
Approach
Separation
TA : DETA = 1 : 5
Jump out F_{co}/R = ~ 17.29 mN/m
e)
Approach
Separation
TA : DETA = 1 : 10
Jump out F_{co}/R = ~ 20.86 mN/m
f)
Approach
Separation
TA : DETA = 1 : 15
Jump out F_{co}/R = ~ 18.58 mN/m
g)
Approach
Separation
TA : DETA = 1 : 20
Jump out F_{co}/R = ~ 14.33 mN/m
h)
Approach
Separation
TA : DETA = 1 : 50
Jump out F_{co}/R = ~ 8.82 mN/m
Force/Radius, F/R (mN/m)
Distance, D (nm)

Figure 4.1 Force-distance profiles of the interaction between two as-formed TA/DETA coatings on mica under tris buffer condition (10 mM, pH 8.5). TA/DETA coatings were prepared using Tris buffer solutions containing TA and DETA with different mass ratios a) 1:0, b) 1:1, c) 1:2, d) 1:5, e) 1:10, f) 1:15, g) 1:20 and h) 1:50. The concentration of TA is kept as 2 mg/mL. The deposition time is 2 h.

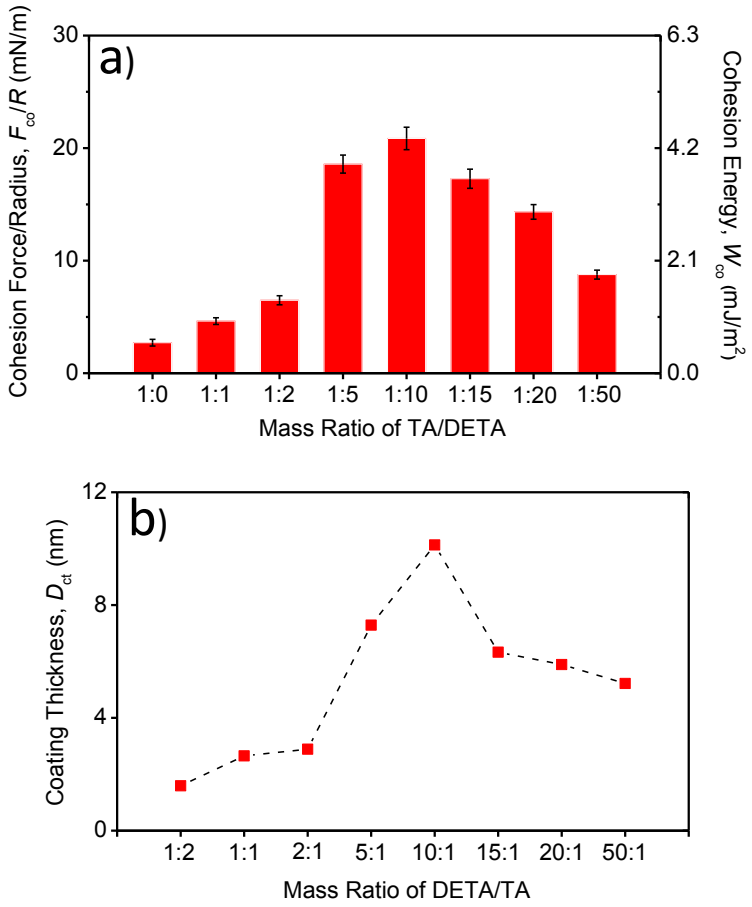

Figure 4.2 The effects of the TA/DETA mass ratio on a) the normalized cohesion forces F_{co}/R and cohesion energy (W_{co}) between TA/DETA coatings, and b) thickness of the TA/DETA coating.

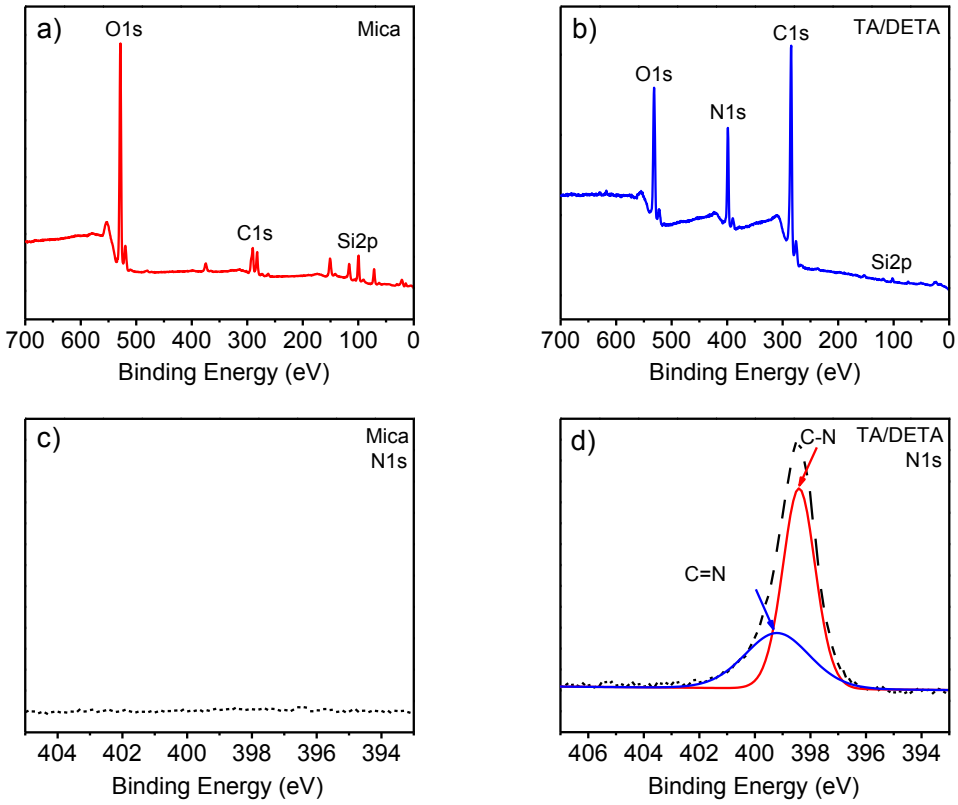

Figure 4.3 X-ray photoelectron spectroscopy (XPS) characterization of a) pristine mica and b) TA/EDTA coating on mica surface. High-resolution XPS analysis of N1s on c) pristine mica and d) the TA/DETA coating.

To obtain further insight into the deposition behavior of TA/DETA moieties, the effect of TA/DETA mass ratio on the surface morphologies of TA/DETA coatings were investigated using AFM. The topographic AFM image of bare mica surface was flat with root-mean-square (RMS) roughness of ~ 0.2 nm (**Figure S4.2**). After TA/DETA deposition, variation in surface morphology of mica could be observed in the height AFM images (**Figure 4.4**). At low TA/DETA mass ratio of 1:0, 1:1 and 1:2, **Figure 4.4a - c** display very few TA or TA/DETA aggregates adsorbed on the surface, indicated by the slightly increased surface roughness of ~0.24 nm, ~0.26 nm and ~0.33 nm, respectively. Here, the limited deposition

capabilities of TA and TA/DETA at low mass ratios arise from different reasons. For the case of TA, the low deposition capacity is mainly due to the strong electrostatic repulsion between negatively charged TA molecules, which strongly inhibits the formation of TA aggregates from surface deposition; while for the case of TA/DETA mass ratios of 1:1 and 1:2, the introduced DETA greatly accelerates the aggregation of TA via bridging effect and thus forms large TA/DETA aggregates to precipitate from the solution rather than deposit on the surface. With the TA/DETA mass ratio changing to 1:5, 1:10 and 1:15, the AFM topographic images in **Figure 4.4d** and **f** show that the resulting TA/DETA coatings are closely packed by TA/DETA aggregates with the higher surface roughness of ~ 1.69 nm, ~ 1.87 nm and ~ 1.38 nm, respectively. The compact morphology of TA/DETA coatings is most likely due to that the aggregation of TA/DETA could be well controlled by adding more DETA molecules, generating sufficient amount of stable TA/DETA aggregates of desirable size which would be favorable to deposit on the substrate rather than precipitate from the solution. However, continuously increasing the TA/DETA mass ratio to 1:20 and 1:50 would result in less compact TA/DETA coatings with loosely packed TA/DETA aggregates on surface (**Figure 4.4g** and **h**), as introducing excessive DETA requires prolonged time to form stable TA/DETA aggregates with suitable size for deposition from strongly charged TA/DETA moieties. The less compact TA/DETA coating also leads to a relatively higher surface roughness of ~ 2.23 nm and ~ 2.26 nm for the case of 1:20 and 1:50, respectively. By correlating the variance of surface morphology, thickness and cohesion strength of TA/DETA coatings, it is reasonable to conclude that DETA plays several roles in preparing TA/DETA coatings: 1) react with TA to form TA/DETA moieties via Michael addition or Schiff base reaction; and 2) influence the physical interactions (e.g.,

electrostatic interaction) between TA/DETA moieties to mediate the formation of TA/DETA aggregates with desirable size for steady deposition, which thereby modulate the deposition behavior (e.g., coating thickness and surface roughness) of TA/DETA coatings.

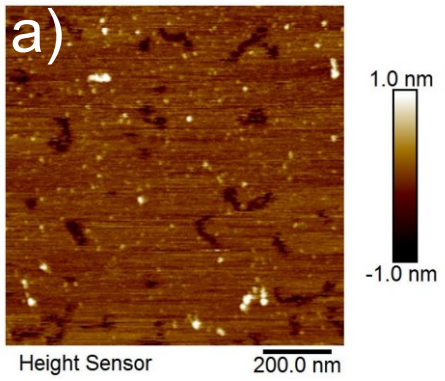
a)
1.0 nm
-1.0 nm
Height Sensor
200.0 nm

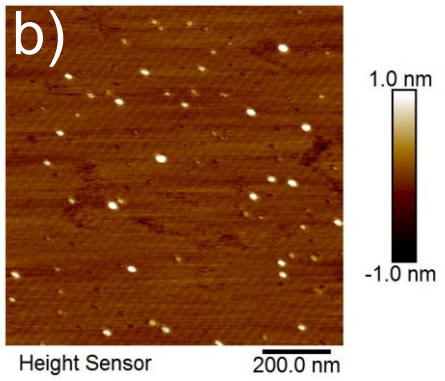
b)
1.0 nm
-1.0 nm
Height Sensor
200.0 nm

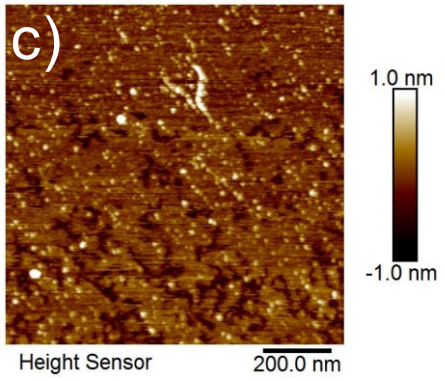
c)
1.0 nm
-1.0 nm
Height Sensor
200.0 nm

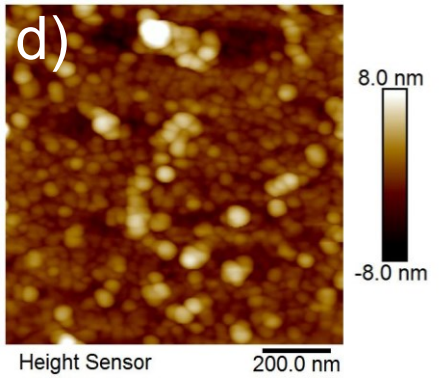
d)
8.0 nm
-8.0 nm
Height Sensor
200.0 nm

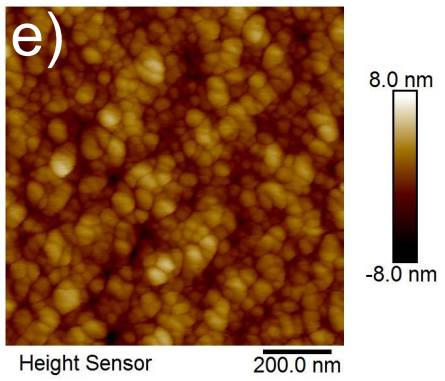
e)
8.0 nm
-8.0 nm
Height Sensor
200.0 nm

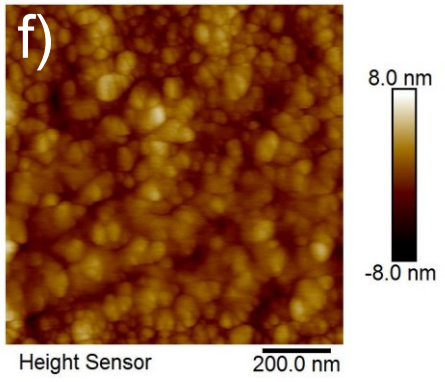
f)
8.0 nm
-8.0 nm
Height Sensor
200.0 nm

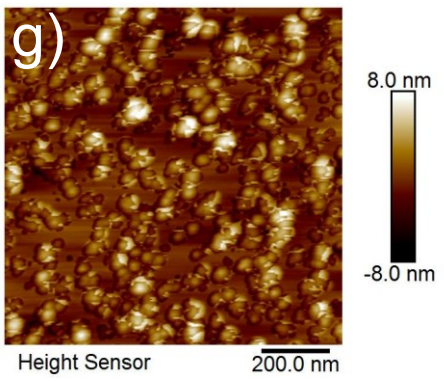
g)
8.0 nm
-8.0 nm
Height Sensor
200.0 nm

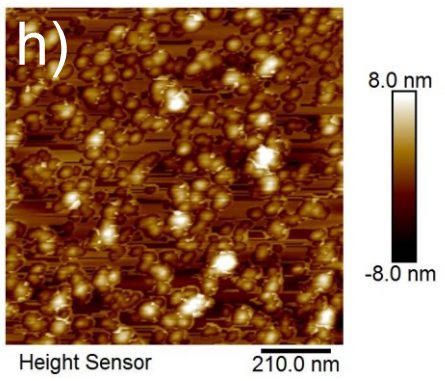
h)
8.0 nm
-8.0 nm
Height Sensor
210.0 nm

Figure 4.4 Atomic force microscopy (AFM) images of as-formed TA/DETA coatings on mica surfaces using tris buffer solutions containing different TA/DETA mass ratios: a) 1:0, b) 1:1, c) 1:2, d) 1:5, e) 1:10, f) 1:15, g) 1:20 and h) 1:50. The concentration of TA is 2 mg/mL and the deposition time is 2 h.

Impact of surface chemistry and wettability on the interaction forces and deposition

During the deposition process, the adhesion of phenol/amine aggregates to substrate surfaces is the first step to realize the deposition process. Although the successful formation of TA/DETA coating on mica surface implies the existence of strong adhesion between phenol/amine aggregates and the mica surface, for the substrate with different surface chemistry (i.e., different chemical compositions), the adhesion behavior may be different. To unravel the adhesion mechanism, SFA was utilized to investigate the interaction forces between TA/DETA coating and various substrates with different surface properties such as hydrophobicity and carrying different functional groups. The TA/DETA coating on the mica surface was prepared by the aforementioned procedure using TA/DETA mass ratio of 1:10. Topographic AFM image shows a full coverage of TA/DETA aggregates on the mica surface (**Figure S4.3**). The substrates with different surface properties were prepared by modifying the mica surface with different chemical agents according to the reported procedures with some modifications.[32-34] After modifying mica surfaces with APTES, TiO_2, PS and OTS, the WCA significantly increased from < 5° to ~ 58°, ~ 57.6°, ~ 93.5° and ~ 109°and the surface roughness increase from ~ 0.2 nm to ~ 0.42 nm, ~ 0.82 nm, ~ 0.65 nm and ~ 0.53 nm, respectively (**Figure S4.2** and 4.**5**). Such obvious change of surface hydrophobicity and morphology of bare mica surfaces demonstrate the successful modification of mica surfaces. **Figure 4.6** shows the force-distance profile of interaction

between TA/DETA coating and APTES surface, TiO_2 surface, PS surface, OTS surface, mica surface in 10 mM buffer solution at pH 8.5, respectively. Pure repulsion was measured during approach for all the cases. When the two surfaces were separated, an obvious "jump out" behavior was observed on the force curves, suggesting the adhesion between TA/DETA coating and these substrates. The F_{ad}/R and W_{ad} of TA/DETA coating to different substrates are summarized in Figure 6f, which follow an order of APTES surface < mica surface < OTS surface < TiO_2 surface < PS surface. The origin of the measured adhesion can be ascribed to the synergistic effect of various interactions such as electric double layer (EDL) forces, hydrogen bonding, van der Waals forces, hydrophobic interactions and so on. For different substrates with the distinct surface chemistry, the major interaction contributing to the strong adhesion to TA/DETA coating is different. At pH 8.5, the APTES surface is positively charged due to the protonation of amino groups and electrostatic interaction between APTES surface and TA/DETA coating is repulsive, while the TiO_2, PS, OTS and mica surfaces have been reported to be negatively charged,[33, 46-48] resulting in an attractive electrostatic interaction between these surfaces and TA/DETA coating. The EDL repulsion in the case of APTES surface may impede the formation of hydrogen bonds between the hydrogen bonding sites on the two surfaces to some extent,[49] leading a relatively weaker adhesion measured in SFA experiments compared to that of other surfaces. In addition to the contribution of EDL attraction, other interactions may also be involved in the measured adhesion for the other four cases. The strong adhesion for the case of TiO_2 surface could also be contributed from the chelating bonding between phenol groups on TA and the Ti sites on TiO_2 surface.[50] The electrostatic attraction between hydrophobic PS or OTS surface and TA/DETA coating could lead to the intimate contact

of the two surfaces. The intimate surface contact is beneficial for the enhancement of hydrophobic interactions between alkyl groups and/or aryl groups on TA/DETA surface and hydrophobic moieties on OTS and PS surface, inducing the strong adhesion measured during separation. Besides, in the case of PS surface, the cation–π interaction between amino groups on DETA and aryl groups on PS may also contribute to the enhanced adhesion when compared to that of OTS surface.[27] For mica surface, the hydrogen bonding between the hydrogen-binding sites on the TA/DETA coating and the oxygen atoms or hydroxyl groups on mica surface is believed to be the major contribution to the adhesion.[26] Compared to that of TiO_2, this finding associated with the weaker adhesion strength is consistent with the previous report, which could be ascribed to the fact that the strength of coordination bond is generally stronger than that of hydrogen bond.[21] The above results indicate that TA/DETA moieties possess the versatility of interacting with various surfaces through different types of interactions due to their specific molecular structure and chemical properties. Such adhesion behavior endows TA/DETA moieties with surface-independent adhesion properties, which hold the key to initiate the deposition of TA/DETA and realize the formation of TA/DETA coatings on different surfaces.

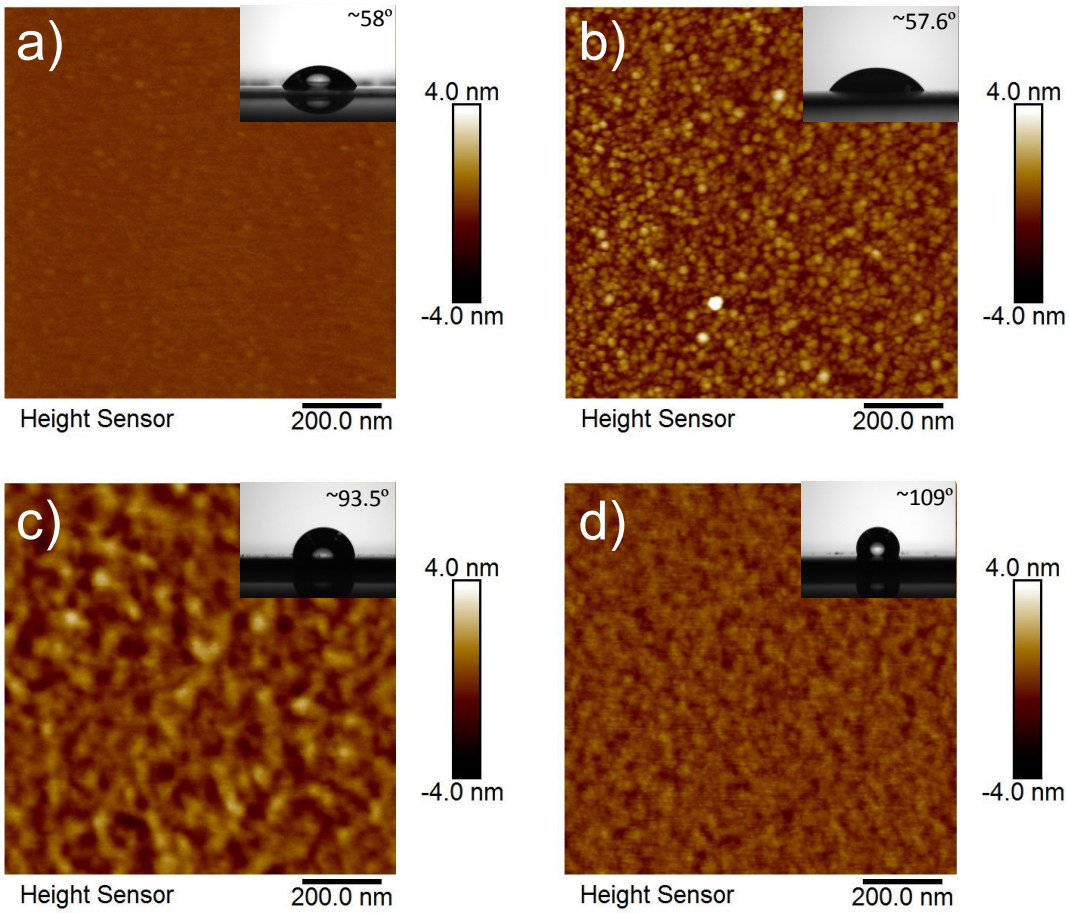

Figure 4.5 AFM images and WCA of a) (3-Aminopropyl) triethoxysilane (APTES), b) Titanium dioxide (TiO2), c) polystyrene (PS) and d) Octadecyltrichlorosilane (OTS) modified mica surface.

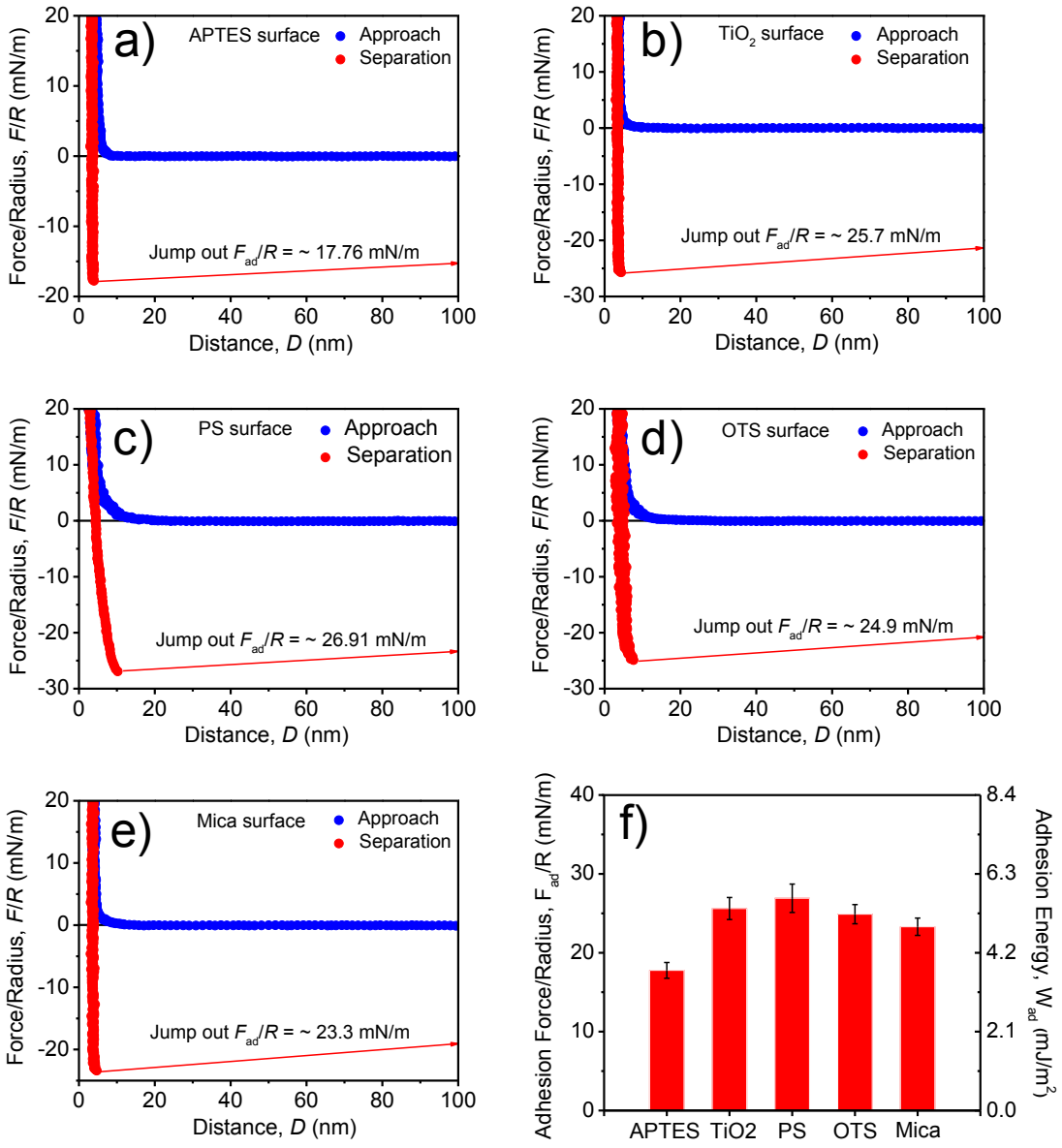

Figure 4.6 Force-distance profiles measured between the as-formed TA/DETA coating and different types of surfaces a) APTES surface, b) TiO2 surface, c) PS surface, d) OTS surface and e) Mica surface under tris buffer condition (10 mM, pH 8.5).

To evaluate the versatility of TA/DETA deposition, the TA/DETA coating strategy was utilized to modify the substrates with different surface properties. The surface wettability and morphology of different surfaces before and after TA/DETA deposition were characterized by contact angle goniometer and AFM. After the TA/DETA deposition, the

modified surfaces show a dramatically increased hydrophilicity with the WCA of ~ 20° (**Figure 4.7a - e**), indicating that TA/DETA coatings have been successfully formed on these substrates. Meanwhile, the AFM images in **Figure 4.7a - e** show distinct variations in surface morphology after TA/DETA coating. In contrast to the relatively lower surface roughness of all the surfaces before TA/DETA deposition, all the modified surfaces are fully covered with TA/DETA aggregates with the higher surface roughness between ~ 1.23 nm and ~ 2.35 nm. The corresponding coating thickness was determined to be ~ 8.5 nm, ~ 11.2 nm, ~ 12.6 nm, ~ 12.3 nm and ~ 10.1 nm, respectively. It is worth noting that the surface roughness and coating thickness in the case of APTES surface is smaller than that of the other four cases. This relatively lower deposition capability is most likely ascribed to the slightly weaker adhesion of APTES surface to TA/DETA coating measured in SFA experiments, suggesting that the adhesion strength of TA/DETA moieties to the substrate surfaces could significantly influence the coating growth during the deposition process. Therefore, the SFA, WCA and AFM results verify that TA/DETA deposition is a feasible and versatile strategy to modify a wide variety of surfaces.

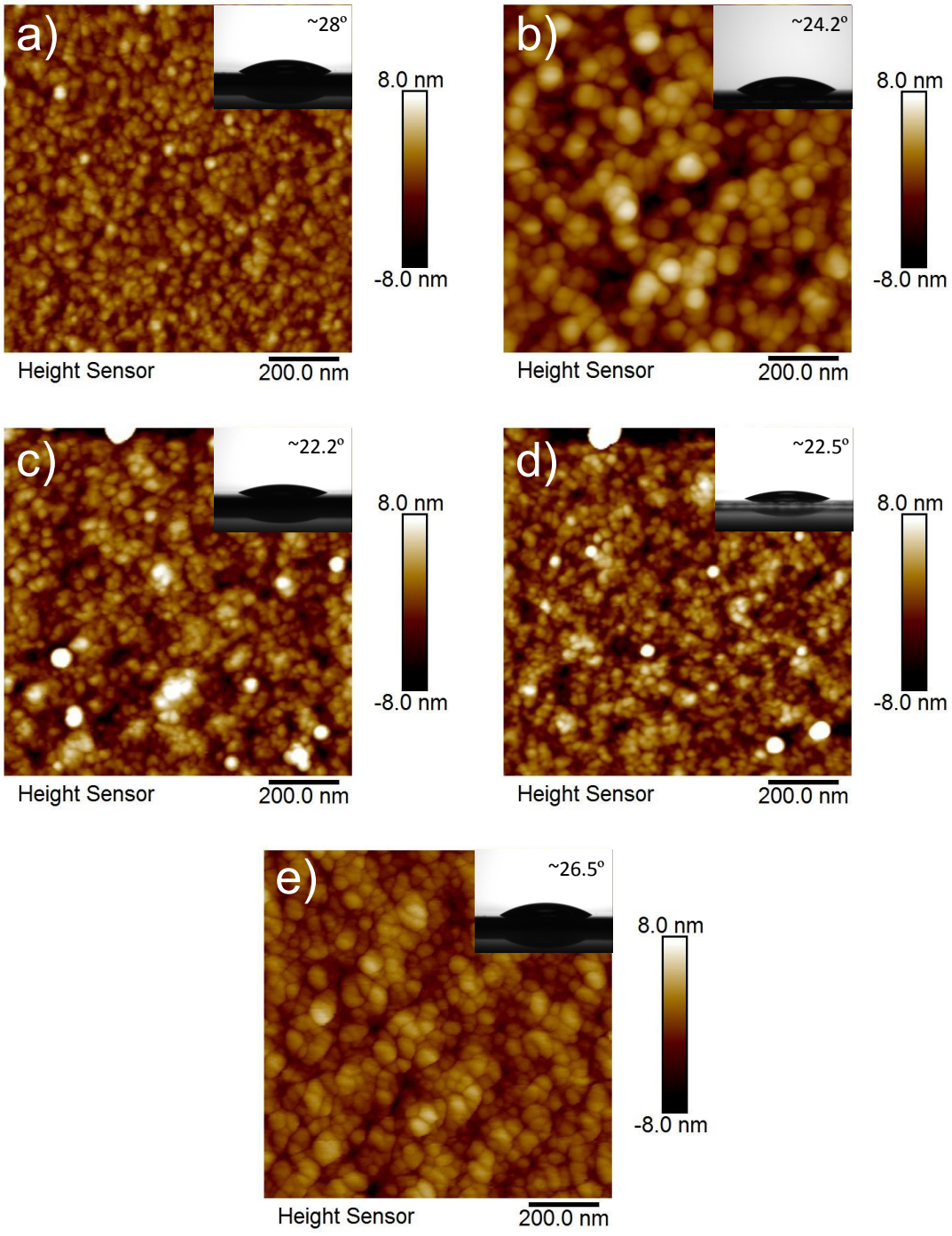

Figure 4.7 AFM images and WCA of TA/DETA coatings on different surfaces, including a) APTES surface, b) TiO2 surface, c) PS surface, d) OTS surface, e) Mica surface. The concentration of TA is kept as 2 mg/mL. The TA/DETA mass ratio is 1:10. The deposition time is 2 h.

4.4 Conclusions

In this work, SFA and AFM were employed to systemically investigate the impact of phenol/amine mass ratio on the cohesion forces between phenol/amine coatings and the deposition behaviors (e.g., coating thickness, morphology and surface roughness) of phenol/amine. TA and DETA were selected as the coating ingredients. TA alone exhibit very limited deposition capability, which is mainly due to the strong electrostatic repulsion between TA particles, severely impeding the formation of TA aggregates deposited on the substrates. When DETA was introduced into the deposition system, the DETA molecules would react with TA molecules to form TA/DETA moieties. The experimental results demonstrated that adding DETA could greatly facilitate the deposition of TA. The cohesion strength and deposition capacity would first increase and the decrease with increasing the mass ratio of DETA, which is largely dependent on the modulation of the contribution of electrostatic repulsion in the overall interaction forces between TA/DETA moieties. Furthermore, the TA/DETA coating was found to possess the ability to adhere to the substrate surfaces of varying surface chemistry and wettability via multiple interactions due to its specific molecular structure and chemical properties. By correlating the adhesion strength and deposition capability of TA/DETA to these surfaces, such adhesion behavior was demonstrated to play a critical role in initiating the TA/DETA deposition on a variety of material surfaces. Our work provides useful insight on the fundamental understanding of interaction mechanism involved in phenol/amine deposition, with implications into the design and development of novel phenol/amine-based coating strategy for a wide range of engineering and bioengineering applications.

4.5 Supporting information

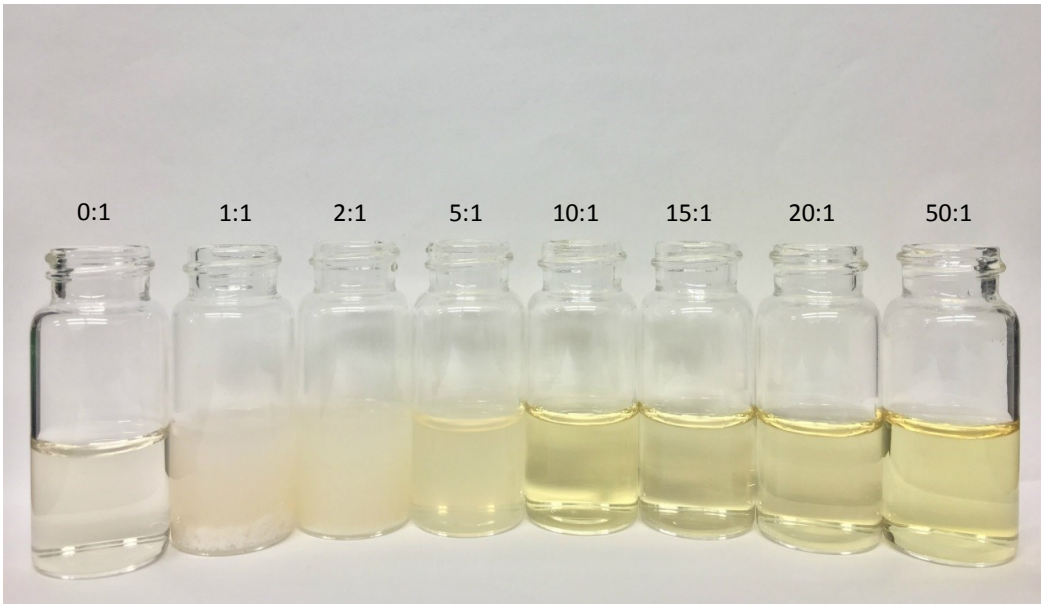

Figure S4.1 Photographs of TA/DETA solution with different mass ratios of TA and DETA (0:1, 1:1, 2:1, 5:1, 10:1, 15:1, 10:1, 15:1, 20:1 and 50:1). The concentration of TA is kept as 2 mg/mL.

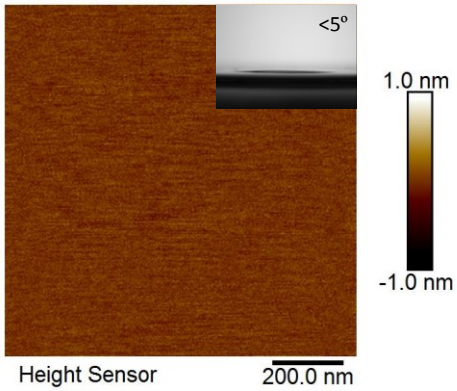

Figure S4.2 AFM image and WCA of bare mica surface.

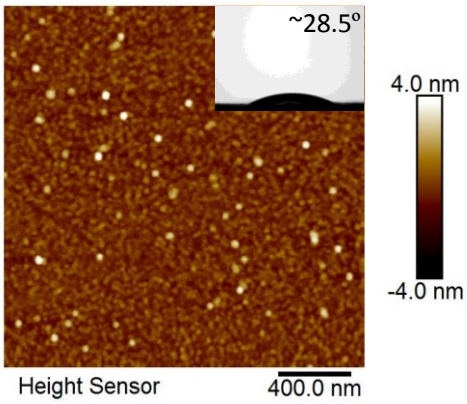

Figure S4.3 AFM images of the as-formed TA/DETA coating deposited on mica surfaces under tris buffer solutions with the TA/DETA mass ratios of 1:10 for 30 min. The concentration of TA is kept as 2 mg/mL.

References

(1) Kord Forooshani, P.; Lee, B. P. *J. Polym. Sci. A* **2017**, *55*, 9-33.

(2) Li, J.; Celiz, A.; Yang, J.; Yang, Q.; Wamala, I.; Whyte, W.; Seo, B.; Vasilyev, N.; Vlassak, J.; Suo, Z. *Science* **2017**, *357*, 378-381.

(3) Brault, N. D.; Gao, C.; Xue, H.; Piliarik, M.; Homola, J.; Jiang, S.; Yu, Q. *Biosens. Bioelectron.* **2010**, *25*, 2276-2282.

(4) Kao, C.-T.; Lin, C.-C.; Chen, Y.-W.; Yeh, C.-H.; Fang, H.-Y.; Shie, M.-Y. *Mater. Sci. Eng. C* **2015**, *56*, 165-173.

(5) Lee, L.-H. In *Book*; Springer, 1988; pp 5-29.

(6) Lee, B. P.; Messersmith, P. B.; Israelachvili, J. N.; Waite, J. H. *Annu. Rev. Mater. Res.* **2011**, *41*, 99-132.

(7) Lee, H.; Dellatore, S. M.; Miller, W. M.; Messersmith, P. B. *Science* **2007**, *318*, 426-430.

(8) Zhang, C.; Ou, Y.; Lei, W. X.; Wan, L. S.; Ji, J.; Xu, Z. K. *Angew. Chem., Int. Ed.* **2016**, *55*, 3054-3057.

(9) Xu, H.; Liu, X.; Su, G.; Zhang, B.; Wang, D. *Langmuir* **2012**, *28*, 13060-13065.

(10) Lim, M.-Y.; Shin, H.; Shin, D. M.; Lee, S.-S.; Lee, J.-C. *Polymer* **2016**, *84*, 89-98.

(11) Liu, Y.; Meng, H.; Messersmith, P. B.; Lee, B. P.; Dalsin, J. L. In *Book*; Springer, 2016; pp 345-378.

(12) Qiu, W.-Z.; Zhong, Q.-Z.; Du, Y.; Lv, Y.; Xu, Z.-K. *Green Chem.* **2016**, *18*, 6205-6208.

(13) Zhang, N.; Jiang, B.; Zhang, L.; Huang, Z.; Sun, Y.; Zong, Y.; Zhang, H. *Chem. Eng. J.* **2019**, *359*, 1442-1452.

(14) Sileika, T. S.; Barrett, D. G.; Zhang, R.; Lau, K. H. A.; Messersmith, P. B. *Angew.*

Chem., Int. Ed. **2013**, *52*, 10766-10770.

(15) Wang, H.; Wu, J.; Cai, C.; Guo, J.; Fan, H.; Zhu, C.; Dong, H.; Zhao, N.; Xu, J. *ACS Appl. Mater. Interfaces* **2014**, *6*, 5602-5608.

(16) Yang, H.-C.; Liao, K.-J.; Huang, H.; Wu, Q.-Y.; Wan, L.-S.; Xu, Z.-K. *J. Mater. Chem. A* **2014**, *2*, 10225-10230.

(17) Zhang, X.; Ren, P.-F.; Yang, H.-C.; Wan, L.-S.; Xu, Z.-K. *Appl. Surf. Sci.* **2016**, *360*, 291-297.

(18) Barclay, T. G.; Hegab, H. M.; Clarke, S. R.; Ginic-Markovic, M. *Adv. Mater. Interfaces*. **2017**, *4*, 1601192.

(19) LaVoie, M. J.; Ostaszewski, B. L.; Weihofen, A.; Schlossmacher, M. G.; Selkoe, D. J. *Nat. Med.* **2005**, *11*, 1214.

(20) Tian, Y.; Cao, Y.; Wang, Y.; Yang, W.; Feng, J. *Adv. Mater.* **2013**, *25*, 2980-2983.

(21) Anderson, T. H.; Yu, J.; Estrada, A.; Hammer, M. U.; Waite, J. H.; Israelachvili, J. N. *Adv. Funct. Mater.* **2010**, *20*, 4196-4205.

(22) Zeng, H.; Hwang, D. S.; Israelachvili, J. N.; Waite, J. H. *Proc. Natl. Acad. Sci. U.S.A.* **2010**, *107*, 12850-12853.

(23) Guo, J.; Richardson, J. J.; Besford, Q. A.; Christofferson, A. J.; Dai, Y.; Ong, C. W.; Tardy, B. L.; Liang, K.; Choi, G. H.; Cui, J. *Langmuir* **2017**, *33*, 10616-10622.

(24) Park, T.; Kim, W. I.; Kim, B. J.; Lee, H.; Choi, I. S.; Park, J. H.; Cho, W. K. *Langmuir* **2018**, *34*, 12318-12323.

(25) Kim, S.; Faghihnejad, A.; Lee, Y.; Jho, Y.; Zeng, H.; Hwang, D. S. *J. Mater. Chem. B* **2015**, *3*, 738-743.

(26) Zhang, C.; Xiang, L.; Zhang, J.; Gong, L.; Han, L.; Xu, Z.-K.; Zeng, H. *Langmuir*

2019.

(27) Lim, C.; Huang, J.; Kim, S.; Lee, H.; Zeng, H.; Hwang, D. S. *Angew. Chem., Int. Ed.* **2016**, *55*, 3342-3346.

(28) Yu, J.; Kan, Y.; Rapp, M.; Danner, E.; Wei, W.; Das, S.; Miller, D. R.; Chen, Y.; Waite, J. H.; Israelachvili, J. N. *Proc. Natl. Acad. Sci. U.S.A.* **2013**, *110*, 15680-15685.

(29) Saiz-Poseu, J.; Mancebo-Aracil, J.; Nador, F.; Busqué, F.; Ruiz-Molina, D. *Angew. Chem., Int. Ed.* **2019**, *58*, 696-714.

(30) Zhang, C.; Gong, L.; Xiang, L.; Du, Y.; Hu, W.; Zeng, H.; Xu, Z.-K. *ACS Appl. Mater. Interfaces* **2017**, *9*, 30943-30950.

(31) Bandara, N.; Zeng, H.; Wu, J. *J. Adhes. Sci. Technol.* **2013**, *27*, 2139-2162.

(32) Eiamchai, P.; Chindaudom, P.; Pokaipisit, A.; Limsuwan, P. *Curr. Appl. Phys.* **2009**, *9*, 707-712.

(33) Xiang, L.; Zhu, S.; Li, M.; Zhang, J.; El-Din, M. G.; Zeng, H. *J. Membr. Sci.* **2019**, *576*, 161-170.

(34) Faghihnejad, A.; Zeng, H. *Langmuir* **2013**, *29*, 12443-12451.

(35) Israelachvili, J.; Min, Y.; Akbulut, M.; Alig, A.; Carver, G.; Greene, W.; Kristiansen, K.; Meyer, E.; Pesika, N.; Rosenberg, K. *Rep. Prog. Phys.* **2010**, *73*, 036601.

(36) Zeng, H.; Huang, J.; Tian, Y.; Li, L.; Tirrell, M. V.; Israelachvili, J. N. *Macromolecules* **2016**, *49*, 5223-5231.

(37) Johnson, K. L.; Kendall, K.; Roberts, A. *Proc. Royal Soc. Lond* **1971**, *324*, 301-313.

(38) Israelachvili, J. *J. Colloid Interface Sci.* **1973**, *44*, 259-272.

(39) Israelachvili, J. N.; Academic press, 2011.

(40) Helm, C. A.; Knoll, W.; Israelachvili, J. N. *Proc. Natl. Acad. Sci. U.S.A.* **1991**, *88*, 8169-8173.

(41) Ościeja, M.; Adamczyk, Z.; Morga, M. *J. Colloid Interface Sci.* **2015**, *438*, 249-258.

(42) Espinosa-Jiménez, M.; Giménez-Martın, E.; Ontiveros-Ortega, A. *J. Colloid Interface Sci.* **1998**, *207*, 170-179.

(43) Riddick, J.; Bunger, W.; Sakano, T.; New York, NY: John Wiley and Sons, 1985.

(44) Zhang, C.; Lv, Y.; Qiu, W.-Z.; He, A.; Xu, Z.-K. *ACS Appl. Mater. Interfaces* **2017**, *9*, 14437-14444.

(45) Sahiner, N.; Sagbas, S.; Sahiner, M.; Demirci, S. *Polym. Degrad. Stab.* **2016**, *133*, 152-161.

(46) Hattori, Y.; Shimada, T.; Yasui, T.; Kaji, N.; Baba, Y. *Anal. Chem.* **2019**.

(47) Huang, J.; Liu, X.; Qiu, X.; Xie, L.; Yan, B.; Wang, X.; Huang, Q.; Zeng, H. *J. Phys. Chem. B* **2017**, *121*, 3151-3161.

(48) Loosli, F.; Stoll, S. *Environ Sci Nano.* **2017**, *4*, 203-211.

(49) Lee, D. W.; Lim, C.; Israelachvili, J. N.; Hwang, D. S. *Langmuir* **2013**, *29*, 14222-14229.

(50) Dalsin, J. L.; Lin, L.; Tosatti, S.; Vörös, J.; Textor, M.; Messersmith, P. B. *Langmuir* **2005**, *21*, 640-646.

Chapter 5. Nanomechanics of π-cation-π Interaction for Bio-inspired Wet Adhesion

5.1 Introduction

Biomolecular structures and functions can be essentially tuned through modulating a variety of non-covalent interactions, among which cation-π interaction is extensively recognized as an important binding mechanism in many biological processes such as potassium-selective channel, molecular recognition, bio-adhesion and biomolecular self-assembly.[1-3] In previous studies, binary cation-π interaction is commonly considered when investigating the cation-π interaction nature, via both computational and experimental approaches.[4-5] However, due to the complexity of biological systems, in practical biological processes, a single cation is commonly in close proximity with more than one π-conjugated units. For example, in K^+ channel and nicotinic acetylcholine receptor channel, both K^+ and acetylcholine (bearing NH_4^+ group) are surrounded by a variety of π-conjugated residues (*i.e.,* phenylalanine, tyrosine and tryptophan) in the channel pores;[6] in chain folding and assembly of protein/peptide,[7] cation could also be closely packed with a couple of π-conjugated residues. In such circumstances, the interaction behaviors between cations and π-conjugated units could be essentially different with relatively simple binary cation-π interaction. In 1993, a computational study has examined the validity of π-cation-π interaction in K^+ channel,[8] however over the past two decades, experimental evidence of such type of ternary interaction is still scarce, which holds the key to fully understand cation-π interaction mechanisms.[4]

In marine science, robust wet adhesion can be readily and effectively achieved by marine organisms on various substrates in seawater.[7, 9-11] In most bioadhesives, catechol groups and the polymerization of catechol to poly(catechol) (initiated by the natural oxidation of catechol to quinone to form a poly(catechol)) under mild alkaline seawater environment were found to be essential for interfacial adhesion.[7, 12-14] Recently, binary cation-π interaction between π-conjugated catechol/quinone groups and cationic moieties (*e.g.,* lysine with NH_3^+ group) was demonstrated as another pivotal binding strategy in wet adhesion.[15-17] The binary cation-π binding pair between a NH_3^+ group and a π-conjugated group covalently bonded to two different polymer backbones enables the bridging between polymer chains, thus enhancing their adhesion. Salt cation (*i.e.,* K^+) was previously regarded to undermine the adhesion through competing with the cationic moieties in the as-formed binary cation-π complexes.[4] Interestingly, in this work, in the absence of other cationic moieties, salt cations alone is found to enhance the binding force of π-conjugated catecholic adhesive using pyrocatechol (PC) (*viz.,* catechol) as the model compound. It's worth mentioning, although divalent cations including Ca^{2+} and Mg^{2+} also widely exist in seawater, to eliminate the influence of chelation between divalent cations and phenolic hydroxyl groups, only monovalent salt cations were utilized to study the underlying interaction mechanism. Such enhanced adhesion force cannot be explained by traditional binary cation-π interaction because K^+ is not chemically bonded to any polymer backbone to form polymer bridging. Herein, ternary π-cation-π interaction was identified to be the primary driving force of the adhesion through bridging between π-conjugated moieties by using a surface forces apparatus (SFA) to systematically measure the adhesion of poly(pyrocatechol) (pPC) films under various saline conditions (*i.e.,* salinity and salt type).

Combining with atomic force microscopy (AFM) imaging, the assembly of π-conjugated pPC films with the coexistence of cations was also precisely characterized. This study presents the first experimental evidence of π-cation-π interaction with its nanomechanics directly quantified, and unravels its contribution to the assembly behavior of π-conjugated moieties with coexistence of cations.

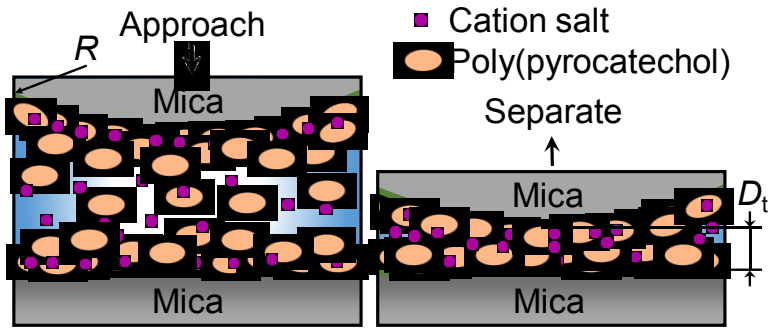

Figure 5.1 Schematic of force measurement using a surface forces apparatus (SFA). Two opposing mica surfaces (radius R) coated with poly(pyrocatechol) (pPC) films first approached to each other until they come into contact to determine the thickness of confined layers (D_t), and then were separated, during which the adhesion force (F_{ad}) was measured.

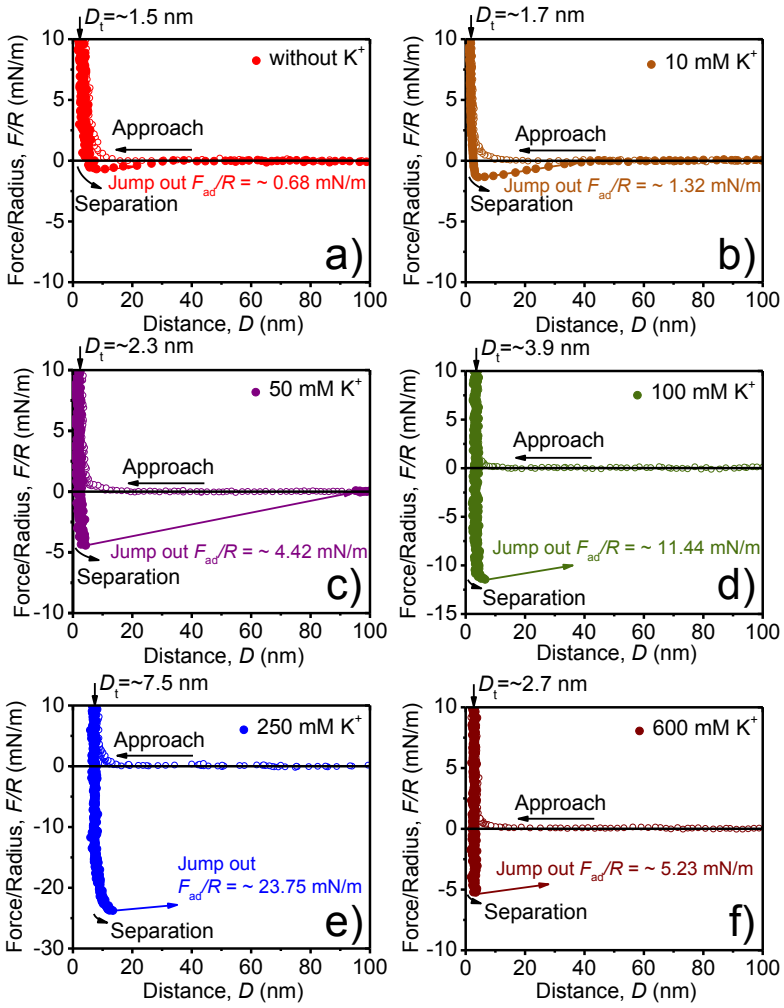

Figure 5.2 Force-distance profiles measured between pPC coatings after in-situ deposition for 8 h in 50 mM bicine buffer solution at pH 8.5 containing 2mg/mL PC and different K^+ concentrations: a) 0, b) 10, c) 50, d) 100, e) 250 and f) 600 mM.

5.2 Materials and Experimental Methods

5.2.1 Materials.

Pyrocatechol (PC), lithium chloride (LiCl), sodium chloride (NaCl), potassium chloride (KCl), tetramethylammonium chloride (NMe_4Cl), potassium nitrate (KNO_3) and N, N-bis(2-hydroxyethyl) glycine (bicine) were purchased from Sigma-Aldrich (Canada).

All chemical reagents were used without further purification. The aqueous solutions were prepared using Milli-Q water with the resistivity of 18.2 MΩ·cm.

5.2.2 Fabrication and characterization of poly(pyrocatechol) (pPC) films

The PC (2 mg/mL) and different concentration of KCl (0 mM, 10 mM, 50 mM, 100 mM, 250 mM and 600 mM) were dissolved in bicine buffer solution (50 mM, pH = 8.5). The pPC-coated surfaces were prepared by immersing the substrates into above solutions for certain time at 25 °C. Subsequently, the as-deposited substrates were washed by deionized water and blow dried by nitrogen gas before use. Other pPC films obtained using different types of alkaline metal salt followed the same procedure. UV adsroption spectra of the deposition solutions was measured using a UV–vis spectrophotometer (Thermo Scientific Evolution™ 300 UV-visible). The surface morphology and chemical component of the as-deposited samples were characterized by atomic force microscope (AFM) (Bruker, Santa Barbara, CA) and XPS spectrophotometer (Kratos AXIS 165). The thickness of the as-formed pPC films was determined using a spectroscopic ellipsometer (Sopra GESP-5, France). A contact angle goniometer (ramé-hart instrument, Succasunna, NJ) was used to measure the static water contact angle on film surfaces.

5.2.3 Surface forces measurements using surface forces apparatus (SFA)

A surface forces apparatus (SFA) was employed to investigate the nanomechanical properties of pPC film under various aqueous solutions in a symmetric configuration (as shown in **Figure 5.1**). Detailed SFA experimental setup can be found in previous reports.[18-20] In this work, mica was selected as a model substrate due to its molecularly smooth feature of the basal plane to eliminate the influence of substrate roughness. Two back-silvered

mica sheets (1-5 μm) were glued on the cylindrical silica disks with radius R= 2 cm. During the force measurement under the condition of *in situ* deposition of PC, the two disks were mounted into the SFA chamber in a crossed-cylinder geometry, which was locally equivalent to a sphere of radius R approaching a flat surface when the separation distance $D \ll R$. One of the surfaces was held by a cantilevered spring. A droplet of 100 μL PC bicine buffer solution with different salt concentrations was injected between two mica surfaces for *in situ* deposition of PC. The absolute separation distance between two mica surfaces can be obtained in real time and *in situ* by monitoring the optical interference fringes of equal chromatic order (FECO) based on the multiple beam interferometry (MBI) optical technique. The interaction force F between the surfaces was measured as a function of surface separation distance D. The reference distance (D = 0) was determined at the contact between two bare mica surfaces in air from an independent measurement. The pPC film thickness D_t was determined from the wavelength shift of the optical interference fringes of equal chromatic order (FECO) patterns before and after deposition. The interaction force was deduced from the deflection of the spring using Hooke's law. The measured adhesion force F_{ad} is correlated to the adhesion energy per unit area (W_{ad}) between two flat surfaces Wad based on the Johnson-Kendall-Roberts (JKR) model, where by $F_{ad}/R = 1.5\pi W_{ad}$.[21, 22]

5.3 Results and Discussion

The schematic setup of SFA force measurement is shown in **Figure 5.1**. PC solutions (2 mg/mL, 50 mM bicine buffer at pH 8.5) with different K^+ concentrations were injected into the gap between two opposing mica surfaces, then the in-situ polymerization of PC and pPC deposition on mica surfaces were initiated. **Figure 5.2a-e** show the normalized

force (F/R)-distance (D) profiles between pPC coatings in aqueous solutions. A "jump-out" behavior was detected on the force curves during surface separation, suggesting the interfacial adhesion between pPC coatings. With K^+ concentration increasing from 0 to 250 mM, the normalized adhesion force F_{ad}/R and corresponding coating thickness D_t dramatically increased from ~0.68 mN/m and ~1.5 nm, to ~23.75 mN/m and ~7.5 nm, respectively. The pPC film deposited in 250 mM KNO_3 buffer solution was further characterized using X-ray photoelectron spectroscopy (XPS) (**Figure S5.1**). K to Si ratio significantly increased to ~0.78 compared with that of mica (~0.37), suggesting K^+ can actively participate in enhancing pPC assembly. Such observation is particularly interesting since the enhanced adhesion would not be expected to arise from binary cation-π interaction between K^+ and π-conjugated pPC due to the lack of bridging between π-conjugated moieties.

The underlying driving force for pPC deposition was further investigated by performing SFA force measurement under acidic pH to suppress PC's oxidation and polymerization.[9]The observed limited pPC deposition capability and negligible adhesion at 250 mM K^+ (**Figure S5.2**) indicated that the oxidative polymerization of PC was a prerequisite for wet deposition.[9, 23] UV-vis spectra of PC solution after polymerization in absence/presence of K^+ showed no observable difference (**Figure S5.3**), suggesting that K^+ had negligible influence on PC's polymerization. Thus, the assembly of pPC coating should be a hierarchical process, *i.e.,* the polymerization to pPC, and the simultaneous assembly with K^+ being involved. Furthermore, the adhesion and assembly enhanced by K^+ was disclosed to arise from non-covalent interactions through consecutive force measurements between two pPC films in 250 mM K^+ buffer solution, during which reversible adhesion

(F_{ad}/R 23.93 ± 0.57 mN/m) was measured (**Figure S5.4**).[17] Electrical double layer, van der Waals, and hydrophobic interactions could not play the dominative role in enhancing adhesion with increased K^+ up to 250 mM, due to their insensitivity to salt concentration higher than 50 mM.[24] As a surprise from 1993, the ternary π-cation-π interaction proposed in a pioneering computational study[8] is likely to be the driving force for the strong adhesion and enhanced assembly behavior of pPC films experimentally observed in this study. As illustrated in **Figure 5.3a**, K^+ could simultaneously interact with two π-conjugated groups on different pPC moieties through ternary π-cation-π interaction, hence enhancing the wet adhesion through physical bridging effect. Therefore, when increasing K^+ concentration from 0 to 250 mM, more π-K^+-π complexes formed to enhance the adhesion between pPC films. AFM topographic images of the as-prepared pPC film (**Figure 5.4a-e**) straightforwardly depicted their assembly behaviors by relating aggregate size to the surface roughness (AFM image of bare mica shown in **Figure S5.5**). Without K^+, pPC film was quite smooth with very small aggregate size (surface roughness ~ 0.32 nm), suggesting that in absence of cations, the self-assembly of pPC moiety was not significant. With gradually increasing K^+ concentration to 250 mM, the aggregate size evidently increased with surface roughness ~3.32 nm, further demonstrating that K^+ facilitated the pPC self-assembly possibly through forming ternary π-cation-π complex. More as-formed ternary complexes result in the growth of larger pPC aggregates to form thicker pPC film on surface.

Interestingly, when K^+ concentration increasing from 250 mM to 600 mM, the adhesion and coating thickness measured in SFA experiments decreased to ~5.23 mN/m and ~2.7 nm, respectively (**Figure 5.2f**), The pPC aggregate size also obviously decreased

(surface roughness ~1.23 nm, **Figure 5.4f**). The undermined adhesion and assembly of pPC were attributed to that the excess of K^+ could lead to the formation of abundant binary K^+-π binding pairs instead of π-K^+-π complexes (**Figure 5.3b**). The abolishment of π-K^+-π bridging would weaken the adhesion and impair the assembly of pPC, thus only small pPC aggregates could form and deposit on surface. As such, this study presented the first experimental evidence of π-cation-π interaction in aqueous media, and provide new nanomechanical insights that such ternary interaction could transform to binary cation-π interaction. Besides adhesion, pPC aggregate size and film thickness can also be tuned by varying K^+ concentration. Such findings suggest that the nanomechanical nature of ternary π-cation-π interaction is essentially different with binary cation-π interaction, which can be readily employed to better understand and modulate other biological processes. For example, by varying its dosage, K^+ may participate and modulate the folding/unfolding and inter/intra-chain recognition of numerous biomolecules containing π-conjugated groups (*e.g.,* enzyme) through π-cation-π bridging to realize different biological functions such as enzymatic activity.

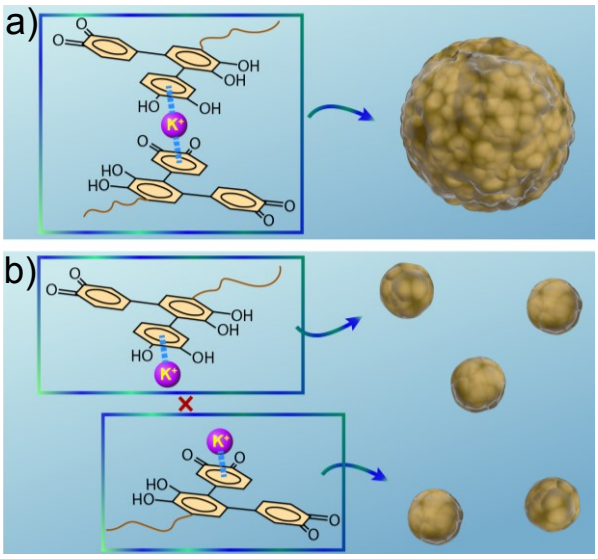

Figure 5.3 Schematic illustration of a) π-cation-π complex can induce bridging and promote the assembly of larger pPC aggregates; and b) binary cation–π binding pairs form due to excess K^+, leading to bridging abolishment and undermined assembly with smaller pPC aggregates.

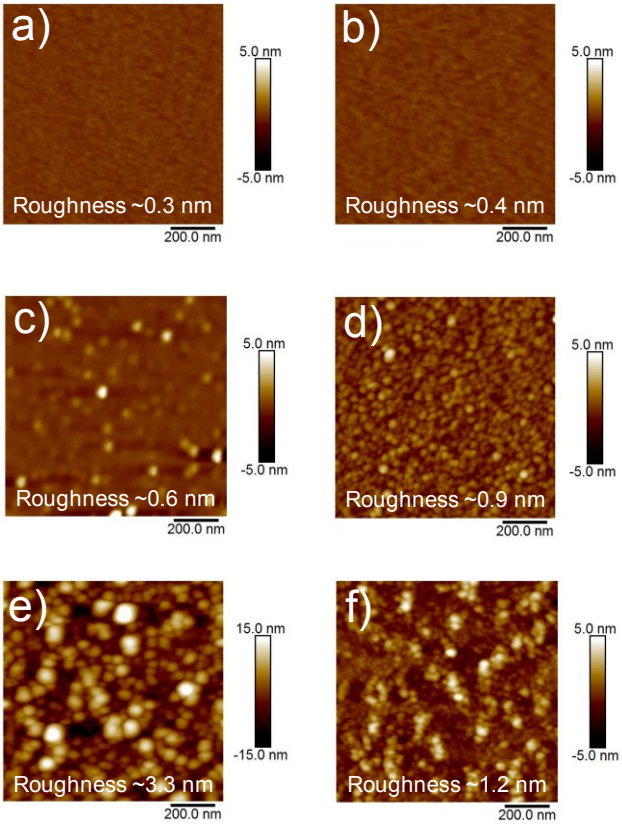

Figure 5.4 Atomic force microscopy (AFM) topographic images of pPC film after deposition in PC solutions containing different K^+ concentrations for 8 h: a) 0, b) 10, c) 50, d) 100, e) 250 and f) 600 mM.

We further investigated the nanomechanical nature of π-cation-π interaction via evaluating the impact of cation species on the adhesion and deposition behavior of pPC coatings using SFA (**Figure 5.5a-c**). With the same cation concentration (250 mM), the adhesion strength followed the order of $NMe_4^+ > K^+ > Na^+ > Li^+$ (**Figure 5.5d**), which essentially agreed with the π-cation-π strength trend based on theoretical simulation.[8] Thus, based on these studies, the binding strength trend of ternary π-cation-π should be dependent on the hydration strength of different cations.[4, 25-27] Stronger hydration of cations would lead to higher desolvation penalty when forming π-cation-π complex, thus impairing the

ternary complex formation. Therefore, higher adhesion strength and larger aggregate size of pPC films (**Figure 5.6**) were observed at cations with lower hydration strength (*i.e.,* K^+ and NMe_4^+), implying that both adhesion and assembly behaviors of π-conjugated groups could be modulated by varying cation species. This finding provides nanomechanical insights into the biological processes of selective molecular recognition and transport involving multiple π-conjugated groups surrounding cations, *e.g.,* the selective transport of K^+ over Li^+ and Na^+ through K^+ channel and the K^+ channel blocking by tetraethylammonium (containing NMe_4^+), in which the channel pore is rich in multiple aromatic residues.

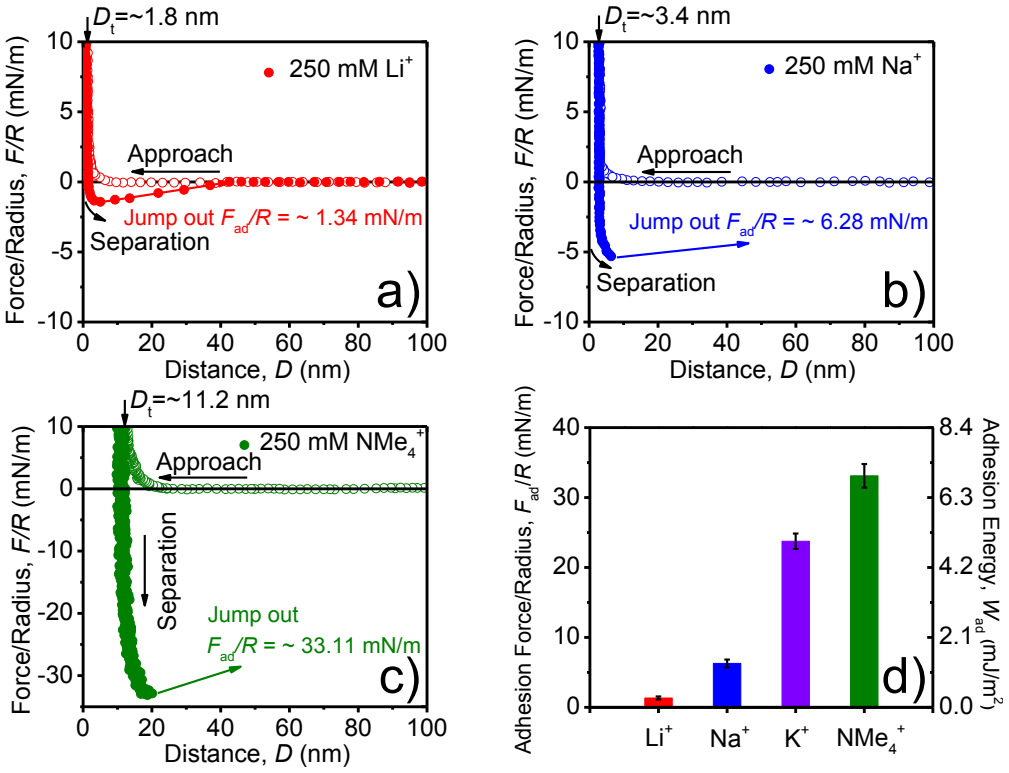

Figure 5.5 Force-distance profiles measured between pPC films after in-situ deposition for 8 h in PC solution containing 250 mM a) Li^+, b) Na^+, and c) NMe_4^+. e) The normalized adhesion forces (F_{ad}/R) and adhesion energy (W_{ad}) as a function of salt specie.

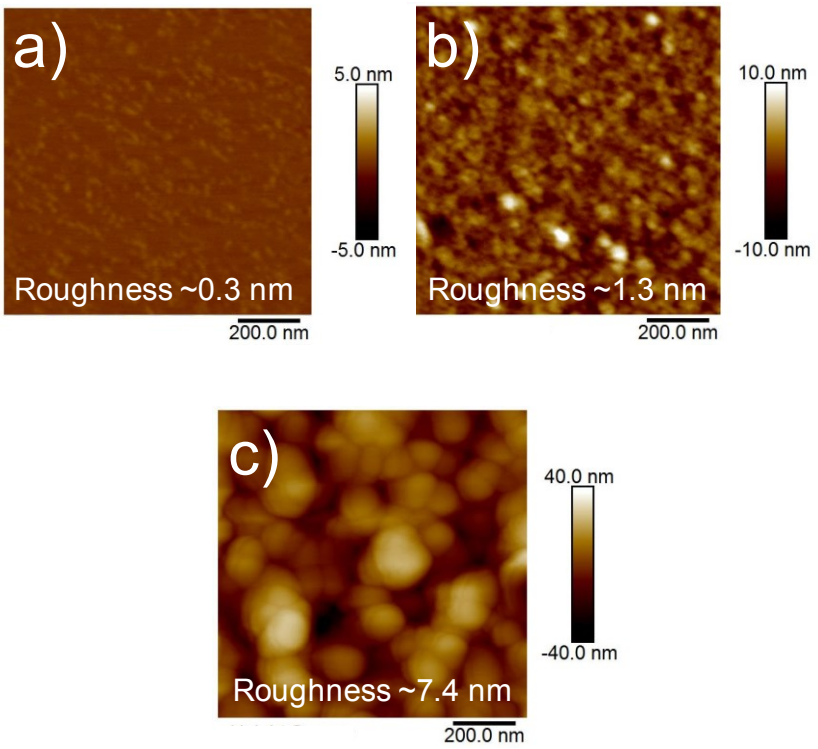

Figure 5.6 AFM topographic images of pPC films on mica deposited in PC solution containing 250 mM a) Li^+, b) Na^+ and c) NMe_4^+.

5.4 Conclusions

In this study, we have presented the first experimental demonstration and quantification of the nanomechanics of π-cation-π interaction through direct force measurements on a model π-conjugated poly(pyrocatechol) (pPC) system with K^+. Its contribution to mediating the assembly of π-conjugated molecules has been carefully monitored by AFM topographic imaging. The ternary π-cation-π interaction enables bridging effect of K^+ with two π-conjugated moieties, leading to the enhanced wet adhesion and assembly of pPC films. Interestingly, such ternary interaction can transform to binary cation–π interaction when K^+ concentration increases, resulting in the abolishment of bridging and the undermined adhesion and assembly. Furthermore, the π-cation-π

interaction is general for various cation species with the binding strength following the trend of $NMe_4^+ > K^+ > Na^+ > Li^+$. The bridging effect of ternary π-cation-π interaction and its transformation to binary cation-π provide new insights into bio-inspired wet-adhesion and opens a new route to develop novel bio-adhesives with reversible adhesive properties for applications in seawater and physiological fluids. More broadly, by varying the dosage of salt cations that ubiquitously exist in living organism, the transition between the folding/assembly state and unfolding/disassembly of many biomolecules (*e.g.,* proteins and peptides) containing aromatic groups could be realized. The bridging strength trend may be responsible for understanding many biological phenomena such as ion selectivity in K^+ channel. Thus, the nanomechanism of π-cation-π interaction unraveled in this work holds great promise in bioengineering application, with implications for regulating a broad range of biological activities.

5.5 Supporting information

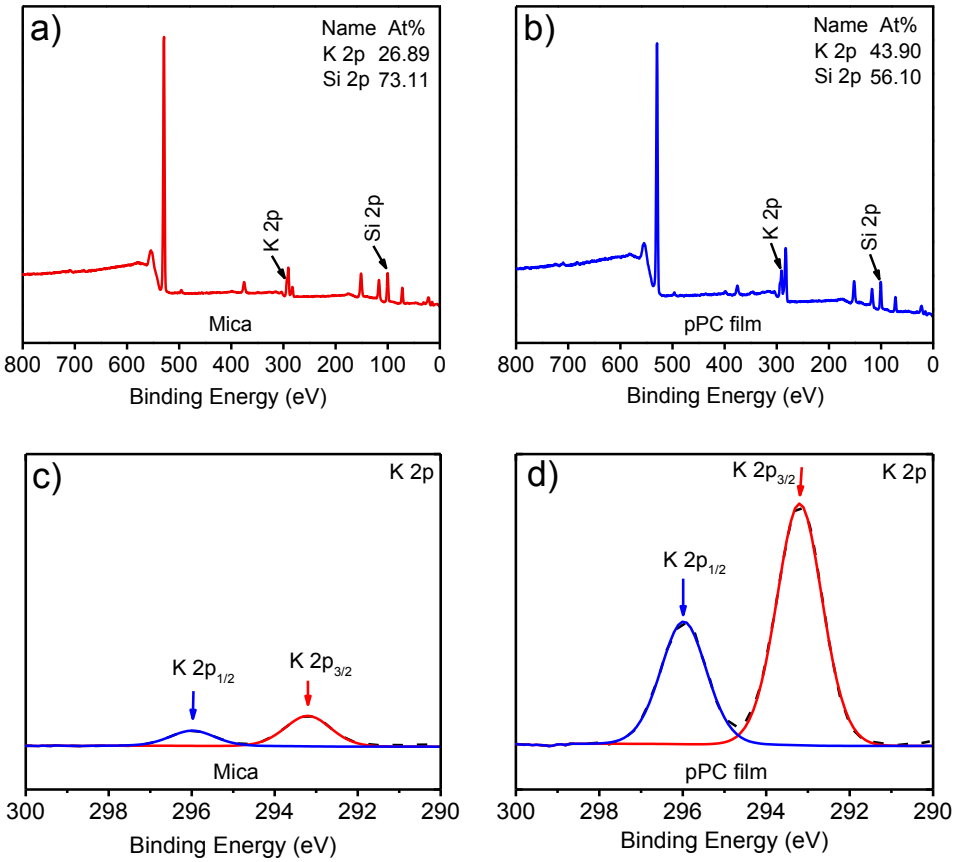

Figure S5.1 X-ray photoelectron spectroscopy (XPS) survey of a) mica and b) pPC film deposited on mica. High-resolution XPS spectral of K 2p of c) bare mica and d) poly(pyrocatechol) (pPC) film. The film deposition condition is at pH 8.5 pyrocatechol bicine buffer solution containing 250 mM K^+. The deposition time is 8 h. For the mica deposited by pPC film, the sample was throughly rinsed by Milli-Q water to remove the free K^+ ions followed by drying the film and preparing for charaterization.

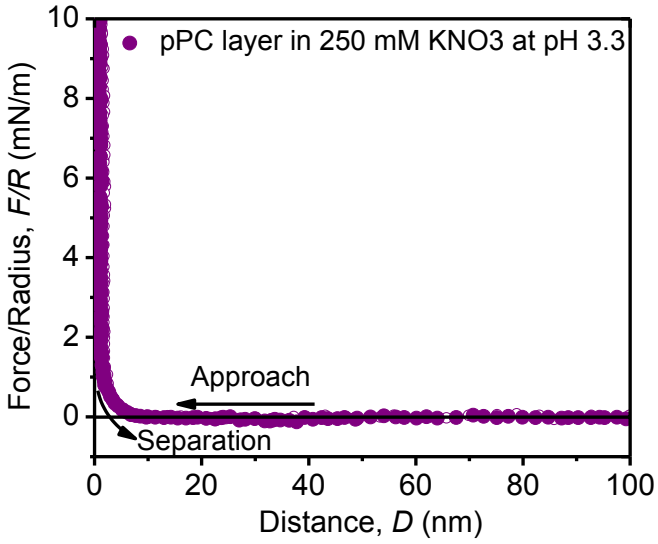

Figure S5.2 a) Force-distance profiles measured between pPC layers after in situ deposition for 8 h under acetate buffer solution (pH=3.3, 10 mM) containing 250 mM KNO_3.

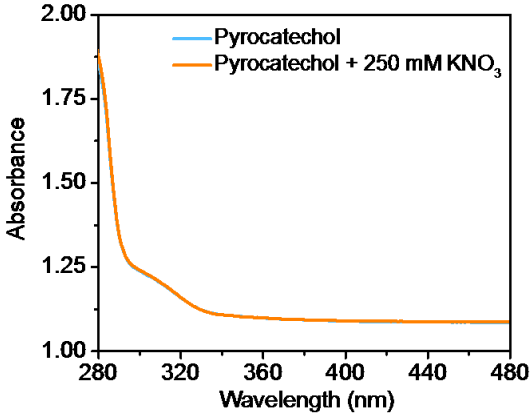

Figure S5.3 Influence of salt on the polymerization of catechol (PC) in bicine buffer solution (pH=8.5, 10 mM) detected by a UV-vis spectrophotometer.

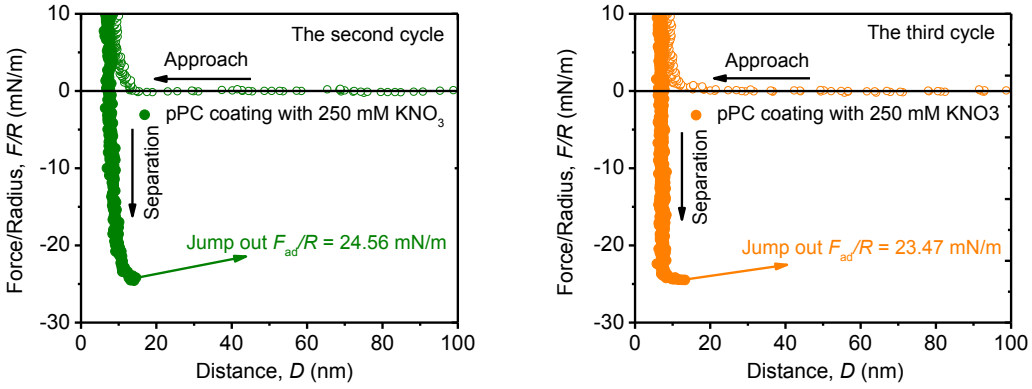

Figure S5.4 Force-distance curves of pPC films after in situ polymerization at pH 8.5 with 250 mM K^+ at the same interacting position under sequential force measurements. The concentration of PC is 2 mg/mL.

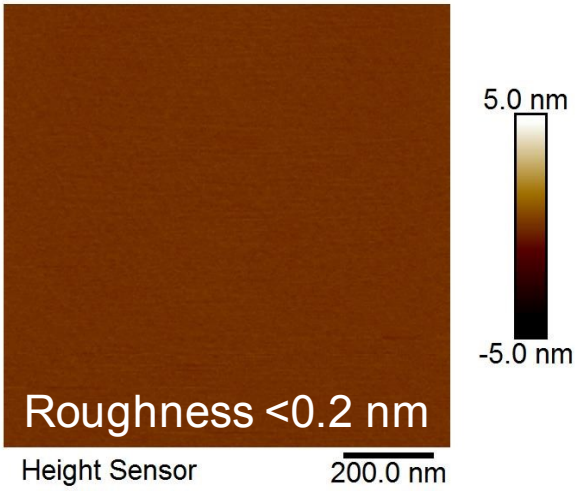

Figure S5.5 AFM image and WCA of bare mica surface. The bare mica surface was very flat and featureless with root-mean-square roughness of ~0.2 nm.

Reference

(1) Khademi, S.; O'Connell, J.; Remis, J.; Robles-Colmenares, Y.; Miercke, L. J.; Stroud, R. M. *Science* **2004**, *305*, 1587-1594.

(2) Mahadevi, A. S.; Sastry, G. N. *Chem. Rev.* **2012**, *113*, 2100-2138.

(3) Pletneva, E. V.; Laederach, A. T.; Fulton, D. B.; Kostić, N. M. *J. Am. Chem. Soc.* **2001**, *123*, 6232-6245.

(4) Lu, Q.; Oh, D. X.; Lee, Y.; Jho, Y.; Hwang, D. S.; Zeng, H. *Angew. Chem., Int. Ed.* **2013**, *52*, 3944-3948.

(5) Rashkin, M. J.; Hughes, R. M.; Calloway, N. T.; Waters, M. L. *J. Am. Chem. Soc.* **2004**, *126*, 13320-13325.

(6) Dougherty, D. A. *Science* **1996**, *271*, 163-168.

(7) Lee, B. P.; Messersmith, P. B.; Israelachvili, J. N.; Waite, J. H. *Annu. Rev. Mater. Res.* **2011**, *41*, 99-132.

(8) Kumpf, R. A.; Dougherty, D. A. *Science* **1993**, *261*, 1708-1710.

(9) Maier, G. P.; Rapp, M. V.; Waite, J. H.; Israelachvili, J. N.; Butler, A. *Science* **2015**, *349*, 628-632.

(10) Waite, J. H. *J. Exp. Biol.* **2017**, *220*, 517-530.

(11) Oh, D. X.; Shin, S.; Yoo, H. Y.; Lim, C.; Hwang, D. S. *Korean J. Chem. Eng.* **2014**, *31*, 1306-1315.

(12) Sever, M. J.; Weisser, J. T.; Monahan, J.; Srinivasan, S.; Wilker, J. J. *Angew. Chem., Int. Ed.* **2004**, *43*, 448-450.

(13) Stewart, R. J.; Ransom, T. C.; Hlady, V. *J. Polym. Sci., Part B: Polym. Phys.* **2011**, *49*,

757-771.

(14) Zhao, Y.; Wu, Y.; Wang, L.; Zhang, M.; Chen, X.; Liu, M.; Fan, J.; Liu, J.; Zhou, F.; Wang, Z. *Nat. Commun.* **2017**, *8*, 1-8.

(15) Gebbie, M. A.; Wei, W.; Schrader, A. M.; Cristiani, T. R.; Dobbs, H. A.; Idso, M.; Chmelka, B. F.; Waite, J. H.; Israelachvili, J. N. *Nat. Chem.* **2017**, *9*, 473.

(16) Hong, S.; Wang, Y.; Park, S. Y.; Lee, H. *Sci. Adv.* **2018**, *4*, eaat7457.

(17) Lim, C.; Huang, J.; Kim, S.; Lee, H.; Zeng, H.; Hwang, D. S. *Angew. Chem. Int. Ed.* **2016**, *55*, 3342-3346.

(18) Faghihnejad, A.; Zeng, H. *Langmuir* **2013**, *29*, 12443-12451.

(19) Zeng, H.; Kristiansen, K.; Wang, P.; Bergli, J.; Israelachvili, J. *Langmuir* **2011**, *27*, 7163-7167.

(20) Israelachvili, J.; Min, Y.; Akbulut, M.; Alig, A.; Carver, G.; Greene, W.; Kristiansen, K.; Meyer, E.; Pesika, N.; Rosenberg, K. *Rep. Prog. Phys.* **2010**, *73*, 036601.

(21) Israelachvili, J. N.; Academic press, 2011.

(22) Zeng, H.; Hwang, D. S.; Israelachvili, J. N.; Waite, J. H. *Proc. Natl. Acad. Sci. U.S.A.* **2010**, *107*, 12850-12853.

(23) Wei, Q.; Zhang, F.; Li, J.; Li, B.; Zhao, C. *Polym. Chem.* **2010**, *1*, 1430-1433.

(24) Israelachvili, J. N.; Academic press, 2015.

(25) Gallivan, J. P.; Dougherty, D. A. *J. Am. Chem. Soc.* **2000**, *122*, 870-874.

(26) Rao, J. S.; Zipse, H.; Sastry, G. N. *J. Phys. Chem. B* **2009**, *113*, 7225-7236.

(27) Ahern, C. A.; Eastwood, A. L.; Lester, H. A.; Dougherty, D. A.; Horn, R. *J. Gen. Physiol.* **2006**, *128*, 649-657.

Chapter 6 Nanomechanics of Anion-π Interaction in Aqueous Media

6.1 Introduction

Charged species and π-conjugated moieties ubiquitously exist in biological systems, and their involvement in noncovalent interactions is significant in molecular adhesion and recognition, protein folding, and many other important biological processes.[1-3] Comprehensive understanding of noncovalent interactions, e.g., π-π stacking, cation-π interactions, holds great promise for biomedical techniques, supramolecular chemistry and engineering applications.[4-8] Yet, anion-π interactions, as a relatively new type of noncovalent interactions, were only recognized recently and computationally to participate in biological processes (e.g., enzymatic activity of urate oxidase and DNA sequence recognition by phosphodiesterase).[2, 9-10] However, experimental studies of anion-π interaction remain limited, and the nanomechanics nature remains unsurveyed.

In the field of wet-adhesion, marine organisms can form robust bioadhesives on solid surfaces under aqueous saline environment, as a great challenge in technology to date. The π-conjugated catechol group in 3,4-dihydroxyphenylalanine (dopa, **Figure 6.1a**) has been identified as the pivotal adhesive promotor in bioadhesive proteins, which undergoes spontaneous oxidation and forms poly(catechol) under weak alkaline seawater condition.[11-13] Recently, cation-π interactions between the abundant π-conjugated catecholic/poly(catechol) residues and cationic residues (e.g., Lys and Arg) have been recognized as a key mechanism in promoting the cohesion of bioadhesives.[1, 14-15] While salt cations (e.g., K^+) have been found to tremendously undermine the cohesion between cationic residues and π-conjugated moieties due to competitive interactions, the extensive

presence of cations in seawater has not frustrated the wet-adhesion of marine organisms, suggesting additional interaction mechanism being involved.[14-15]

In bioadhesives, anionic phosphoserine (with phosphate ester group, **Figure 6.1a**) commonly abounds together with dopa.[16] For example, sandcastle worm glue proteins overall contain ~30 mol% phosphoserine and 2-3 mol% dopa.[17-18] Mfp-5, a primary protein in surface adhesion of mussel, contains 10 mol% phosphoserine and 25 mol% dopa.[18-19] However, the noncovalent interactions between phosphate ester, intrinsically as an anion, and the π-conjugated catecholic moieties, and the consequent contribution to under seawater adhesion is seldom considered. In this work, anion-π interaction is unraveled to exist between anionic phosphate ester and π-conjugated poly(catechol) moieties, and indispensably contribute to wet-adhesion, presenting the *first* experimental study on the nanomechanics of anion-π interaction.

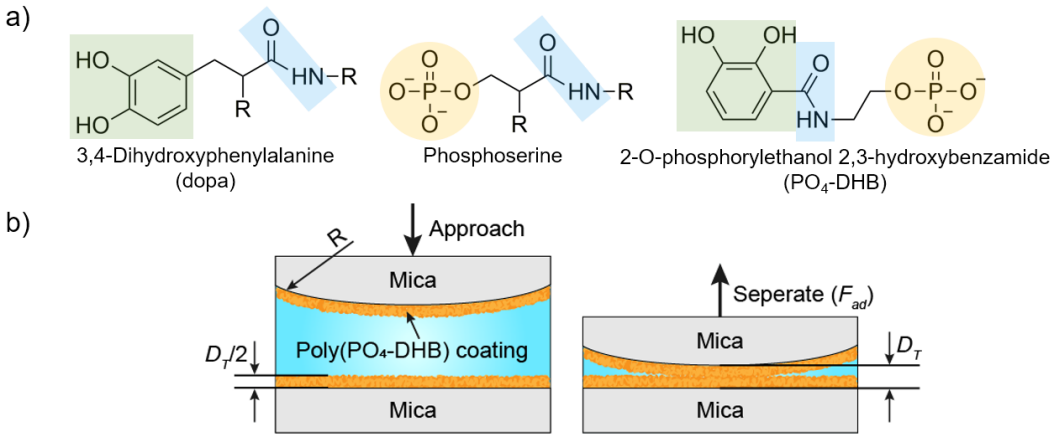

Figure 6.1 a) Structures of dopa and phosphoserine residues, and PO_4-DHB. b) Schematic of SFA measurement. Two opposing curved mica surfaces (radius R) coated with poly(PO_4-DHB) films first approached to each other, then were compressed and separated to measure the adhesion force (F_{ad}) and thickness of confined films (D_T).

2-O-phosphorylethanol 2,3-hydroxybenzamide (PO_4-DHB, **Figure 6.1a**) was synthesized as a model compound to mimic the natural bioadhesives (synthesis and characterization shown in Supporting Information). A surface forces apparatus (SFA) was used to directly quantify the nanomechanics of anion effect of phosphate ester on the wet-adhesion of π-conjugated catecholic adhesives in saline solution (pH 8.4, 50 mM bicine buffer). Typical SFA experimental setup is illustrated in **Figure 1b**.[20] Typically, PO_4-DHB saline buffer solution was injected in the gap between two opposing atomically smooth mica surfaces (radius R), then PO_4-DHB polymerized and poly(PO_4-DHB) coatings formed on both mica surfaces. Force-distance curves (F/R vs. D) between poly(PO_4-DHB) coatings were obtained during their approach and separation, with thickness of each coating determined as $D_T/2$. The deposition of poly(PO_4-DHB) coating on mica substrate was also verified by atomic force microscopy (AFM) topographic imaging and time-of-flight negative secondary ion mass (ToF-SIMS) analysis (**Figure S6.1-S6.2**).

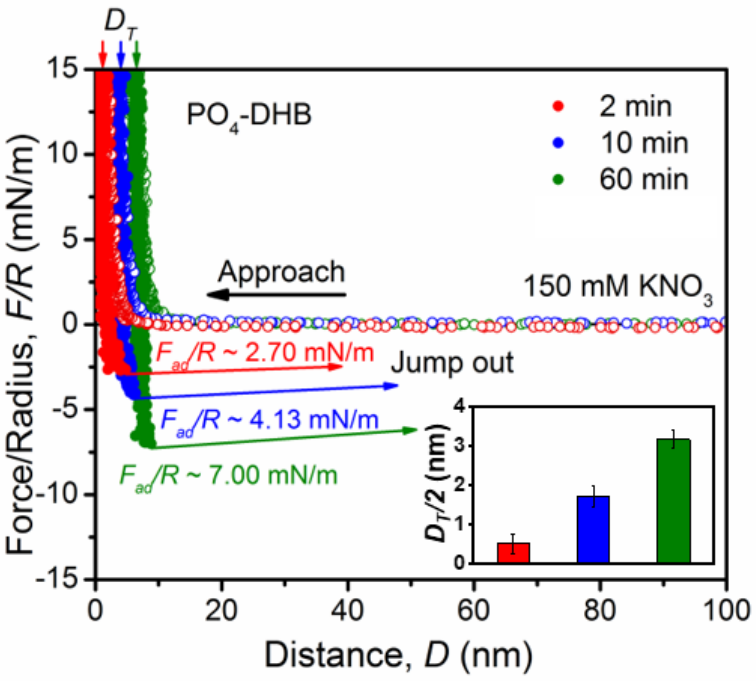

Figure 6.2 Force-distance profiles as a function of deposition time *t* of poly(PO_4-DHB) films in 150 mM KNO_3 buffer solution (50 mM bicine, pH 8.4) with initial concentration of PO_4-DHB as 2 mg/mL. The inset shows thickness (D_T/2) of each poly(PO_4-DHB) films.

In 150 mM KNO_3 buffer solution, both adhesive forces and thickness of poly(PO_4-DHB) films increased with deposition time *t* (**Figure 6.2**). With *t*=1 hr, the negatively charged poly(PO_4-DHB) coatings present robust adhesion (F_{ad}/R= ~7 /m) comparable to dopa-Fe^{3+} chelation system,[21-22] and cation-π interaction systems such as poly(catecholamine).[15] The adhesion was repetitive and reversible (**Figure S3**), which should be attributed to noncovalent interactions.

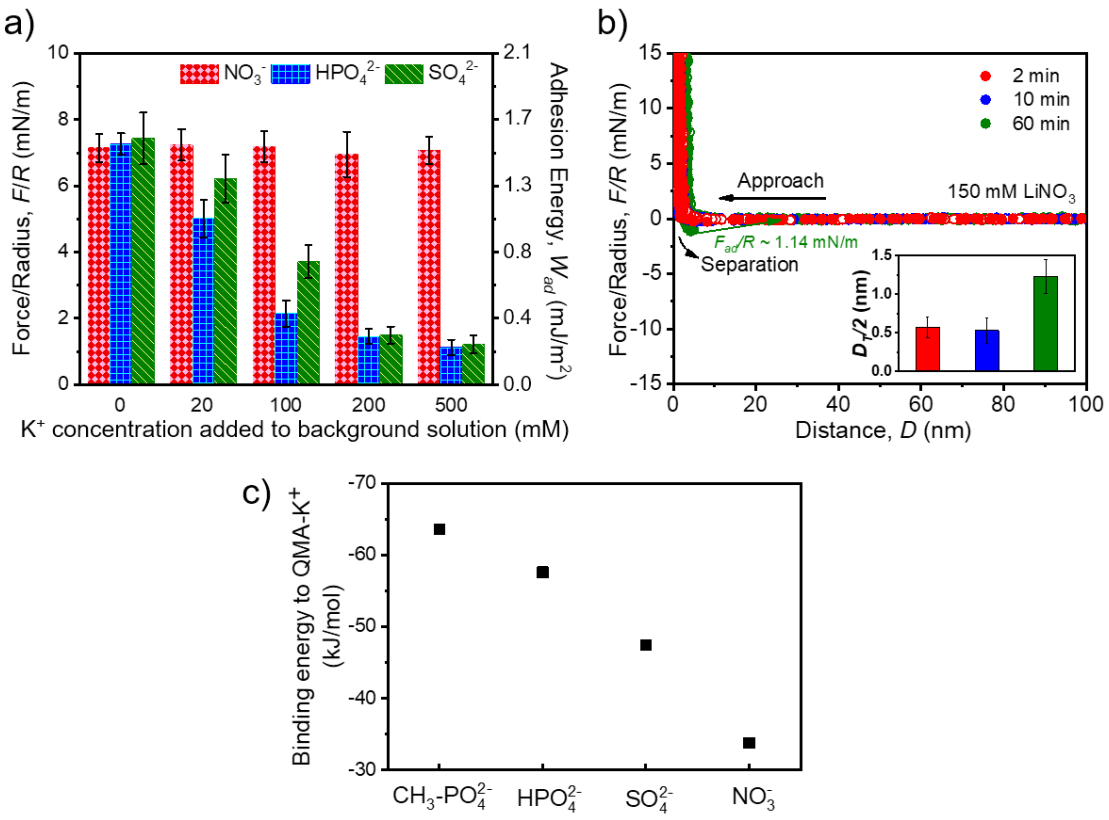

Figure 6.3 a) Adhesion changes between poly(PO_4-DHB) films (1 hr deposition) in 150 mM KNO_3 background buffer solution after further addition of NO_3^-, HPO_4^{2-} or SO_4^{2-}. b) Force-distance profiles and thickness of poly(PO_4-DHB) coatings as a function of *t* in 150 mM $LiNO_3$ buffer solution. c) Binding energies of different anions to methyl amide of π-conjugated quinone (QMA)-K^+ pair in water obtained from DFT simulation.

6.2 Materials and Experimental Methods

6.2.1 Materials and synthesis

2,3-Dihydroxybenzoic acid (2,3-DHBA), benzyl bromide (BnBr), potassium hydroxide (KOH), N,N′-dicyclohexylcarbodiimide (DCC), O-phosphorylethanolamine (O-PEA), Pd/C, dimethyl sulfoxide (DMSO), N-hydroxysuccinimide (NHS), potassium bicarbonate ($KHCO_3$), bicine, tetrahydrofuran (THF), methanol (MeOH) and 1,4-cyclohexadiene

were purchased from Sigma-Aldrich. Methylene chloride (DCM) was purchased from Fisher Scientific, Canada. All chemicals were used as received without further purification.

Synthesis of 2,3-dibenzyloxy-benzoic acid (2,3-2Bn-BA) from 2,3-DHBA

The synthesis was based on a previous report.[1] 2,3-DHBA (2 g) and powdered KOH (10.28 g) were dissolved into DMSO (40 mL). Followed by addition of benzyl bromide (6 mL), the mixture was allowed to react overnight under stirring. Then the product was obtained and purified by extraction (EtOAc) and rotary evaporation. 1H NMR spectrum (*d_6*-DMSO, 400 MHz): δ 7.51-7.09 (m, 13 H; Ph) δ 5.17 (s, 2H; O=CPhOC**H₂**) δ 4.99 (s, 2H; PhOC**H₂**).

Synthesis of 2-O-phosphorylethanol 2,3-dibenzyloxy-benzamide (PO_4-2Bn-B)

The synthesis was performed according to a previously reported method.[2] 2,3-2Bn-BA (2 g) and NHS (0.72 g) was dissolved in 40 mL of THF in a round-bottom flask with ice bath cooling, followed by the dropwise addition of DCC (1.30 g) in THF (10 mL). The reaction was monitored by TLC and the resulted mixture was filtered. The filtrate was concentrated and purified by column chromatography. 1H NMR spectrum (*d_6*-DMSO, 400 MHz) of the resulted product, 2,3-dibenzyloxy-benzoic acid NHS ester (2,3-2Bn-BA-NHS): δ 7.64-7.18 (m, 13H; Ph) δ 5.23 (s, 2H; O=CPhOC**H₂**) δ 5.03 (s, 2H; PhOC**H₂**) δ 2.87 (s, 4H; NO=CC**H₂**). 2.4 g of 2,3-2Bn-BA-NHS was weighed and dissolved in 10 mL THF, and then dropped to a mixture of O-PEA (2.62 g) and $NaHCO_3$ (4.15 g) in 60 mL of 50% aq. THF. The reaction was monitored by TLC. Followed by aqueous work-up (CH_2Cl_2), the product was purified by column chromatography. 1H NMR spectrum (*d_6*-DMSO, 400 MHz): δ 8.30 (t, J=5.7 Hz, 1H; N**H**) δ 7.61-6.98 (m, 13 H; Ph) δ 5.18 (s, 2H; O=CPhOC**H₂**) δ 5.01 (s, 2H; PhOC**H₂**) δ 3.86 (t, J=6.2 Hz, 2H; OC**H₂**CH_2) δ 3.41 (t, J=6.0 Hz, 2H; NHC**H₂**).

Synthesis of 2-O-phosphorylethanol 2,3-hydroxybenzamide (PO_4-DHB)

The removal of benzyl protect group (Bn) was achieved based on a previous report.[3] 700 mg of PO_4-2Bn-B was dissolved in MeOH. Then 700 mg of 10% Pd/C solution in 5 mL of DCM was dropped into the previous mixture, followed by the dropwise addition of 4 mL 1,4-cyclohexadiene under Argon atmosphere. The reaction was allowed to react for 5 hrs. Then the mixture was filtrated and evaporated to obtain the final product. 1H NMR spectrum (d_6-DMSO, 400 MHz): δ 8.97 (t, J=5.4 Hz, 1H; N**H**) δ 7.28-6.67 (m, 3H; Ph) δ 3.95 (t, J=5.8 Hz, 2H; OC**H**$_2$) δ 3.49 (t, J=5.7 Hz, 2H; NHC**H**$_2$).

6.2.2 Experimental method

Surface force measurement using surface forces apparatus

The normal force-distance profiles and adhesion forces of poly(PO_4-DHB) coatings under various aqueous conditions were determined using a surface forces apparatus (SFA) in a configuration reported previously.[4-6] Briefly, two back-silvered mica sheets glued on the cylindrical silica disks (radius R = 2 cm) were mounted in the SFA chamber in a cross-cylinder configuration, which is locally equivalent to a sphere of radius R against a flat surface at a separation distance of $D \ll R$. During the SFA force measurement, D was obtained by monitoring the optical interference fringes of equal chromatic order (FECO) based on the multiple beam interferometry (MBI) optical technique, and the interaction forces were calculated through the deflection of the cantilever spring using Hooke's law. The reference distance ($D_0 = 0$) was determined from an independent measurement of the contact point at which two bare mica surfaces were contacted in air. The adhesion energy per unit area (W_{ad}) was deduced from the measured adhesion force (F_{ad}) based on the Johnson−Kendall−Roberts (JKR) model where $W_{ad}=F_{ad}/1.5\pi R$.[7-8]

For the force measurement during the deposition process, a droplet of 100 μL as-prepared PO_4-DHB buffer solution, with existence of different kinds of salt ions, was injected between two mica surfaces, to study the influence of salt ion types on the interaction behavior and deposition capability. The interaction forces were measured with the variation of deposition time. During a typical force measurement, two surfaces were firstly brought together to reach a "hard wall" and kept in contact for a certain time before the separation. The "hard wall" distance was defined as the formed coating thickness, which did not significantly vary with the increase of normal load. For the force measurement between two as-formed poly(PO_4-DHB) coatings, the coatings were firstly deposited on mica surfaces, and then the two surfaces were transferred to the SFA chamber. The effect of salt species and salt concentrations on the interaction forces was studied by injecting a droplet of 100 μL buffer solution containing different salt ions and salt concentrations between two transferred surfaces followed by the same force measurement method as described above.

Quantum simulation

The density function theory simulation was performed using Gaussian 09 program package.[9] All the calculations were performed at b3lyp/6-311+g(d,p) level with D3BJ dispersion and zero-point vibrational correction, and SMD (water) implicit solvation model was used.[10] For simplicity, the methyl amide of catechol, quinone and *o*-semiquinone radical, denoted as CMA, QMA, QRMA respectively, was used as the model π-conjugated systems, and methyl phosphate was used as the model anionic phosphate ester. The optimized geometries of methyl phosphate ($MePO_4^{2-}$)-CMA/QMA/QRMA-K^+ were obtained. The electrostatic potential (ESP) surfaces of optimized CMA/QMA/QRMA-K^+ pairs, and the binding energies between $MePO_4^{2-}$ and each CMA/QMA/QRMA-K^+ pairs

were computed. The optimized geometries of NO_3^-/HPO_4^{2-}/SO_4^{2-}-QMA-K^+ were also simulated, and the binding energy between NO_3^-/HPO_4^{2-}/SO_4^{2-} and QMA-K^+ pairs were obtained. All the stability of optimized geometry was verified by vibrational analysis. The binding interaction energy was defined as: Binding energy = $E_{complex} - (E_{anion} + E_{pair})$, where $E_{complex}$, E_{anion} and E_{pair} are the total ground state energies of each type of complex, anion and pair in water, respectively.

Time-of-flight secondary ion mass spectrometry (ToF-SIMS) characterization

The composition characterizations of mica and poly(PO_4-DHB) coated mica surfaces were performed by ToF-SIMS analysis in negative-ion mode using an TOF.SIMS 5 instrument (IONTOF GmbH, Münster, Germany) with a 25 keV Bi^+ primary ion source. The primary Bi^+ ion beam was operated at 19 ns with ~1 pA pulsed beam current. The mass anaysis was carried out by using a Time of Flight analyzer and the mass scale was calibrated using H^-, C^-, and O^- peaks. As shown in **Figure S6.2a**), the abundant characteristic ions on mica included C_2H^-, Cl^-, SiO_2^- and SiO_3^-.With the poly(PO_4-DHB) coating on mica surface, as shown in **Figure 6.2b**), the characteristic ion peaks of the poly(PO_4-DHB) coating emerged, including NC^-, NCO^-, PO_2^- and PO_3^-, and the ion intensity ratios of C_2H^-/SiO_2^- and C_2OH^-/SiO_2^- compared with that of bare mica greatly increased from 1.7 to 11.7, and from 0.4 to 2.2, respectively. This characterization results further proved the successful deposition of poly(PO_4-DHB) coating on the mica surface.

X-ray photoelectron spectrometer (XPS) characterization

The XPS C1s spectra of PO_4-DHB and poly(PO_4-DHB) were obtained by using a Kratos Axis 165 XPS spectrophotometer (Kratos Analytical, Manchester, UK). As shown in **Figure S6.12**, compared with PO_4-DHB, in poly(PO_4-DHB), the bond percentage of C-

O/C-N is lower, while the bond percentage of C=O is higher, which should be attributed to the oxidation of a portion of catechol moieties containing C-OH groups to quinone moieties containing C=O groups. As shown in **Figure S6.15a**, according to previous studies, upon exposure to air, catechol in PO_4-DHB would be spontaneously oxidized by oxygen to *o*-semiquinone radical, along with the formation of $O_2^{\cdot-}$. The generated $O_2^{\cdot-}$ would further oxidize another catechol to form *o*-semiquinone radical. The produced two *o*-semiquinone radicals can form quinone and catechol.[11-12] Thus, the transition from *o*-semiquinone radicals to catechol and quinone are reversible, during which the polymerization of PO_4-DHB can be initiated.[11] The oxidation of catechol to quinone is substantiated by XPS characterization. In the following section, the presence of *o*-semiquinone radical would be further verified by using electron paramagnetic spectroscopy (EPR).

Electron paramagnetic spectroscopy (EPR) characterization

As shown in **Figure S6.13**, the EPR spectrum of PO_4-DHB buffer solution (initial concentration of PO_4-DHB: 2 mg/mL, pH 8.4, 50 mM bicine and 150 mM KNO_3) was acquired by using a Bruker Elexys E500 spectrometer (Billerica, MA). The instrument parameters were set as follows: frequency, 9.86 GHz; microwave power, 20 mW; modulation amplitude, 1.0 G; modulation frequency, 100 kHz. The EPR signal peak of the measured free radical is located at ~3314 G with g-value of 2.005, corresponding to typical *o*-semiquinone radical.[13-14]

UV-vis adsorption analysis

The time-dependent UV-vis adsorption spectra of PO_4-DHB (initial concentration: 2 mg/mL) in bicine buffer solution (pH 8.4, 150 mM KNO_3) are shown in **Figure S6.14**. It can be observed that the adsorption of a broad range of wavelength (~380 nm to ~700 nm)

increases with time. The increased adsorption at ~400 nm should be attributed to the oxidation of catechol in PO_4-DHB to quinone.[15-16] The increased adsorption at higher wavelength up to 700 nm should be attributed to the oxidative polymerization due to the occurred *o*-semiquinone radical.[15-16] The broad wavelength adsorption range can be attributed to the complex polymerization routes.[15] Previously, tremendous efforts have been devoted to investigating the oxidative polymerization of catechol and its derivatives, and it is generally accepted that the polymerization route is initiated by the oxidation of catechol to quinone with occurred *o*-semiquinone radical, and the resulted products are consisted of crosslinked catechol and quinone moieties.[11, 17-18] However, due to the versatile and complex chemistry of catechol and its derivatives, their precise polymerization routes and exact chemical structures are still not completely clear.[11, 15] Based on our characterization results and previous studies, the possible polymerization route and structure of poly(PO_4-DHB) are proposed (**Figure S6.15b**).[19-20] Upon spontaneous oxidation, the polymerization of PO_4-DHB between quinone and catechol moieties can be initiated, through C-C bonding between phenyl rings or C-O bonding between phenyl ring and deprotonated hydroxyl group. During the polymerization of PO_4-DHB, the oxidation of catechol to quinone through the intermediate *o*-semiquinone radical can occur simultaneously. Thus, the π-conjugated moieties in the resulted poly(PO_4-DHB) should include crosslinked catechol and quinone moieties, with intermediate *o*-semiquinone radical, which is substantiated by our results based on XPS, EPR and UV-vis characterizations.

6.3 Results and discussion

The important role of phosphate ester in the robust adhesion was further demonstrated through parallel SFA measurements by varying the species and concentrations of competition anions. The adhesion between two as-formed poly(PO_4-DHB) coatings (1 hr deposition) was measured in 150 mM KNO_3 background buffer solution (**Figure 6.3**) as ~7.27 mN/m. To compare the competition effect of different anions, the further added K^+ concentrations were controlled to be ~20, 100, 200 and 500 mM, and the corresponding additional counterions were ~20, 100, 200 and 500 mM of NO_3^-, and ~10, 50, 100 and 250 mM of HPO_4^{2-}/SO_4^{2-}. By increasing concentrations of NO_3^-, the adhesion varied negligibly, suggesting negligible competition capability with phosphate ester groups. For HPO_4^{2-} and SO_4^{2-}, the adhesion with addition of HPO_4^{2-} decreased more dramatically than SO_4^{2-}. The successful competition by HPO_4^{2-} and SO_4^{2-} and decreased adhesion suggest the crucial role of phosphate ester in enhancing adhesion, possibly through forming noncovalent bonding with π-conjugated poly(catechol) moieties. And the binding strength of HPO_4^{2-} to the π-conjugated moieties are stronger than SO_4^{2-}. When the additional concentration of HPO_4^{2-}/SO_4^{2-} ≥ 100 mM, the adhesion almost leveled off and was similar (~1.47 mN/m), which should be due to the much higher concentration of HPO_4^{2-}/SO_4^{2-} compared with phosphate ester groups, thus almost all phosphate ester groups in the binding complex were substituted by HPO_4^{2-}/SO_4^{2-}. When the added HPO_4^{2-}/SO_4^{2-} concentration increased to 250 mM, the further decrease of adhesion was insignificant (~1.17 mN/m).

Because the initial concentration of PO_4-DHB was ~7 mM, and only a fraction would form poly(PO_4-DHB) coatings during deposition, with 10 mM of HPO_4^{2-} in the solution, the amount of HPO_4^{2-} would be much higher than that of the phosphate ester groups on the

coating surface. Yet, the measured adhesion between poly(PO_4-DHB) coatings only decreased by ~31.3%. Therefore, though HPO_4^{2-} could compete with phosphate ester, its binding affinity to the π-conjugated moieties should still be lower than that of phosphate ester. Thus the affinity trend of anions to the π-conjugated moieties in poly(PO_4-DHB) coatings should be: phosphate ester > HPO_4^{2-} > SO_4^{2-} > NO_3^-.

Under the experimental condition (pH 8.4), catechol moieties in PO_4-DHB would undergo spontaneous oxidation to *o*-semiquinone radicals and quinones, then polymerization would be initiated.[23-24] The resulted poly(catechol) is a complex mixture containing crosslinked catechol, quinone and intermediate *o*-semiquinone radical moieties, as electron-rich π systems. [15, 25] The presence of these moieties in poly(PO_4-DHB) was further substantiated by using X-ray photoelectron spectrometer (XPS), electron paramagnetic spectroscopy (EPR) and UV-vis spectroscopy (**Figure S6.12-S6.14**) . The oxidation route and possible chemical structure of poly(PO_4-DHB) are illustrated in **Figure S6.15**. The binary anion-π interaction between electron-rich π system and anion was reported to be weakly attractive or repulsive.[2, 26] However, with a cation (e.g., K^+, Na^+) on the other side of the π system to form cation-π bonding, the formation of anion-π bonding was suggested to be enabled in previous pioneering computational investigations,[26-27] and the interaction in such anion···π···cation orientation was found to be cooperative.[2, 28] To test if the binding strength of anionic phosphate esters to π-conjugated moieties is relevant to cation-π interactions, Li^+ was used as the cation instead of K^+ during film deposition (**Figure 6.3b**), due to the much weaker cation-π interaction performed by Li^+ than K^+.[14] When *t* reached 1 hr, the adhesion in 150 mM $LiNO_3$ buffer solution increased to 1.14 mN/m, significantly lower than that with 150 mM KNO_3. As such, cation-π was proved to

facilitate anionic phosphate ester binding to π-conjugated moieties. Due to abundant Na^+ in seawater, the adhesion of poly(PO_4-DHB) coatings was further investigated during film deposition in 150 mM $NaNO_3$ buffer solution. Strong adhesion was measured (**Figure S6.16a**, ~6.00 mN/m with *t*=1 hr), slightly lower than that with K^+, possibly due to relatively higher desolvation penalty of Na^+ when forming cation-π complex.[14] The adhesion between poly(PO_4-DHB) coatings (1 hr deposition with Na^+) was also greatly undermined with further addition of 250 mM of HPO_4^{2-} in 150 mM $NaNO_3$ background buffer solution (**Figure S6.16b**, ~1.14 mN/m), suggesting cooperative interactions involved similar to that with K^+.

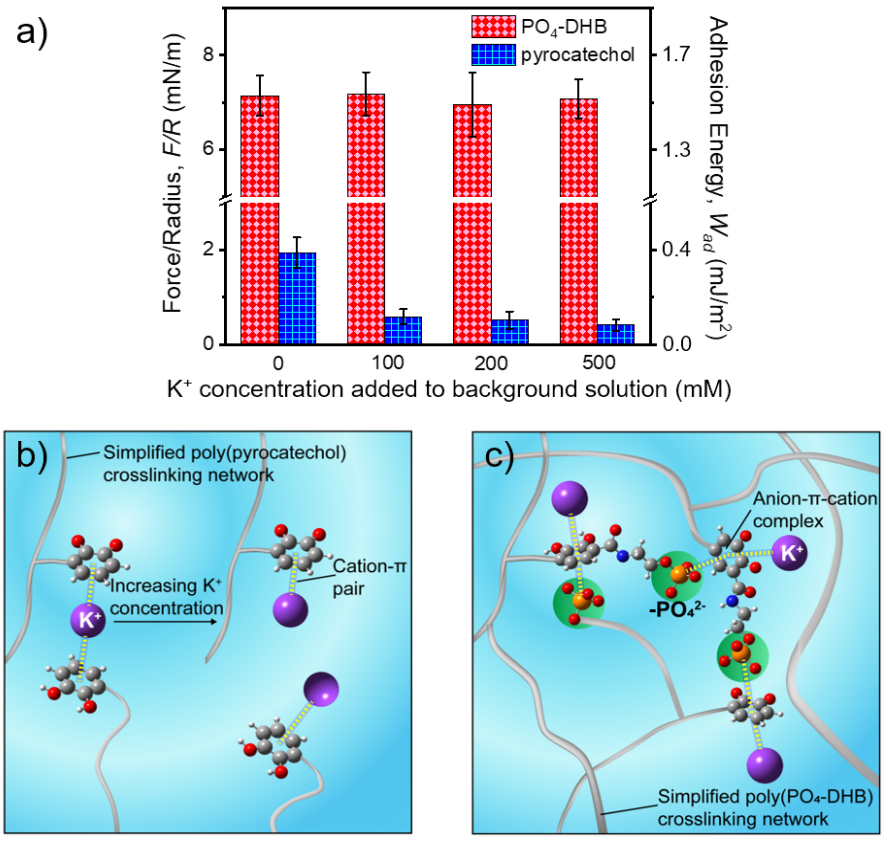

Figure 6.4 a) Adhesion changes obtained from SFA experiments between two poly(PO_4-DHB) or two poly(pyrocatechol) films (1 hr deposition) in 150 mM KNO_3 background

buffer solution with increased additional K^+ concentration. Schematics for b) the abolishment of bridging with increasing concentration of K^+ due to the formation of more cation-π pairs in poly(pyrocatechol) coating and c) the formation of anion-π-cation complex in poly(PO_4-DHB) coating.

Density functional theory (DFT) simulation was performed to better understand the anion-π interaction mechanisms with cooperative cation-π interaction in promoting the adhesion of poly(PO_4-DHB) coatings. Methyl amides of catechol (CMA), quinone (QMA) and *o*-semiquinone radical (QRMA) (**Figure S6.4a**) were used as the electron-rich π-conjugated moieties, and methyl phosphate ($MePO_4^{2-}$) was used as phosphate ester for simplicity.[25, 29] The optimized geometries of $MePO_4^{2-}$-CMA/QMA/QRMA-K^+ complexes (**Figure S6.4b**) are consistent with exemplary anion-π-cation geometries in previous study.[2] $MePO_4^{2-}$ formed stable complexes in all three cases, and the binding strength of $MePO_4^{2-}$ to QMA-K^+ pairs was the strongest (**Table S6.1**), possibly due to more positive electrostatic potential (ESP) on the π-conjugated ring of QMA-K^+ pair (**Figure S6.4c**). Hydrogen bonding interaction also contributed to the binding of $MePO_4^{2-}$, indicated by linear N-H···O and O-H···O configuration.[30] Furthermore, the binding energies of NO_3^-, HPO_4^{2-} and SO_4^{2-} to QMA-K^+ pair was calculated (optimized geometries shown in **Figure S6.5**). The affinity of anions to QMA-K^+ pair followed: $MePO_4^{2-} > HPO_4^{2-} > SO_4^{2-} > NO_3^-$ (**Figure 6.3c**), essentially consistent with SFA experiments. This affinity trend was relevant to charge density, polarity and hydration effect.[31-32] Compared to monovalent NO_3^-, the electrostatic interaction between divalent anions and π-K^+ pair should be much stronger, resulting in higher binding affinity. This finding agreed with the previous study that suggested electrostatic forces as the main contributor to anion-π interaction cooperated

with cation-π interaction.[14, 26] Phosphate ester/$MePO_4^{2-}$ is more hydrophobic than HPO_4^{2-} and SO_4^{2-} with strong hydration shells, thus their binding affinity to the hydrophobic π-conjugated moieties are stronger.[33] As shown in **Figure S6.4b**, the hydrophobic methyl group in $MePO_4^{2-}$ was close to the π-conjugated moieties. HPO_4^{2-} possessed higher polarity than SO_4^{2-}, resulting in more negative ESP on the phosphate group (**Figure S6.6**), hence stronger binding affinity to the positively charged π-K^+ pair.

K^+ concentration effect on the adhesion of poly(PO_4-DHB) coatings (1 hr deposition) was further investigated, with poly(pyrocatechol) coatings as contrast. In both systems cation-π interaction was involved, whereas huge difference was observed (**Figure 6.4a**). With 150 mM KNO_3 background buffer solution, the adhesion between poly(PO_4-DHB) coatings was barely affected by further addition of K^+. While the adhesion of poly(pyrocatechol) coatings was significantly undermined, possibly due to the formation of higher amount of π-K^+ pairs, leading to the abolishment of bridging effect of K^+ between two π-conjugated moieties (**Figure 6.4b**). As to poly(PO_4-DHB) coatings (**Figure 6.4c**), the phosphate ester groups could bridge the π-conjugated moieties with K^+ on the other side, insusceptible to high concentration of K^+. The bridging effect of anion-π interaction showed great promises in resolving the undermined adhesion of binary cationic residues/dopa adhesives due to salt cation competition.

6.4 Conclusions

In summary, for the *first* time, anion-π interaction in aqueous solution and its nanomechanics were directly verified and evaluated through surface force measurements. In the marine bioadhesives-inspired phosphorylated catecholic system, robust and reversible wet-adhesion was detected, and anion-π interaction between anionic phosphate

ester and π-conjugated poly(catechol) moieties was found as the primary contributor. Furthermore, such anion-π interaction was unravelled to be enabled by the cooperative effect of cation-π interaction with the co-existence of cation. The affinity trend of anions to the π-conjugated systems in poly(PO_4-DHB) coating was phosphate ester > HPO_4^{2-} > SO_4^{2-} > NO_3^-, as further substantiated by DFT simulations. The wet-adhesion strength of poly(PO_4-DHB) coatings was not affected by increased concentration of cation (K^+), contrasted with severely undermined adhesion of poly(pyrocatechol). This insusceptible, strong and reversible bridging effect of phosphate ester to the π-cation pairs provides new insights into fundamental adhesion science of marine bioadhesives and shows great implications in biochemical and materials engineering. More broadly, the unravelled nanomechanical insights into the anion-π interaction in aqueous media are significant in understanding biomolecular interactions and rationalizing biomolecule assembly in diverse biological processes such as selective anion binding and protein folding.

6.5 Supporting information

Table S6.1 Binding energies between methyl phosphate and CMA/QMA/QRMA-K^+ pairs.

Name	Binding energy (kJ/mol)
Methyl phosphate/CMA-K^+	-58.67
Methyl phosphate/QMA-K^+	-63.62
Methyl phosphate/QRMA-K^+	-34.92

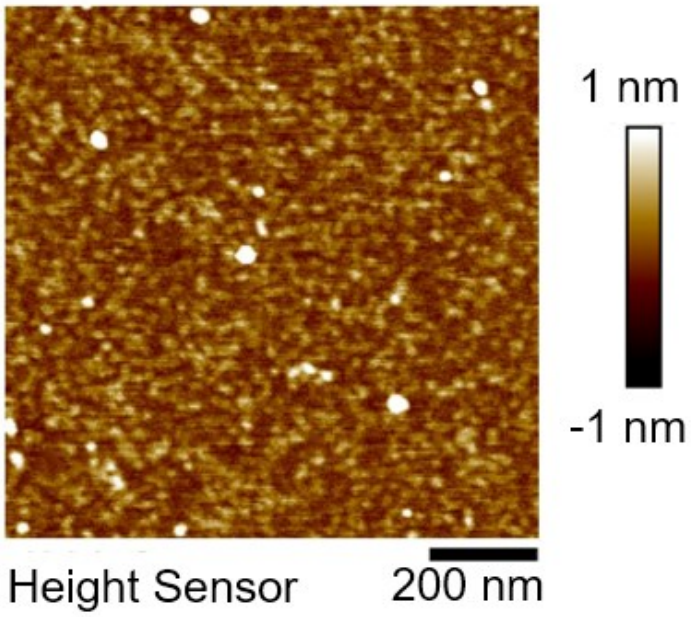

Figure S6.1 Atomic force microscopy (AFM) topographic image of poly(PO_4-DHB) coating.

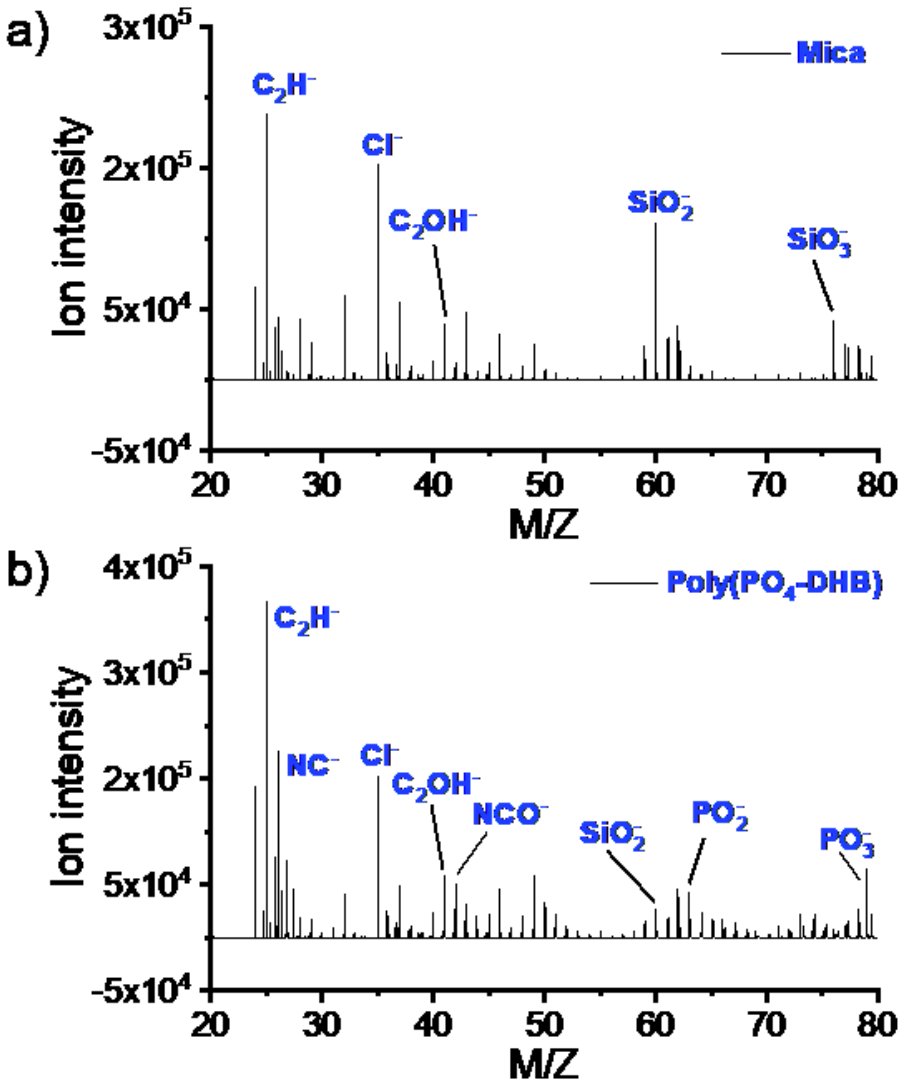

Figure S6.2 Negative time-of-flight secondary ion mass spectrometry (ToF-SIMS) spectra of (a) mica surface and (b) poly(PO_4-DHB) coated mica surface in m/z 20–80.

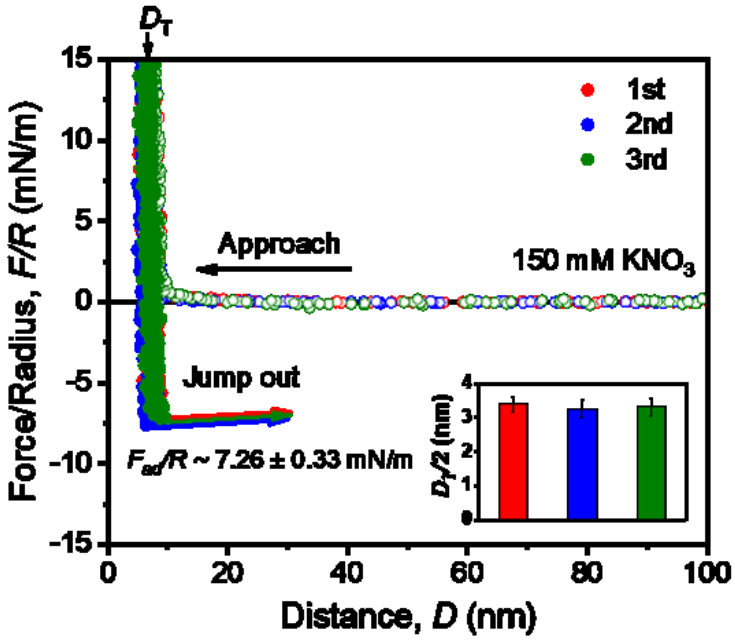

Figure S6.3 Force-distance profiles obtained from three sequential force measurements between two poly(PO_4-DHB) coatings with 1 hr deposition.

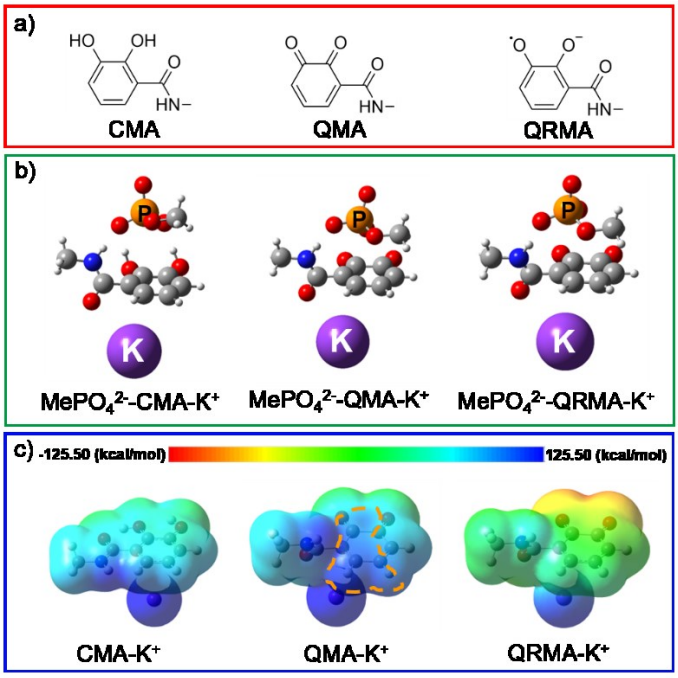

Figure S6.4 a) Chemical structures of methyl amides of catechol (CMA), quinone (QMA) and *o*-semiquinone radical (QRMA). b) Optimized geometries of $MePO_4^{2-}$-CMA/QMA/QRMA-K^+ complexes. The white, grey, red, navy, purple and orange balls stand for hydrogen, carbon, oxygen, nitrogen, potassium and phosphorus atoms, respective. c) Electrostatic potential (ESP) surfaces of CMA/QMA/QRMA-K^+ pairs. Orange circle marks the region with higher positive ESP on the surface of π-conjugated rings.

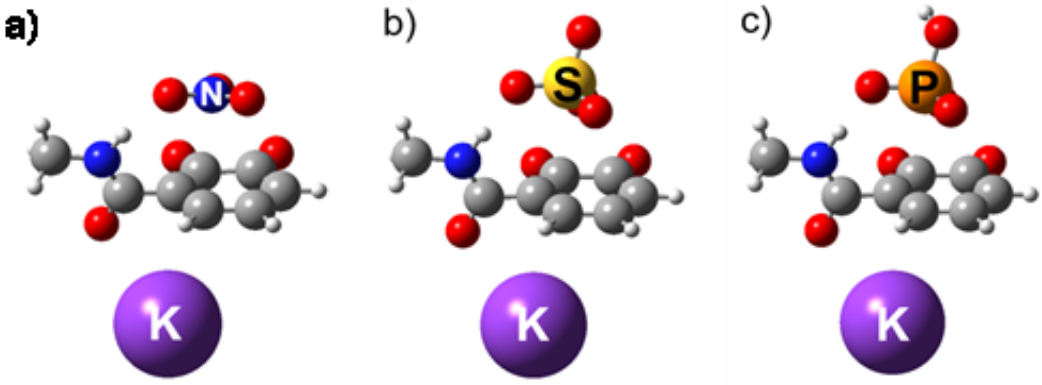

Figure S6.5 Optimized geometries of NO_3^-/SO_4^{2-}/HPO_4^{2-}-QMA-K^+.

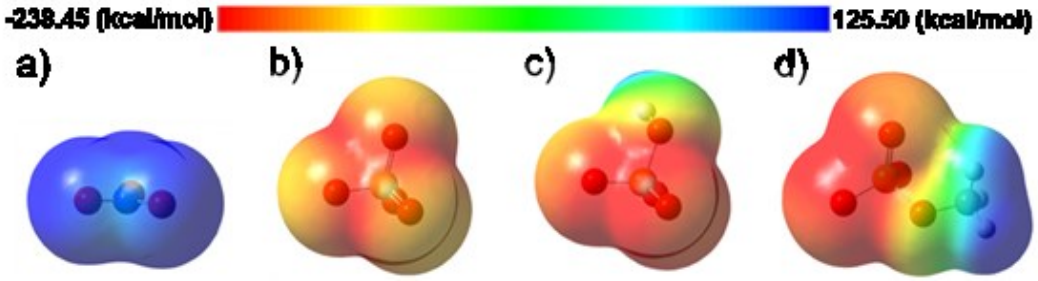

Figure S6.6 ESP surfaces of a) NO_3^-, b) SO_4^{2-}, c) HPO_4^{2-} and d) $MePO_4^{2-}$.

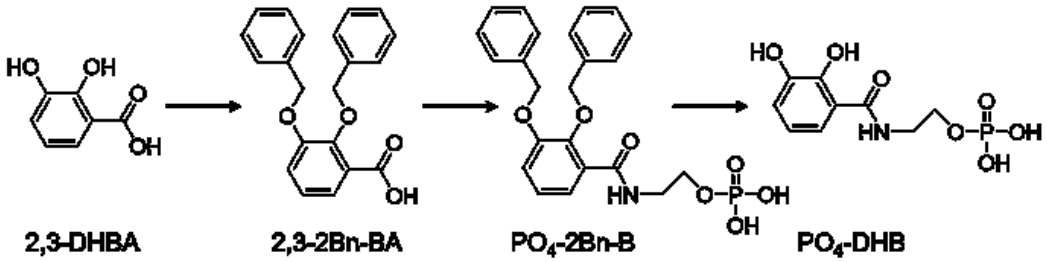

Figure S6.7 Synthesis scheme of PO_4-DHB.

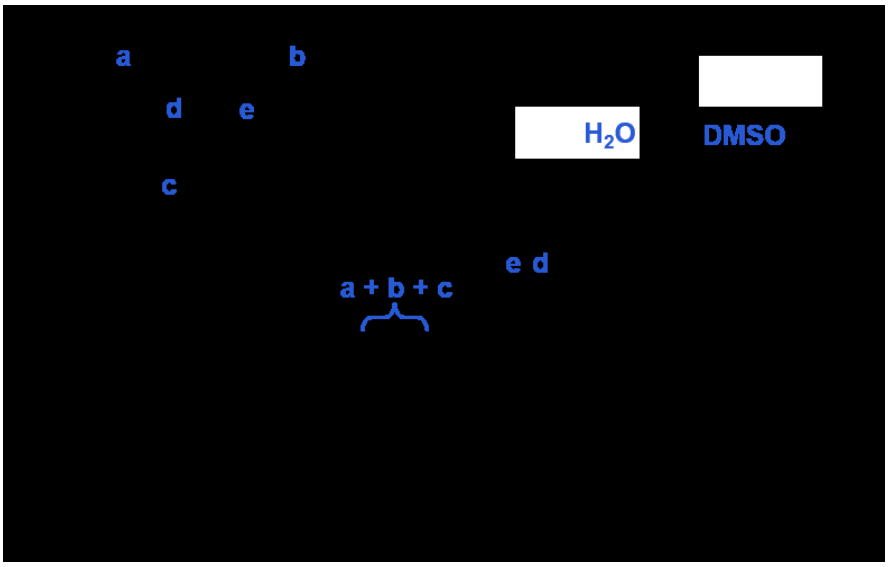

Figure S6.8 1H NMR spectrum of 2,3-dibenzyloxy-benzoic acid (2,3-2Bn-BA).

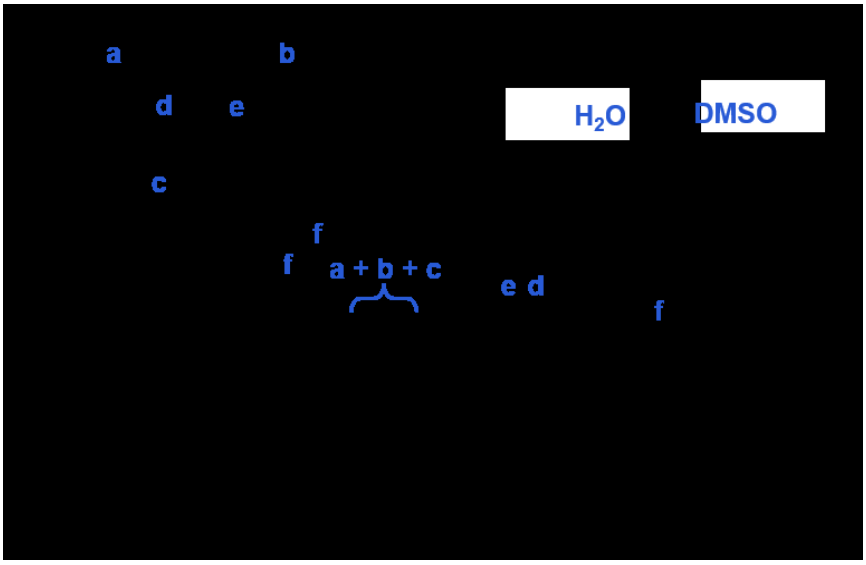

Figure S6.9 1H NMR spectrum of 2,3-dibenzyloxy-benzoic acid NHS ester (2,3-2Bn-BA-NHS).

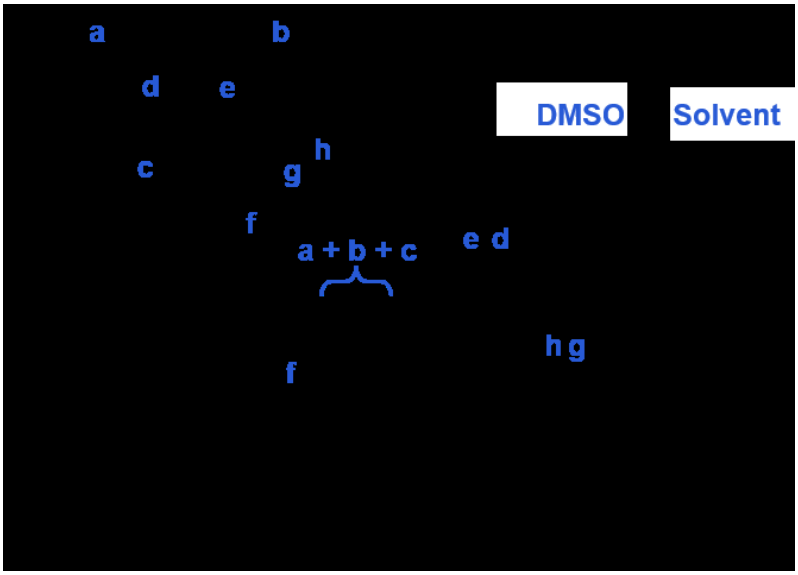

Figure S6.10 1H NMR spectrum of 2-O-phosphorylethanol 2,3-dibenzyloxy-benzamide (PO_4-2Bn-B).

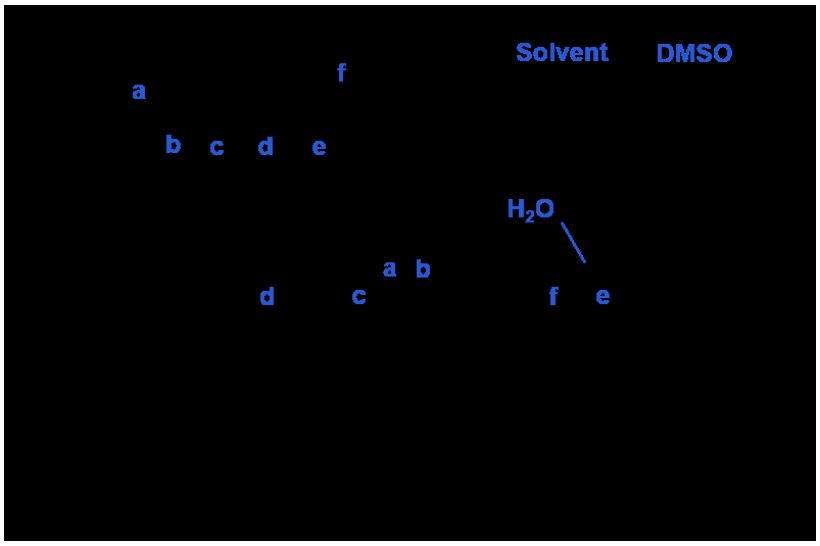

Figure 6.11 1H NMR spectrum of 2-O-phosphorylethanol 2,3-hydroxybenzamide (PO_4-DHB).

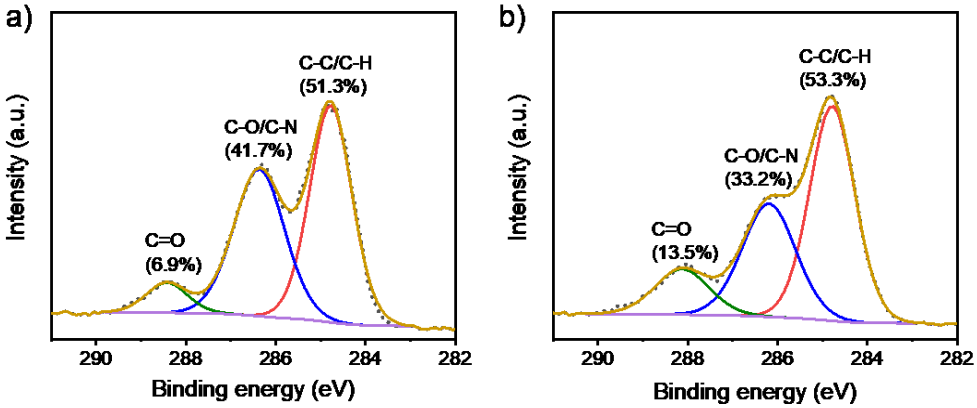

Figure S6.12 X-ray photoelectron spectrometer (XPS) spectra of PO_4-DHB a) before and b) after oxidative polymerization.

Figure S6.13 Electron paramagnetic spectroscopy (EPR) spectrum of PO_4-DHB solution (initial concentration of PO_4-DHB: 2 mg/mL, pH 8.4, 50 mM bicine and 150 mM KNO_3).

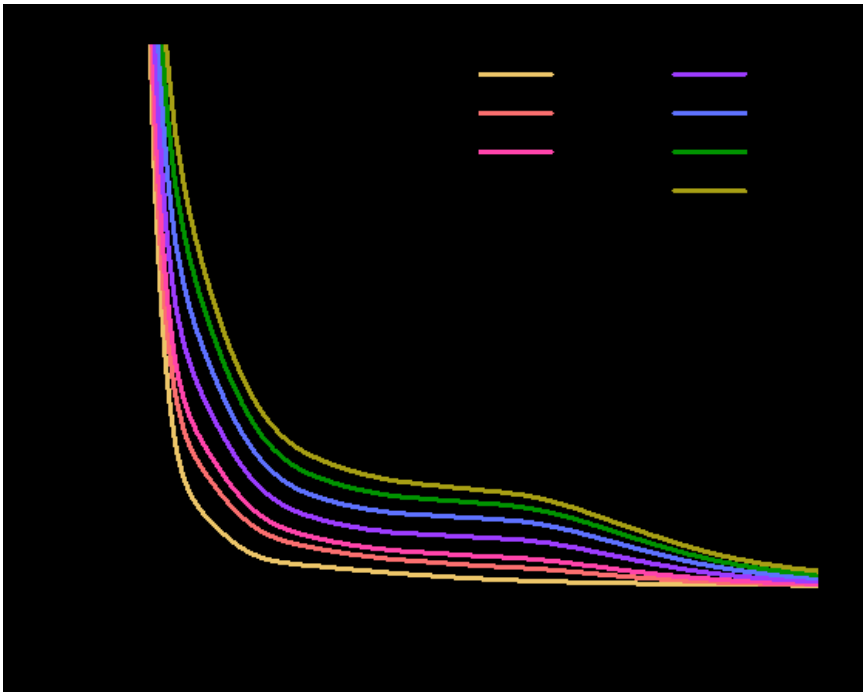

Figure S6.14 Time-dependent UV-vis adsorption spectra of PO_4-DHB (initial concentration: 2 mg/mL) in bicine buffer (pH 8.4, 150 mM KNO_3).

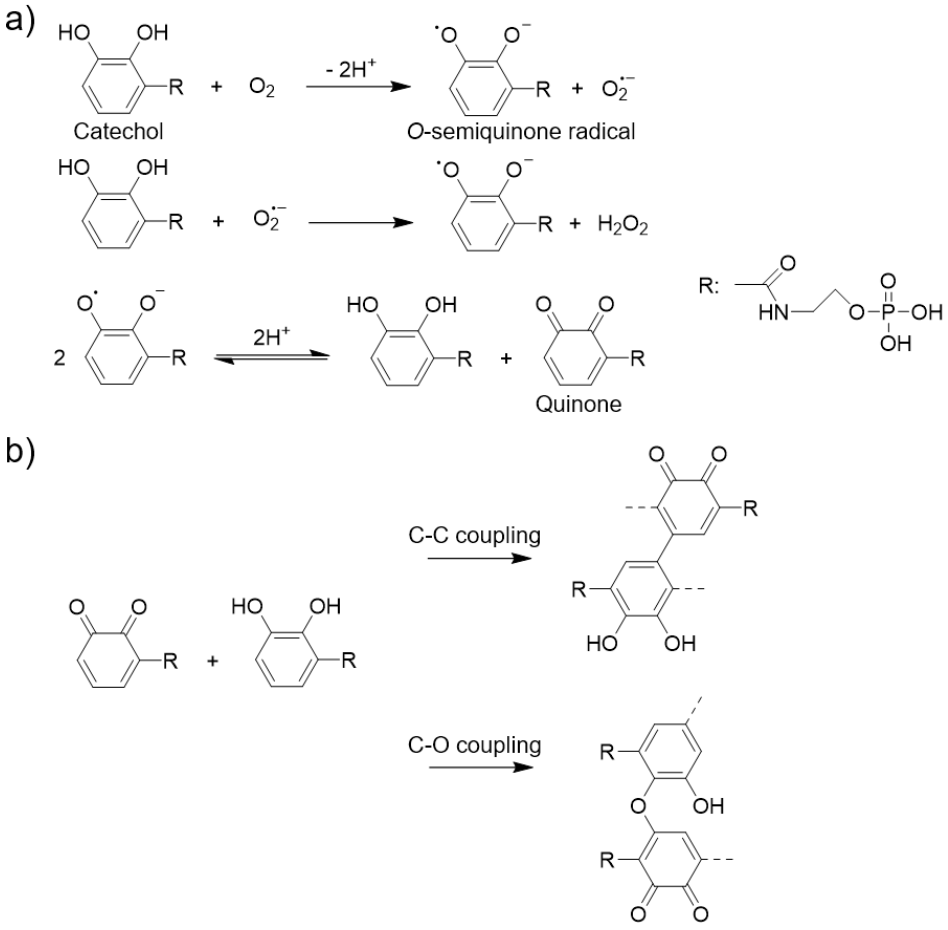

Figure S6.15 a) Oxidation route of catechol in PO_4-DHB to quinone, b) proposed chemical structure of poly(PO_4-DHB).

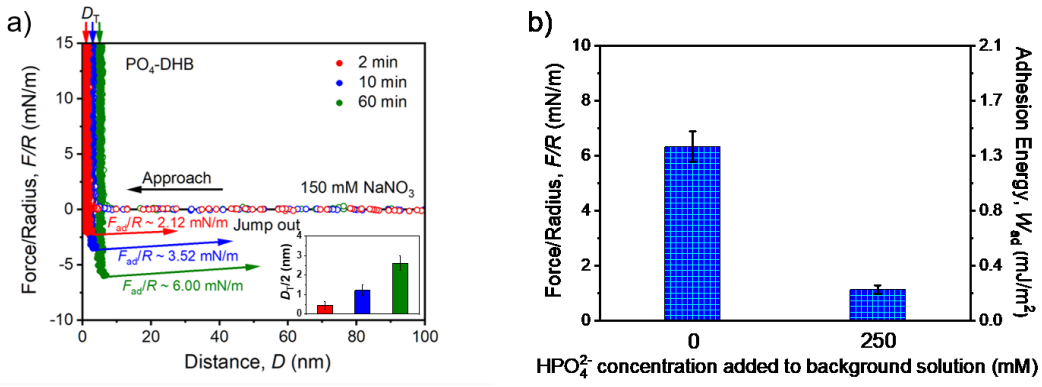

Figure 6.16 a) Force-distance profiles of poly(PO_4-DHB) film as function of deposition time *t* in 150 mM $NaNO_3$ buffer solution (pH 8.4, 50 mM bicine, initial concentration of

PO_4-DHB: 2 mg/mL). The inset shows the thickness of each poly(PO_4-DHB) film (D_T/2). b) Adhesion changes between two poly(PO_4-DHB) films (1 h deposition with 150 mM $NaNO_3$) after further addition of 250 mM HPO_4^- (with the concentration of corresponding counterion Na^+ as 500 mM) in 150 mM $NaNO_3$ background buffer solution.

References

(1) Gebbie, M. A.; Wei, W.; Schrader, A. M.; Cristiani, T. R.; Dobbs, H. A.; Idso, M.; Chmelka, B. F.; Waite, J. H.; Israelachvili, J. N., Tuning underwater adhesion with cation–π interactions. *Nat. Chem.* **2017,** *9* (5), 473.

(2) Lucas, X.; Bauzá, A.; Frontera, A.; Quinonero, D., A thorough anion-π interaction study in biomolecules: on the importance of cooperativity effects. *Chem. Sci.* **2016,** *7* (2), 1038-1050.

(3) Yu, Y.-C.; Berndt, P.; Tirrell, M.; Fields, G. B., Self-assembling amphiphiles for construction of protein molecular architecture. *J. Am. Chem. Soc.* **1996,** *118* (50), 12515-12520.

(4) Mahadevi, A. S.; Sastry, G. N., Cation-π interaction: Its role and relevance in chemistry, biology, and material science. *Chem. Rev.* **2012,** *113* (3), 2100-2138.

(5) Liu, H.; Liu, X.; Meng, J.; Zhang, P.; Yang, G.; Su, B.; Sun, K.; Chen, L.; Han, D.; Wang, S., Hydrophobic interaction-mediated capture and release of cancer cells on thermoresponsive nanostructured surfaces. *Adv. Mater.* **2013,** *25* (6), 922-927.

(6) Mitragotri, S.; Burke, P. A.; Langer, R., Overcoming the challenges in administering biopharmaceuticals: formulation and delivery strategies. *Nat. Rev. Drug Discov.* **2014,** *13* (9), 655.

(7) Knowles, T. P.; Buehler, M. J., Nanomechanics of functional and pathological amyloid materials. *Nat. Nanotechnol.* **2011,** *6* (8), 469.

(8) Qamar, S.; Wang, G.; Randle, S. J.; Ruggeri, F. S.; Varela, J. A.; Lin, J. Q.; Phillips, E. C.; Miyashita, A.; Williams, D.; Ströhl, F., FUS phase separation is modulated by a molecular chaperone and methylation of arginine cation-π interactions. *Cell* **2018,** *173* (3),

720-734. e15.

(9) Neela, Y. I.; Sastry, G. N., Theoretical investigation of anion (F^-, Cl^-) and cation (Na^+) interactions with substituted benzene [$C_6H_{6-n}Y_n$ (Y=-F, -CN, -NO_2; n= 1-6)]. *Mol. Phys.* **2015,** *113* (2), 137-148.

(10) Estarellas, C.; Frontera, A.; Quiñonero, D.; Deyà, P. M., Relevant anion-π interactions in biological systems: The case of urate oxidase. *Angew. Chem. Int. Ed.* **2011,** *50* (2), 415-418.

(11) Lin, Q.; Gourdon, D.; Sun, C.; Holten-Andersen, N.; Anderson, T. H.; Waite, J. H.; Israelachvili, J. N., Adhesion mechanisms of the mussel foot proteins mfp-1 and mfp-3. *Proc. Natl. Acad. Sci. U. S. A.* **2007,** *104* (10), 3782-3786.

(12) Zhang, K.; Zhang, F.; Song, Y.; Fan, J. B.; Wang, S., Recent Progress of Mussel-Inspired Underwater Adhesives. *Chin. J. Chem* . **2017,** *35* (6), 811-820.

(13) Zhao, Y.; Wu, Y.; Wang, L.; Zhang, M.; Chen, X.; Liu, M.; Fan, J.; Liu, J.; Zhou, F.; Wang, Z., Bio-inspired reversible underwater adhesive. *Nat. Commun.* **2017,** *8* (1), 2218.

(14) Lu, Q.; Oh, D. X.; Lee, Y.; Jho, Y.; Hwang, D. S.; Zeng, H., Nanomechanics of cation-π interactions in aqueous solution. *Angew. Chem.* **2013,** *125* (14), 4036-4040.

(15) Lim, C.; Huang, J.; Kim, S.; Lee, H.; Zeng, H.; Hwang, D. S., Nanomechanics of poly(catecholamine) coatings in aqueous solutions. *Angew. Chem. Int. Ed.* **2016,** *55* (10), 3342-3346.

(16) Hofman, A. H.; van Hees, I. A.; Yang, J.; Kamperman, M., Bioinspired underwater adhesives by using the supramolecular toolbox. *Adv. Mater.* **2018,** *30* (19), 1704640.

(17) Stewart, R. J.; Wang, C. S.; Song, I. T.; Jones, J. P., The role of coacervation and phase transitions in the sandcastle worm adhesive system. *Adv. Colloid Interface Sci.* **2017,** *239*,

88-96.

(18) Stewart, R. J.; Ransom, T. C.; Hlady, V., Natural underwater adhesives. *J. Polym. Sci., Part B: Polym. Phys.* **2011,** *49* (11), 757-771.

(19) Lee, B. P.; Messersmith, P. B.; Israelachvili, J. N.; Waite, J. H., Mussel-inspired adhesives and coatings. *Annu. Rev. Mater. Res.* **2011,** *41*, 99-132.

(20) Maeda, N.; Chen, N.; Tirrell, M.; Israelachvili, J. N., Adhesion and friction mechanisms of polymer-on-polymer surfaces. *Science* **2002,** *297* (5580), 379-382.

(21) Zeng, H.; Hwang, D. S.; Israelachvili, J. N.; Waite, J. H., Strong reversible Fe^{3+}-mediated bridging between dopa-containing protein films in water. *Proc. Natl. Acad. Sci. U. S. A.* **2010,** *107* (29), 12850-12853.

(22) Kim, S.; Peterson, A. M.; Holten-Andersen, N., Enhanced Water Retention Maintains Energy Dissipation in Dehydrated Metal-Coordinate Polymer Networks: Another Role for Fe-Catechol Cross-Links? *Chem. Mater.* **2018,** *30* (11), 3648-3655.

(23) Zhang, M.; Peltier, R.; Zhang, M.; Lu, H.; Bian, H.; Li, Y.; Xu, Z.; Shen, Y.; Sun, H.; Wang, Z., In situ reduction of silver nanoparticles on hybrid polydopamine-copper phosphate nanoflowers with enhanced antimicrobial activity. *J. Mater. Chem. B* **2017,** *5* (27), 5311-5317.

(24) Sieste, S.; Mack, T.; Synatschke, C. V.; Schilling, C.; Meyer zu Reckendorf, C.; Pendi, L.; Harvey, S.; Ruggeri, F. S.; Knowles, T. P.; Meier, C., Water-Dispersible Polydopamine-Coated Nanofibers for Stimulation of Neuronal Growth and Adhesion. *Adv. Healthcare Mater.* **2018,** *7* (11), 1701485.

(25) Yang, J.; Stuart, M. A. C.; Kamperman, M., Jack of all trades: versatile catechol crosslinking mechanisms. *Chem. Soc. Rev.* **2014,** *43* (24), 8271-8298.

(26) Kim, D.; Lee, E. C.; Kim, K. S.; Tarakeshwar, P., Cation-π-Anion Interaction: A Theoretical Investigation of the Role of Induction Energies. *J. Phys. Chem. A* **2007,** *111* (32), 7980-7986.

(27) Garau, C.; Quiñonero, D.; Frontera, A.; Ballester, P.; Costa, A.; Deyà, P. M., Anion-π interactions: must the aromatic ring be electron deficient? *New J. Chem.* **2003,** *27* (2), 211-214.

(28) Carrazana-García, J. A.; Rodríguez-Otero, J. s.; Cabaleiro-Lago, E. M., A computational study of anion-modulated cation-π interactions. *J. Phys. Chem. B* **2012,** *116* (20), 5860-5871.

(29) Kalyanaraman, B.; Felix, C.; Sealy, R., Semiquinone anion radicals of catechol(amine)s, catechol estrogens, and their metal ion complexes. *Environ. Health Perspect.* **1985,** *64*, 185-198.

(30) Purushotham, U.; Vijay, D.; Narahari Sastry, G., A computational investigation and the conformational analysis of dimers, anions, cations, and zwitterions of L-phenylalanine. *J. Comput. Chem.* **2012,** *33* (1), 44-59.

(31) Lo Nostro, P.; Ninham, B. W., Hofmeister phenomena: an update on ion specificity in biology. *Chem. Rev.* **2012,** *112* (4), 2286-2322.

(32) Marcus, Y., Ionic radii in aqueous solutions. *Chem. Rev.* **1988,** *88* (8), 1475-1498.

(33) Mason, P.; Neilson, G.; Dempsey, C.; Barnes, A.; Cruickshank, J., The hydration structure of guanidinium and thiocyanate ions: implications for protein stability in aqueous solution. *Proc. Natl. Acad. Sci. U. S. A.* **2003,** *100* (8), 4557-4561.

Chapter 7 Conclusions and Future Work

The research works presented in this thesis aimed at understanding the nanomechanics and related deposition behavior of mussel-inspired functional materials and coatings under various conditions using nanomechanical instruments such as SFA and AFM, which provide useful nanomechanical insights in mussel-inspired interfacial chemistry and material science, with great implications into engineering and bioengineering applications.

The first work was to develop a facile and scalable strategy that held promising potential for developing underwater adhesive materials with surface salt displacement and robust and durable wet adhesion under physiological and seawater environments. Inspired by the mussel-adhesion mechanism and PDA chemistry, we found that integrating primary amine groups located on the adjacent position of catechol groups in PDA via Michael addition reaction through simply introducing amines as functional moieties during dopamine polymerization was an easy-to-implement method to realize strong underwater adhesion with surface salt displacement. Direct SFA force measurement in combination with AFM imaging indicated that the strong adhesive interactions were mainly attributed to the synergetic effect of amine and PDA, in which the displacement/eviction of hydrated salt layer by positively-charged amine groups allowed for the strong adhesion of catechol groups on PDA to the surface, and the cation-π interaction between π-conjugated catechol and protonated amines for the enhancement of cohesion. The major contribution of this work is to propose an readily approach as a candidate for design facile underwater adhesives with bioengineering and marine engineering applications, and the experimental unveiling of the nanomechanics

underlying such adhesion behavior by quantitatively evaluating the adhesion strength and surface morphology of amine/PDA coatings under varies amine species and saline conditions.

The second work aimed at unraveling the impact of mass ratio and surface chemistry on the interaction behavior and deposition capability of phenol/amine coatings. SFA and AFM were utilized to systematically correlate the interaction strength between phenol/amine coatings and between phenol/amine coating and various substrates with the phenol/amine deposition behavior. Introducing amine during phenol deposition could significantly promote the deposition through enhancing the cohesion between amine/phenol moieties. The trend of cohesion strength and deposition capability that first increase and then decrease with increasing the mass ratio of phenol and amine could be attributed to the regulation of the contribution of electrostatic repulsion in overall interactions that involved in the deposition system. The phenol/amine coating exhibited strong adhesion to the substrates with different surface chemistry and wettability, which play a essential role in initiating the phenol/amine deposition on various materials. The surface-independent adhesion behavior could be mainly due to the specific molecular structure and chemical properties of phenol-amine moieties, which enable them to interact with different surfaces through multiple interactions. The major contribution is to provide nanomechanical insight into the interaction mechanism and deposition behavior as well as their correlation during phenol/amine deposition process by quantitatively evaluating the adhesion/cohesion strength and deposition capability of phenol/amine coating. This study offers guidance for engineering advanced phenol/amine-based coating strategy for engineering and bioengineering applications.

The third work mainly focused on exploring the nanomechanics underlying the wet-adhesion and deposition of bio-inspired (i.e., mussel-inspired DOPA chemistry and plant-derived polyphenol deposition) catechol-based adhesives and coatings under physiological fluids and seawater environment. Through directly quantifying the correlation between the interfacial adhesion behavior and deposition properties of pPC in a series of saline aqueous conditions, it was demonstrated that monovalent cations can actively participate in and significantly facilitate the formation of catechol-based coating. The attractive interaction between pPC coatings could be effectively regulated through varying cation concentration and type to realize the modulation of pPC deposition behavior such as pPC assembly and coating thickness. Our major contribution is the experimental identification and successful unraveling of a ternary π-cation–π interaction and its nanomechanics for the first time. Such π-cation–π interaction behavior was found to be closely related to the cation concentration and species, and was demonstrated to be a primary mechanism for the assembly, adhesion and deposition of π-conjugated moieties (e.g., peptides and proteins). This nanomechanical understanding into the ternary π-cation–π interaction enriches the scientific gap of the knowledge on cation–π interaction, more broadly, holds great promise in interpreting a wide range of biological phenomena and activities from biomolecular interaction to biological functions.

The fourth work experimentally verified the existence of anion-π interaction in biological systems, and its nanomechanics was directly investigated through surface force measurements. In the marine bioadhesives-inspired phosphorylated catecholic system, robust and reversible wet-adhesion was detected, and, intriguingly, anion-π interaction between the anionic phosphate ester and π-conjugated poly(catechol) moieties was found to play a major role in the wet-adhesion science. Furthermore, it

was unravelled that such anion-π interaction utilizing electron-rich poly(catechol) moieties as the π systems was enabled by the cooperative effect of cation-π interaction between cations and π moieties, which was substantiated by both SFA force measurements and DFT simulations. With increasing the concentration of cation (K^+), the wet-adhesion strength of poly(PO_4-DHB) was not affected, while in contrast, for poly(pyrocatechol) coatings with the absence of anionic phosphate groups, the wet-adhesion was severely undermined. The affinity trend of the anions to the π-conjugated systems in the as-formed poly(PO_4-DHB) coating was found to be phosphate ester > HPO_4^{2-} > SO_4^{2-} > NO_3^-. This insusceptible, strong and reversible bridging effect of phosphate ester to the π-cation pairs provides new insights into the fundamental adhesion science of marine organism-secreted adhesives and provide new molecular design principles in developing advanced adhesives and coatings in biochemical and materials engineering applications.

In summary, using the nanomechanical instruments SFA and AFM, the interfacial adhesion mechanism and deposition behavior of bio-inspired catechol-based adhesive materials and coatings have been investigated. These results have improved the fundamental understanding of the molecular interaction mechanisms involved in mussel adhesive proteins with valuable insights into designing and developing advanced mussel-inspired adhesives and coatings to meet the requirements in biomedical applications. For instance, preparing smart adhesives with on-demand bonding/debonding transition property in response to external stimuli (*e.g.,* temperature, salinity, pH and light) for removable wound dressing; and fabricating therapeutic adhesives which can not only seal surgical wounds but also offer stimuli-responsive drug release to prevent wound infection or kill residual disease cells. More broadly, the new nanomechanical insights underlying marine mussel adhesion sheds light on

understanding and regulating many biological processes including selective ion binding, protein folding, biological assembly and other biological events involving π-conjugated moieties as well as cationic/anionic species from biomolecular interactions to biological functions. For example, in K^+ channel pore which is rich in multiple aromatic residues, the selective transport of K^+ over Li^+ and Na^+ through K^+ channel and the K^+ channel blocking by tetraethylammonium (containing NMe_4^+) enable the regulation of electrical activity in nerves and muscles. Through varying ion dosage and species, cations and anions may participate and modulate folding/unfolding and inter/intra-chain recognition of numerous biomolecules containing π-conjugated groups (*e.g.,* enzyme) through π-cation-π/anion-π bridging to realize different biological functions such as enzymatic activity.

For the further work, one possible direction is to systematically investigate the effects of extrinsic factors such as salinity, salt species, pH and temperature to fully understand the interfacial interaction mechanism underlying the bio-inspired adhesive coatings in complex aqueous conditions. Another direction is, on the basis of the newly-unraveled interfacial adhesion and deposition mechanisms obtained from this thesis, to develop more advanced functional adhesive materials with stimuli-responsive properties and tuneable composition and structure for different engineering and bioengineering applications.

Bibliography

(1) Maier, G. P.; Rapp, M. V.; Waite, J. H.; Israelachvili, J. N.; Butler, A. *Science* **2015**, *349*, 628-632.

(2) Lee, B. P.; Messersmith, P. B.; Israelachvili, J. N.; Waite, J. H. *Annu. Rev. Mater. Res.* **2011**, *41*, 99-132.

(3) Waite, J. H. *J. Exp. Biol.* **2017**, *220*, 517-530.

(4) Oh, D. X.; Shin, S.; Yoo, H. Y.; Lim, C.; Hwang, D. S. *Korean J. Chem. Eng.* **2014**, *31*, 1306-1315.

(5) Waite, J. H. *Nat. Mater.* **2008**, *7*, 8-9.

(6) Waite, J. H.; Andersen, N. H.; Jewhurst, S.; Sun, C. *J. Adhes.* **2005**, *81*, 297-317.

(7) Kavouras, J. H.; Maki, J. S. *Invertebr. Biol.* **2003**, *122*, 138-151.

(8) Aldred, N.; Ista, L.; Callow, M.; Callow, J.; Lopez, G.; Clare, A. *J. Royal Soc. Interface* **2006**, *3*, 37-43.

(9) Crisp, D.; Walker, G.; Young, G.; Yule, A. *J. Colloid Interface Sci.* **1985**, *104*, 40-50.

(10) Haris, V.; Springer Science & Business Media, 1990.

(11) Waite, J. H. *Int. J. Adhes. Adhes.* **1987**, *7*, 9-14.

(12) Waite, J. H. In *Book*; Springer, 1992; pp 27-54.

(13) Waite, J. H.; Qin, X.-X.; Coyne, K. J. *Matrix Biol.* **1998**, *17*, 93-106.

(14) Lowy, J.; Millman, B. *Philos. Trans. R. Soc. Lond. B. Biol. Sci.* **1963**, *246*, 105-148.

(15) Hwang, D. S.; Zeng, H.; Masic, A.; Harrington, M. J.; Israelachvili, J. N.; Waite, J. H. *J. Biol. Chem.* **2010**, *285*, 25850-25858.

(16) Holten-Andersen, N.; Fantner, G. E.; Hohlbauch, S.; Waite, J. H.; Zok, F. W. *Nat.*

Mater. **2007**, *6*, 669-672.

(17) Qin, X.; Waite, J. H. *J. Exp. Biol.* **1995**, *198*, 633-644.

(18) Filpula, D. R.; Lee, S. M.; Link, R. P.; Strausberg, S. L.; Strausberg, R. L. *Biotechnol. Prog.* **1990**, *6*, 171-177.

(19) Taylor, S. W.; Waite, J. H.; Ross, M. M.; Shabanowitz, J.; Hunt, D. F. *J. Am. Chem. Soc.* **1994**, *116*, 10803-10804.

(20) Waite, J. H. *J. Biol. Chem.* **1983**, *258*, 2911-2915.

(21) Rzepecki, L. M.; Hansen, K. M.; Waite, J. H. *The Biological Bulletin* **1992**, *183*, 123-137.

(22) Inoue, K.; Takeuchi, Y.; Miki, D.; Odo, S. *J. Biol. Chem.* **1995**, *270*, 6698-6701.

(23) Burzio, L. A.; Waite, J. H. *Biochemistry* **2000**, *39*, 11147-11153.

(24) Even, M. A.; Wang, J.; Chen, Z. *Langmuir* **2008**, *24*, 5795-5801.

(25) Zhao, H.; Waite, J. H. *Biochemistry* **2006**, *45*, 14223-14231.

(26) Waite, J. H.; Qin, X. *Biochemistry* **2001**, *40*, 2887-2893.

(27) Zhao, H.; Waite, J. H. *J. Biol. Chem.* **2006**, *281*, 26150-26158.

(28) Yu, J.; Wei, W.; Danner, E.; Ashley, R. K.; Israelachvili, J. N.; Waite, J. H. *Nat. Chem. Biol.* **2011**, *7*, 588-590.

(29) Yu, J.; Springer, 2014.

(30) Yu, M.; Hwang, J.; Deming, T. J. *J. Am. Chem. Soc.* **1999**, *121*, 5825-5826.

(31) Lee, H. *Proc. Natl. Acad. Sci. USA* **2006**, *103*, 12999-13003.

(32) Bandara, N.; Zeng, H.; Wu, J. *J. Adhes. Sci. Technol.* **2013**, *27*, 2139-2162.

(33) Ahn, B. K.; Lee, D. W.; Israelachvili, J. N.; Waite, J. H. *Nat. Mater.* **2014**, *13*, 867-872.

(34) Lu, Q.; Danner, E.; Waite, J. H.; Israelachvili, J. N.; Zeng, H.; Hwang, D. S. *J. Royal Soc. Interface* **2013**, *10*, 20120759.

(35) Zeng, H.; Hwang, D. S.; Israelachvili, J. N.; Waite, J. H. *Proc. Natl. Acad. Sci. U.S.A.* **2010**, *107*, 12850-12853.

(36) Kan, Y.; Danner, E. W.; Israelachvili, J. N.; Chen, Y.; Waite, J. H. *PLoS ONE* **2014**, *9*.

(37) Fant, C.; Sott, K.; Elwing, H.; Hook, F. *Biofouling* **2000**, *16*, 119-132.

(38) Krogsgaard, M.; Nue, V.; Birkedal, H. *Chem. Eur. J.* **2016**, *22*, 844-857.

(39) Kim, S.; Yoo, H. Y.; Huang, J.; Lee, Y.; Park, S.; Park, Y.; Jin, S.; Jung, Y. M.; Zeng, H.; Hwang, D. S. *ACS nano* **2017**, *11*, 6764-6772.

(40) Kord Forooshani, P.; Lee, B. P. *J. Polym. Sci., Part A: Polym. Chem.* **2017**, *55*, 9-33.

(41) Li, J.; Celiz, A.; Yang, J.; Yang, Q.; Wamala, I.; Whyte, W.; Seo, B.; Vasilyev, N.; Vlassak, J.; Suo, Z. *Science* **2017**, *357*, 378-381.

(42) Brault, N. D.; Gao, C.; Xue, H.; Piliarik, M.; Homola, J.; Jiang, S.; Yu, Q. *Biosens. Bioelectron.* **2010**, *25*, 2276-2282.

(43) Kao, C.-T.; Lin, C.-C.; Chen, Y.-W.; Yeh, C.-H.; Fang, H.-Y.; Shie, M.-Y. *Mater. Sci. Eng. C* **2015**, *56*, 165-173.

(44) Lee, L.-H. In *Book*; Springer, 1988; pp 5-29.

(45) Dalsin, J. L.; Messersmith, P. B. *Mater. Today* **2005**, *8*, 38-46.

(46) Gao, C.; Li, G.; Xue, H.; Yang, W.; Zhang, F.; Jiang, S. *Biomaterials* **2010**, *31*, 1486-1492.

(47) Lee, H.; Dellatore, S. M.; Miller, W. M.; Messersmith, P. B. *Science* **2007**, *318*, 426-430.

(48) Han, H.; Wu, J.; Avery, C. W.; Mizutani, M.; Jiang, X.; Kamigaito, M.; Chen, Z.; Xi, C.; Kuroda, K. *Langmuir* **2011**, *27*, 4010-4019.

(49) Kang, S. M.; You, I.; Cho, W. K.; Shon, H. K.; Lee, T. G.; Choi, I. S.; Karp, J. M.;

Lee, H. *Angew. Chem., Int. Ed.* **2010**, *49*, 9401-9404.

(50) Liu, J.; Li, J.; Yu, B.; Ma, B.; Zhu, Y.; Song, X.; Cao, X.; Yang, W.; Zhou, F. *Langmuir* **2011**, *27*, 11324-11331.

(51) Wei, Q.; Pei, X.; Hao, J.; Cai, M.; Zhou, F.; Liu, W. *Adv. Mater. Interfaces.* **2014**, *1*, 1400035.

(52) Wach, J. Y.; Malisova, B.; Bonazzi, S.; Tosatti, S.; Textor, M.; Zürcher, S.; Gademann, K. *Chem. Eur. J.* **2008**, *14*, 10579-10584.

(53) Edmondson, S.; Osborne, V. L.; Huck, W. T. *Chem. Soc. Rev.* **2004**, *33*, 14-22.

(54) Min, Y. **2011**.

(55) Ho, C.-C.; Ding, S.-J. *J. Biomed. Nanotechnol.* **2014**, *10*, 3063-3084.

(56) Liu, Y.; Ai, K.; Lu, L. *Chem. Rev.* **2014**, *114*, 5057-5115.

(57) Yang, H.-C.; Luo, J.; Lv, Y.; Shen, P.; Xu, Z.-K. *J. Membr. Sci.* **2015**, *483*, 42-59.

(58) Jeon, E. K.; Seo, E.; Lee, E.; Lee, W.; Um, M.-K.; Kim, B.-S. *Chem. Commun.* **2013**, *49*, 3392-3394.

(59) Zhang, C.; Yang, H.-C.; Wan, L.-S.; Liang, H.-Q.; Li, H.; Xu, Z.-K. *ACS Appl. Mater. Interfaces* **2015**, *7*, 11567-11574.

(60) Choi, B.-H.; Choi, Y. S.; Hwang, D. S.; Cha, H. J. *Tissue Eng. Part C: Methods* **2012**, *18*, 71-79.

(61) Ham, H. O.; Liu, Z.; Lau, K. A.; Lee, H.; Messersmith, P. B. *Angew. Chem., Int. Ed.* **2011**, *50*, 732-736.

(62) Lee, H.; Rho, J.; Messersmith, P. B. *Adv. Mater.* **2009**, *21*, 431-434.

(63) Pashley, R. *Adv. Colloid Interface Sci.* **1982**, *16*, 57-62.

(64) Israelachvili, J.; Wennerström, H. *Nature* **1996**, *379*, 219-225.

(65) Rapp, M. V.; Maier, G. P.; Dobbs, H. A.; Higdon, N. J.; Waite, J. H.; Butler, A.; Israelachvili, J. N. *J. Am. Chem. Soc.* **2016**, *138*, 9013-9016.

(66) North, M. A.; Del Grosso, C. A.; Wilker, J. J. *ACS Appl. Mater. Interfaces* **2017**, *9*, 7866-7872.

(67) Wang, R.; Li, J.; Chen, W.; Xu, T.; Yun, S.; Xu, Z.; Xu, Z.; Sato, T.; Chi, B.; Xu, H. *Adv. Funct. Mater.* **2017**, *27*, 1604894.

(68) Zhao, Y.; Wu, Y.; Wang, L.; Zhang, M.; Chen, X.; Liu, M.; Fan, J.; Liu, J.; Zhou, F.; Wang, Z. *Nat. Commun.* **2017**, *8*, 1-8.

(69) Yu, J. In *Book*; Springer, 2014; pp 21-30.

(70) Li, L.; Zeng, H. *Biotribology* **2016**, *5*, 44-51.

(71) Park, S.; Kim, S.; Jho, Y.; Hwang, D. S. *Langmuir* **2019**, *35*, 16002-16012.

(72) Gebbie, M. A.; Wei, W.; Schrader, A. M.; Cristiani, T. R.; Dobbs, H. A.; Idso, M.; Chmelka, B. F.; Waite, J. H.; Israelachvili, J. N. *Nat. Chem.* **2017**, *9*, 473-479.

(73) Yang, B.; Jin, S.; Park, Y.; Jung, Y. M.; Cha, H. J. *Small* **2018**, *14*, 1803377.

(74) Degen, G. D.; Stow, P. R.; Lewis, R. B.; Andresen Eguiluz, R. C.; Valois, E.; Kristiansen, K.; Butler, A.; Israelachvili, J. N. *J. Am. Chem. Soc.* **2019**, *141*, 18673-18681.

(75) Lim, C.; Huang, J.; Kim, S.; Lee, H.; Zeng, H.; Hwang, D. S. *Angew. Chem., Int. Ed.* **2016**, *55*, 3342-3346.

(76) Tabor, D.; Winterton, R. *Proc. R. Soc. A-Math. Phy.* **1969**, *312*, 435-450.

(77) Israelachvili, J.; Tabor, D. *Wear* **1973**, *24*, 386-390.

(78) Israelachvili, J.; Tabor, D. *Nat. Phys. Sci.* **1972**, *236*, 106.

(79) Israelachvili, J.; Adams, G. *Nature* **1976**, *262*, 774-776.

(80) Israelachvili, J. N.; McGuiggan, P. M. *J. Mater. Res.* **1990**, *5*, 2223-2231.

(81) Israelachvili, J.; Min, Y.; Akbulut, M.; Alig, A.; Carver, G.; Greene, W.; Kristiansen, K.; Meyer, E.; Pesika, N.; Rosenberg, K. *Rep. Prog. Phys.* **2010**, *73*, 036601.

(82) Horn, R.; Israelachvili, J.; Pribac, F. *J. Colloid Interface Sci.* **1987**, *115*, 480-492.

(83) Klein, J. *J. Chem. Soc., Faraday Trans.* **1983**, *79*, 99-118.

(84) Israelachvili, J. N.; Academic press, 2011.

(85) Israelachvili, J.; Min, Y.; Akbulut, M.; Alig, A.; Carver, G.; Greene, W.; Kristiansen, K.; Meyer, E.; Pesika, N.; Rosenberg, K.; Zeng, H. *Rep Prog Phys* **2010**, *73*.

(86) Zeng, H.; Tian, Y.; Anderson, T. H.; Tirrell, M.; Israelachvili, J. N. *Langmuir* **2008**, *24*, 1173-1182.

(87) Teng, F. C.; Zeng, H. B.; Liu, Q. X. *J Phys Chem C* **2011**, *115*, 17485-17494.

(88) Natarajan, A.; Xie, J. G.; Wang, S. Q.; Liu, Q. X.; Masliyah, J.; Zeng, H. B.; Xu, Z. H. *J Phys Chem C* **2011**, *115*, 16043-16051.

(89) Natarajan, A.; Kuznicki, N.; Harbottle, D.; Masliyah, J.; Zeng, H. B.; Xu, Z. H. *Langmuir* **2014**, *30*, 9370-9377.

(90) Gong, L.; Xiang, L.; Zhang, J.; Chen, J.; Zeng, H. *Langmuir* **2019**, *35*, 15914-15936.

(91) Israelachvili, J. N.; Academic press, 2015.

(92) Israelac.Jn. *J Colloid Interf. Sci.* **1973**, *44*, 259-272.

(93) Israelachvili, J. *J Colloid Interf. Sci.* **1973**, *44*, 259-272.

(94) Faure, E.; Falentin-Daudré, C.; Jérôme, C.; Lyskawa, J.; Fournier, D.; Woisel, P.; Detrembleur, C. *Prog. Polym. Sci.* **2013**, *38*, 236-270.

(95) Tay, F. R.; Pashley, D. H. *J. Dent.* **2003**, *16*, 6-12.

(96) Zhang, C.; Li, H.-N.; Du, Y.; Ma, M.-Q.; Xu, Z.-K. *Langmuir* **2017**, *33*, 1210-1216.

(97) Zhang, C.; Ou, Y.; Lei, W. X.; Wan, L. S.; Ji, J.; Xu, Z. K. *Angew. Chem., Int. Ed.* **2016**, *55*, 3054-3057.

(98) Guo, Z.; Zhou, F.; Hao, J.; Liu, W. *J. Am. Chem. Soc.* **2005**, *127*, 15670-15671.

(99) Schmidt, T. A.; Gastelum, N. S.; Nguyen, Q. T.; Schumacher, B. L.; Sah, R. L. *Arthritis & Rheumatism* **2007**, *56*, 882-891.

(100) Wei, Q.; Zhang, F.; Li, J.; Li, B.; Zhao, C. *Poly. Chem.* **2010**, *1*, 1430-1433.

(101) Hwang, D. S.; Sim, S. B.; Cha, H. J. *Biomaterials* **2007**, *28*, 4039-4046.

(102) Ahn, B. K. *J. Am. Chem. Soc.* **2017**, *139*, 10166-10171.

(103) Lin, Q.; Gourdon, D.; Sun, C.; Holten-Andersen, N.; Anderson, T. H.; Waite, J. H.; Israelachvili, J. N. *Proc. Natl. Acad. Sci. U.S.A.* **2007**, *104*, 3782-3786.

(104) Han, L.; Gong, L.; Chen, J.; Zhang, J.; Xiang, L.; Zhang, L.; Wang, Q.; Yan, B.; Zeng, H. *ACS Appl. Mater. Interfaces* **2018**, *10*, 2166-2173.

(105) Li, Y.; Wang, T.; Xia, L.; Wang, L.; Qin, M.; Li, Y.; Wang, W.; Cao, Y. *J. Mater. Chem. B* **2017**, *5*, 4416-4420.

(106) Sen, R.; Gahtory, D.; Carvalho, R. R.; Albada, B.; van Delft, F. L.; Zuilhof, H. *Angew. Chem.* **2017**, *129*, 4194-4198.

(107) Yu, J.; Wei, W.; Danner, E.; Israelachvili, J. N.; Waite, J. H. *Adv. Mater.* **2011**, *23*, 2362-2366.

(108) Liu, M.; Zeng, G.; Wang, K.; Wan, Q.; Tao, L.; Zhang, X.; Wei, Y. *Nanoscale* **2016**, *8*, 16819-16840.

(109) Zhang, X.; Huang, Q.; Deng, F.; Huang, H.; Wan, Q.; Liu, M.; Wei, Y. *Appl. Mater. Today* **2017**, *7*, 222-238.

(110) Zhang, X.; Wang, S.; Xu, L.; Feng, L.; Ji, Y.; Tao, L.; Li, S.; Wei, Y. *Nanoscale* **2012**, *4*, 5581-5584.

(111) Li, L.; Yan, B.; Zhang, L.; Tian, Y.; Zeng, H. *Chem. Commun.* **2015**, *51*, 15780-15783.

(112) Lu, Q.; Oh, D. X.; Lee, Y.; Jho, Y.; Hwang, D. S.; Zeng, H. *Angew. Chem.,* **2013**, *125*, 4036-4040.

(113) Johnson, K. L.; Kendall, K.; Roberts, A. *Proc. Royal Soc. Lond.* **1971**, *324*, 301-313.

(114) Zeng, H.; Tian, Y.; Zhao, B.; Tirrell, M.; Israelachvili, J. *Macromolecules* **2007**, *40*, 8409-8422.

(115) Yang, H.-C.; Liao, K.-J.; Huang, H.; Wu, Q.-Y.; Wan, L.-S.; Xu, Z.-K. *J. Mater. Chem. A* **2014**, *2*, 10225-10230.

(116) Jin, L.; Liu, J.; Tang, Y.; Cao, L.; Zhang, T.; Yuan, Q.; Wang, Y.; Zhang, H. *ACS Appl. Mater. Interfaces* **2017**, *9*, 41648-41658.

(117) Zhang, C.; Lv, Y.; Qiu, W.-Z.; He, A.; Xu, Z.-K. *ACS Appl. Mater. Interfaces* **2017**, *9*, 14437-14444.

(118) Hwang, D. S.; Harrington, M. J.; Lu, Q.; Masic, A.; Zeng, H.; Waite, J. H. *J. Mater. Chem.* **2012**, *22*, 15530-15533.

(119) Yu, J.; Wei, W.; Menyo, M. S.; Masic, A.; Waite, J. H.; Israelachvili, J. N. *Biomacromolecules* **2013**, *14*, 1072-1077.

(120) Liu, M.; Ji, J.; Zhang, X.; Zhang, X.; Yang, B.; Deng, F.; Li, Z.; Wang, K.; Yang, Y.; Wei, Y. *J. Mater. Chem. B* **2015**, *3*, 3476-3482.

(121) Zhang, X.; Huang, Q.; Liu, M.; Tian, J.; Zeng, G.; Li, Z.; Wang, K.; Zhang, Q.; Wan, Q.; Deng, F. *Appl. Surf. Sci.* **2015**, *343*, 19-27.

(122) Hwang, D. S.; Zeng, H.; Lu, Q.; Israelachvili, J.; Waite, J. H. *Soft Matter* **2012**, *8*, 5640-5648.

(123) Kim, S.; Faghihnejad, A.; Lee, Y.; Jho, Y.; Zeng, H.; Hwang, D. S. *J. Mater. Chem. B* **2015**, *3*, 738-743.

(124) Kim, S.; Huang, J.; Lee, Y.; Dutta, S.; Yoo, H. Y.; Jung, Y. M.; Jho, Y.; Zeng, H.; Hwang, D. S. *Proc. Natl. Acad. Sci.* **2016**, *113*, E847-E853.

(125) Shao, H.; Stewart, R. J. *Adv. Mater.* **2010**, *22*, 729-733.

(126) Haemers, S.; Koper, G. J.; Frens, G. *Biomacromolecules* **2003**, *4*, 632-640.

(127) Zhao, Q.; Lee, D. W.; Ahn, B. K.; Seo, S.; Kaufman, Y.; Israelachvili, J. N.;

Waite, J. H. *Nat. Mater.* **2016**, *15*, 407.

(128) Lv, Y.; Yang, H.-C.; Liang, H.-Q.; Wan, L.-S.; Xu, Z.-K. *J. Membr. Sci.* **2015**, *476*, 50-58.

(129) Adamcik, J.; Lara, C.; Usov, I.; Jeong, J. S.; Ruggeri, F. S.; Dietler, G.; Lashuel, H. A.; Hamley, I. W.; Mezzenga, R. *Nanoscale* **2012**, *4*, 4426-4429.

(130) Oral, I.; Guzel, H.; Ahmetli, G. *Polymer bulletin* **2011**, *67*, 1893-1906.

(131) Lin, A. S.; Barrows, T. H.; Cartmell, S. H.; Guldberg, R. E. *Biomaterials* **2003**, *24*, 481-489.

(132) Kord Forooshani, P.; Lee, B. P. *J. Polym. Sci. A* **2017**, *55*, 9-33.

(133) Xu, H.; Liu, X.; Su, G.; Zhang, B.; Wang, D. *Langmuir* **2012**, *28*, 13060-13065.

(134) Lim, M.-Y.; Shin, H.; Shin, D. M.; Lee, S.-S.; Lee, J.-C. *Polymer* **2016**, *84*, 89-98.

(135) Liu, Y.; Meng, H.; Messersmith, P. B.; Lee, B. P.; Dalsin, J. L. In *Book*; Springer, 2016; pp 345-378.

(136) Qiu, W.-Z.; Zhong, Q.-Z.; Du, Y.; Lv, Y.; Xu, Z.-K. *Green Chem.* **2016**, *18*, 6205-6208.

(137) Zhang, N.; Jiang, B.; Zhang, L.; Huang, Z.; Sun, Y.; Zong, Y.; Zhang, H. *Chem. Eng. J.* **2019**, *359*, 1442-1452.

(138) Sileika, T. S.; Barrett, D. G.; Zhang, R.; Lau, K. H. A.; Messersmith, P. B. *Angew. Chem., Int. Ed.* **2013**, *52*, 10766-10770.

(139) Wang, H.; Wu, J.; Cai, C.; Guo, J.; Fan, H.; Zhu, C.; Dong, H.; Zhao, N.; Xu, J. *ACS Appl. Mater. Interfaces* **2014**, *6*, 5602-5608.

(140) Zhang, X.; Ren, P.-F.; Yang, H.-C.; Wan, L.-S.; Xu, Z.-K. *Appl. Surf. Sci.* **2016**, *360*, 291-297.

(141) Barclay, T. G.; Hegab, H. M.; Clarke, S. R.; Ginic-Markovic, M. *Adv. Mater.*

Interfaces. **2017**, *4*, 1601192.

(142) LaVoie, M. J.; Ostaszewski, B. L.; Weihofen, A.; Schlossmacher, M. G.; Selkoe, D. J. *Nat. Med.* **2005**, *11*, 1214.

(143) Tian, Y.; Cao, Y.; Wang, Y.; Yang, W.; Feng, J. *Adv. Mater.* **2013**, *25*, 2980-2983.

(144) Anderson, T. H.; Yu, J.; Estrada, A.; Hammer, M. U.; Waite, J. H.; Israelachvili, J. N. *Adv. Funct. Mater.* **2010**, *20*, 4196-4205.

(145) Guo, J.; Richardson, J. J.; Besford, Q. A.; Christofferson, A. J.; Dai, Y.; Ong, C. W.; Tardy, B. L.; Liang, K.; Choi, G. H.; Cui, J. *Langmuir* **2017**, *33*, 10616-10622.

(146) Park, T.; Kim, W. I.; Kim, B. J.; Lee, H.; Choi, I. S.; Park, J. H.; Cho, W. K. *Langmuir* **2018**, *34*, 12318-12323.

(147) Zhang, C.; Xiang, L.; Zhang, J.; Gong, L.; Han, L.; Xu, Z.-K.; Zeng, H. *Langmuir* **2019**.

(148) Yu, J.; Kan, Y.; Rapp, M.; Danner, E.; Wei, W.; Das, S.; Miller, D. R.; Chen, Y.; Waite, J. H.; Israelachvili, J. N. *Proc. Natl. Acad. Sci. U.S.A.* **2013**, *110*, 15680-15685.

(149) Saiz-Poseu, J.; Mancebo-Aracil, J.; Nador, F.; Busqué, F.; Ruiz-Molina, D. *Angew. Chem., Int. Ed.* **2019**, *58*, 696-714.

(150) Zhang, C.; Gong, L.; Xiang, L.; Du, Y.; Hu, W.; Zeng, H.; Xu, Z.-K. *ACS Appl. Mater. Interfaces* **2017**, *9*, 30943-30950.

(151) Eiamchai, P.; Chindaudom, P.; Pokaipisit, A.; Limsuwan, P. *Curr. Appl. Phys.* **2009**, *9*, 707-712.

(152) Xiang, L.; Zhu, S.; Li, M.; Zhang, J.; El-Din, M. G.; Zeng, H. *J. Membr. Sci.* **2019**, *576*, 161-170.

(153) Faghihnejad, A.; Zeng, H. *Langmuir* **2013**, *29*, 12443-12451.

(154) Zeng, H.; Huang, J.; Tian, Y.; Li, L.; Tirrell, M. V.; Israelachvili, J. N. *Macromolecules* **2016**, *49*, 5223-5231.

(155) Helm, C. A.; Knoll, W.; Israelachvili, J. N. *Proc. Natl. Acad. Sci. U.S.A.* **1991**, *88*, 8169-8173.

(156) Oćwieja, M.; Adamczyk, Z.; Morga, M. *J. Colloid Interface Sci.* **2015**, *438*, 249-258.

(157) Espinosa-Jiménez, M.; Giménez-Martın, E.; Ontiveros-Ortega, A. *J. Colloid Interface Sci.* **1998**, *207*, 170-179.

(158) Riddick, J.; Bunger, W.; Sakano, T.; New York, NY: John Wiley and Sons, 1985.

(159) Sahiner, N.; Sagbas, S.; Sahiner, M.; Demirci, S. *Polym. Degrad. Stab.* **2016**, *133*, 152-161.

(160) Hattori, Y.; Shimada, T.; Yasui, T.; Kaji, N.; Baba, Y. *Anal. Chem.* **2019**.

(161) Huang, J.; Liu, X.; Qiu, X.; Xie, L.; Yan, B.; Wang, X.; Huang, Q.; Zeng, H. *J. Phys. Chem. B* **2017**, *121*, 3151-3161.

(162) Loosli, F.; Stoll, S. *Environ Sci Nano.* **2017**, *4*, 203-211.

(163) Lee, D. W.; Lim, C.; Israelachvili, J. N.; Hwang, D. S. *Langmuir* **2013**, *29*, 14222-14229.

(164) Dalsin, J. L.; Lin, L.; Tosatti, S.; Vörös, J.; Textor, M.; Messersmith, P. B. *Langmuir* **2005**, *21*, 640-646.

(165) Khademi, S.; O'Connell, J.; Remis, J.; Robles-Colmenares, Y.; Miercke, L. J.; Stroud, R. M. *Science* **2004**, *305*, 1587-1594.

(166) Mahadevi, A. S.; Sastry, G. N. *Chem. Rev.* **2012**, *113*, 2100-2138.

(167) Pletneva, E. V.; Laederach, A. T.; Fulton, D. B.; Kostić, N. M. *J. Am. Chem. Soc.* **2001**, *123*, 6232-6245.

(168) Lu, Q.; Oh, D. X.; Lee, Y.; Jho, Y.; Hwang, D. S.; Zeng, H. *Angew. Chem., Int. Ed.* **2013**, *52*, 3944-3948.

(169) Rashkin, M. J.; Hughes, R. M.; Calloway, N. T.; Waters, M. L. *J. Am. Chem. Soc.* **2004**, *126*, 13320-13325.

(170) Dougherty, D. A. *Science* **1996**, *271*, 163-168.

(171) Kumpf, R. A.; Dougherty, D. A. *Science* **1993**, *261*, 1708-1710.

(172) Sever, M. J.; Weisser, J. T.; Monahan, J.; Srinivasan, S.; Wilker, J. J. *Angew. Chem., Int. Ed.* **2004**, *43*, 448-450.

(173) Stewart, R. J.; Ransom, T. C.; Hlady, V. *J. Polym. Sci., Part B: Polym. Phys.* **2011**, *49*, 757-771.

(174) Gebbie, M. A.; Wei, W.; Schrader, A. M.; Cristiani, T. R.; Dobbs, H. A.; Idso, M.; Chmelka, B. F.; Waite, J. H.; Israelachvili, J. N. *Nat. Chem.* **2017**, *9*, 473.

(175) Hong, S.; Wang, Y.; Park, S. Y.; Lee, H. *Sci. Adv.* **2018**, *4*, eaat7457.

(176) Zeng, H.; Kristiansen, K.; Wang, P.; Bergli, J.; Israelachvili, J. *Langmuir* **2011**, *27*, 7163-7167.

(177) Gallivan, J. P.; Dougherty, D. A. *J. Am. Chem. Soc.* **2000**, *122*, 870-874.

(178) Rao, J. S.; Zipse, H.; Sastry, G. N. *J. Phys. Chem. B* **2009**, *113*, 7225-7236.

(179) Ahern, C. A.; Eastwood, A. L.; Lester, H. A.; Dougherty, D. A.; Horn, R. *The J. Gen. Physiol.* **2006**, *128*, 649-657.

(180) Lucas, X.; Bauzá, A.; Frontera, A.; Quinonero, D. *Chem. Sci.* **2016**, *7*, 1038-1050.

(181) Yu, Y.-C.; Berndt, P.; Tirrell, M.; Fields, G. B. *J. Am. Chem. Soc.* **1996**, *118*, 12515-12520.

(182) Liu, H.; Liu, X.; Meng, J.; Zhang, P.; Yang, G.; Su, B.; Sun, K.; Chen, L.; Han, D.; Wang, S. *Adv. Mater.* **2013**, *25*, 922-927.

(183) Mitragotri, S.; Burke, P. A.; Langer, R. *Nat. Rev. Drug Discov.* **2014**, *13*, 655.

(184) Knowles, T. P.; Buehler, M. J. *Nat. Nanotechnol.* **2011**, *6*, 469.

(185) Qamar, S.; Wang, G.; Randle, S. J.; Ruggeri, F. S.; Varela, J. A.; Lin, J. Q.; Phillips, E. C.; Miyashita, A.; Williams, D.; Ströhl, F. *Cell* **2018**, *173*, 720-734. e715.

(186) Neela, Y. I.; Sastry, G. N. *Mol. Phys.* **2015**, *113*, 137-148.

(187) Estarellas, C.; Frontera, A.; Quiñonero, D.; Deyà, P. M. *Angew. Chem. Int. Ed.* **2011**, *50*, 415-418.

(188) Zhang, K.; Zhang, F.; Song, Y.; Fan, J. B.; Wang, S. *Chin. J. Chem* . **2017**, *35*, 811-820.

(189) Zhao, Y.; Wu, Y.; Wang, L.; Zhang, M.; Chen, X.; Liu, M.; Fan, J.; Liu, J.; Zhou, F.; Wang, Z. *Nat. Commun.* **2017**, *8*, 2218.

(190) Hofman, A. H.; van Hees, I. A.; Yang, J.; Kamperman, M. *Adv. Mater.* **2018**, *30*, 1704640.

(191) Stewart, R. J.; Wang, C. S.; Song, I. T.; Jones, J. P. *Adv. Colloid Interface Sci.* **2017**, *239*, 88-96.

(192) Maeda, N.; Chen, N.; Tirrell, M.; Israelachvili, J. N. *Science* **2002**, *297*, 379-382.

(193) Kim, S.; Peterson, A. M.; Holten-Andersen, N. *Chem. Mater.* **2018**, *30*, 3648-3655.

(194) Tse, B.; Kishi, Y. *J. Org. Chem.* **1994**, *59*, 7807-7814.

(195) Bergeron, R. J.; Singh, S.; Bharti, N. *Tetrahedron* **2011**, *67*, 3163-3169.

(196) Felix, A. M.; Heimer, E. P.; Lambros, T. J.; Tzougraki, C.; Meienhofer, J. *J. Org. Chem.* **1978**, *43*, 4194-4196.

(197) Frisch, M.; Trucks, G.; Schlegel, H.; Scuseria, G.; Robb, M.; Cheeseman, J.; Scalmani, G.; Barone, V.; Petersson, G.; Nakatsuji, H.; Li, X.; Caricato, M.; Marenich,

A.; Bloino, J.; Janesko, B.; Gomperts, R.; Mennucci, B.; Hratchian, H.; Ortiz, J.; Izmaylov, A.; Sonnenberg, J.; Williams-Young, D.; Ding, F.; Lipparini, F.; Egidi, F.; Goings, J.; Peng, B.; Petrone, A.; Henderson, T.; Ranasinghe, D.; Zakrzewski, V.; Gao, J.; Rega, N.; Zheng, G.; Liang, W.; Hada, M.; Ehara, M.; Toyota, K.; Fukuda, R.; Hasegawa, J.; Ishida, M.; Nakajima, T.; Honda, Y.; Kitao, O.; Nakai, H.; Vreven, T.; Throssell, K.; Montgomery, J.; Peralta, J., JE; Ogliaro, F.; Bearpark, M.; Heyd, J.; Brothers, E.; Kudin, K.; Staroverov, V.; Keith, T.; Kobayashi, R.; Normand, J.; Raghavachari, K.; Rendell, A.; Burant, J.; Iyengar, S.; Tomasi, J.; Cossi, M.; Millam, J.; Klene, M.; Adamo, C.; Cammi, R.; Ochterski, J.; Martin, R.; Morokuma, K.; Farkas, O.; Foresman, J.; Fox, D. *Gaussian 09, Revision E. 01, Gaussian, Inc., Wallingford CT* **2016**.

(198) Grimme, S.; Ehrlich, S.; Goerigk, L. *J. Comput. Chem.* **2011**, *32*, 1456-1465.

(199) Yang, J.; Stuart, M. A. C.; Kamperman, M. *Chem. Soc. Rev.* **2014**, *43*, 8271-8298.

(200) Kalyanaraman, B.; Felix, C.; Sealy, R. *Environ. Health Perspect.* **1985**, *64*, 185-198.

(201) Wu, T.-l.; Qin, W.-x.; Alves, M. E.; Fang, G.-d.; Sun, Q.; Cui, P.-x.; Liu, C.; Zhou, D.-m.; Wang, Y.-j. *Chem. Eng. J.* **2019**, *356*, 190-198.

(202) Saab, S. C.; Martin-Neto, L. *J. Braz. Chem. Soc.* **2008**, *19*, 413-417.

(203) Moulay, S. *Polym. Rev.* **2014**, *54*, 436-513.

(204) Hong, S.; Lee, H.; Lee, H. *Beilstein J. Nanotechnol.* **2014**, *5*, 887-894.

(205) Sanchez-Cortes, S.; Francioso, O.; Garcıa-Ramos, J.; Ciavatta, C.; Gessa, C. *Colloids Surf. Physicochem. Eng. Aspects* **2001**, *176*, 177-184.

(206) Zhang, M.; Peltier, R.; Zhang, M.; Lu, H.; Bian, H.; Li, Y.; Xu, Z.; Shen, Y.; Sun, H.; Wang, Z. *J. Mater. Chem. B* **2017**, *5*, 5311-5317.

(207) Sieste, S.; Mack, T.; Synatschke, C. V.; Schilling, C.; Meyer zu Reckendorf, C.; Pendi, L.; Harvey, S.; Ruggeri, F. S.; Knowles, T. P.; Meier, C. *Adv. Healthcare Mater.* **2018**, *7*, 1701485.

(208) Kim, D.; Lee, E. C.; Kim, K. S.; Tarakeshwar, P. *J. Phys. Chem. A* **2007**, *111*, 7980-7986.

(209) Garau, C.; Quiñonero, D.; Frontera, A.; Ballester, P.; Costa, A.; Deyà, P. M. *New J. Chem.* **2003**, *27*, 211-214.

(210) Carrazana-García, J. A.; Rodríguez-Otero, J. s.; Cabaleiro-Lago, E. M. *J. Phys. Chem. B* **2012**, *116*, 5860-5871.

(211) Purushotham, U.; Vijay, D.; Narahari Sastry, G. *J. Comput. Chem.* **2012**, *33*, 44-59.

(212) Lo Nostro, P.; Ninham, B. W. *Chem. Rev.* **2012**, *112*, 2286-2322.

(213) Marcus, Y. *Chem. Rev.* **1988**, *88*, 1475-1498.

(214) Mason, P.; Neilson, G.; Dempsey, C.; Barnes, A.; Cruickshank, J. *Proc. Natl. Acad. Sci. U. S. A.* **2003**, *100*, 4557-4561.